Spring 5-2024

Numerical Simulations of Supersonic/ Hypersonic Flows in Compression Corners and a Hypersonic Flow Study of Atmospheric Entry of Mars Science Laboratory Capsule

Dexter Allen
Washington University – McKelvey School of Engineering

WASHINGTON UNIVERSITY IN ST. LOUIS

McKelvey School of Engineering

Department of Mechanical Engineering and Materials Science

Thesis Examination Committee:

Ramesh K. Agarwal, Chair

Swami Karunamoorthy

David A. Peters

Numerical Simulations of Supersonic/ Hypersonic Flows in Compression Corners and a Hypersonic Flow Study of Atmospheric Entry of Mars Science Laboratory Capsule

by

Dexter J. P. Allen

A thesis presented to
the McKelvey School of Engineering
of Washington University in
partial fulfillment of the
requirements for the degree
of Master of Science

May 2024

St. Louis, Missouri

Table of Contents

List of Figures

List of Tables

Acknowledgments

I would like to thank Prof. Ramesh K. Agarwal for his outstanding technical advice and guidance throughout the course of this research. He has provided very valuable help and has taken a good deal of time away from his schedule to provide this help to me as well as all his other graduate students. I would also like to thank other graduate students in Dr. Agarwal's group in Computational Fluid Dynamics (CFD) laboratory who helped me frequently throughout this project including Bryce Thomas, Mike Kiely, Aidan Murphy, and Dean Ryan-Simmons.

I would like to thank Dr. Seokkwan Yoon of NASA Ames Research Center for the opportunity to do research in his department as well as Patricia Ventura Diaz for providing a great deal of help in how to use the various NASA software and facilities. I would also like to thank Dr. Denis-Gabriel Caprace and David García Pérez for their help and advice, and Dr. Aga Goodsell for help in navigating the field of aerospace engineering.

Finally, I would like to thank my parents, Dr. Karen Poremski and Patrick Allen for their great love and support throughout this work as well as all of my friends.

Dexter J. P. Allen

Washington University in St. Louis

May 2024

ABSTRACT OF THE THESIS

Numerical Simulations of Supersonic/ Hypersonic Flows in Compression Corners and a Hypersonic Flow Study of Atmospheric Entry of Mars Science Laboratory Capsule

by

Dexter Allen

Master of Science in Aerospace Engineering

Washington University in St. Louis, 2024

Professor Ramesh K. Agarwal, Chair

This thesis consists of two related parts. The first part is the study of supersonic/hypersonic flow in compression corners. The compression corners are simple geometries but rich in flow-features that can be challenging for accurate prediction of their flow fields in high-speed compressible flow using the Reynold-Averaged Navier-Stokes (RANS) equations in conjunction with a turbulence model. At higher degrees of corner angles, there exists a shock-boundary layer interaction region which includes a significant recirculation zone in the corner. In this thesis, experimentally available test cases for compression corner at Mach 3, 8, and 11 at various corner angles are modeled as 2D planar geometries and are simulated using the ANSYS Fluent. Results are compared to the experimental studies for the same flow conditions from Settles et al. and Smits and Muck at Mach 2.85 and from Holden et al. at Mach 8 and Mach 11 for various corner angles. The Spalart-Allmaras (SA), SST k-ω, and Wray-Agarwal (WA) turbulence models are employed in the study. The surface static pressure, heat transfer rate, and separation bubble in the corner are compared between the simulations and the experiments. Generally, it was found that the SA model's accuracy begins to falter at the higher corner angles (> 20+ degrees). It was found that SST k-ω and WA models are suitable for these flow conditions, as they can reproduce the trends seen in the experimental static pressure measurements. Additionally, it was found that the WA model shows good behavior in generating the major recirculation region that is present in the corner for the higher corner angles (>20+ degrees).

The second part of the thesis consists of a hypersonic flow study of atmospheric entry of Mars Science Laboratory (MSL) Capsule. The MSL spacecraft architecture constituted the design of the Curiosity and Perseverance rover missions. The heat shield of the MSL capsule used a tiled PICA (Phenolic Impregnated Carbon Ablator) TPS (Thermal Protection System), with gap-filler material applied in the space between the tiles. During atmospheric entry at high Mach numbers, the instrumentation of the MSL heatshield reported a sharp rise in the net heating rate of the heatshield, which indicated an earlier-than-expected onset of turbulent flow over the heatshield. A CFD investigation was conducted to determine if the protrusion of the gap-filler after a period of ablation could be a significant factor in the onset of turbulent flow over the heat shield. The case was run using the resources of NASA Ames Research Center's Advanced Supercomputing Division and employed NASA's DPLR hypersonic CFD code. The results obtained suggest that the gap-filler protrusion is a significant fact

Chapter 1: Mars Science Laboratory (MSL) Hypersonic Flow Study

1.1 Background

Reentry is one of the less well-understood aspects in space exploration engineering. Low level of confidence in predicted heating rates and turbulent transitions for a spacecraft during atmospheric entry means that a very significant amount of weight of the spacecraft must be used in applying a heavier-than-predicted thermal protection system to account for this low level of confidence. Because of the high Mach numbers (often more than 20), it is not yet possible to test a heat shield on the ground that simulates all flight conditions satisfactorily. Current ground tests include testing the geometry and flow separation using a shock cannon, and testing materials using an arc jet. Aerodynamic theories regarding reentry, and CFD simulations of reentry cannot therefore be compared to real physical data in most cases, and therefore must settle for verification at lower Mach numbers. Real physical data can be captured with instrumentation on real heat shields, and with the analysis of the heat shield after its use.

For a long time, instrumentation was not used on uncrewed exploration missions because of the difficulty in the implementation of the instruments on the spacecraft. Due to the harsh nature of the atmospheric entry, not even a very small portion of the heat shield face could be left empty to fit the instrumentation, since making such a modification would require confidence that the heat shield can survive entry in its new configuration. Additionally, any instrument which is exposed directly to the oncoming flow will instantly be destroyed. Therefore, flight data is often inferred from the instrumentation placed well inside of the heat shield. For smaller uncrewed missions, this can be a difficult task and can add significantly to the budget of the entry system.

The NASA Genesis mission is one such mission which did not utilize significant heat shield instrumentation. The Genesis mission was an uncrewed exploration probe that operated from 2001 to 2004, collecting solar wind at Earth-Sun L1 location for 28 months, and returned to Earth September 2004 with collectors (very pure materials with highly polished surfaces) into which solar wind atoms were implanted, typically 40 to 100 nm below the surface. Immediately following the atmospheric entry, the drogue parachute on the capsule failed, causing it to crash into the ground and be damaged to such an extent that a significant number of the samples were unusable. It was eventually determined that this failure was not directly caused by the atmospheric entry environment, but the failure did reveal a weakness in the ability of the investigation team to recreate the reentry given the lack of heat shield data. Therefore, for the Mars Science Laboratory mission architecture (Curiosity and Perseverance Rovers), it was decided that a suite of instrumentation plugs would be added into the heat shield to provide full reentry data.

Mars Science Laboratory (MSL) is a mission architecture that refers to the Curiosity and Perseverance Rovers. Curiosity was launched in 2011 and Perseverance was launched in 2020. Due to a test failure in the previous standard heat shield material, SLA-561V (Super Light Ablator), a newer material, PICA (Phenolic-Impregnated Carbon Ablator) was chosen as the ablative material for the MSL heat shield. PICA is made up of a matrix of carbon fibers immersed in phenolic resin. The resin provides the desired ablation effects while the carbon matrix provides the structure. PICA was originally developed for the Stardust mission, which was a comet trail sample return mission. The MSL heat shield needed to be 4.5 meters in diameter, which is significantly larger than the 32-inch heat shield of Stardust. Because of PICA’s brittle nature, a 4.5-meter single piece heat shield would likely crack and fracture under thermal stresses alone.

Therefore, the MSL heat shield was designed using multiple ablative PICA tiles which fit together to create the full shield as shown in Fig. 1.1.

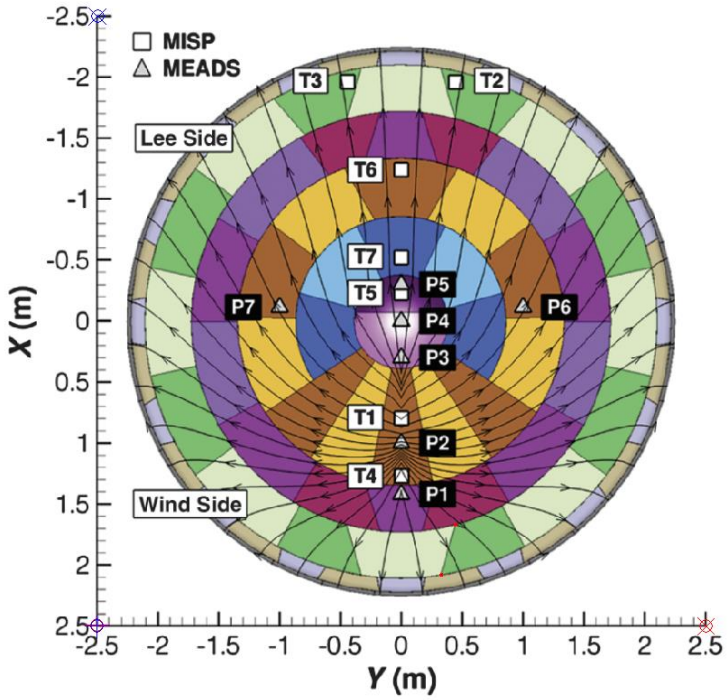

Figure 1.1. Diagram showing the placement of TPS tiles and sensors. [1]

There must be some room left for the tiles to thermally expand, so gaps on the millimeter-scale are left open during PICA placement, and then filled using a silicone-based gap-filler. Unlike the ablative PICA, the gap-filler material tends to simply burn when exposed to entry conditions and does not reduce in size the way the ablative materials do. This means that the surface of the PICA, which makes up the tiles, will be reduced during the entry, leaving "fences" of gap-filler protruding up to a few centimeters from the heat shield. A concern regarding this gap-filler fencing is that it will encourage turbulence in the flow passing over the face of the heat shield. Convective heat transfer rates in a turbulent boundary layer are higher than in a laminar boundary layer; thus, this turbulence would increase the net heating rate to the heat shield. Figure 1.2 shows the increased heating in turbulent flow for the MSL spacecraft.

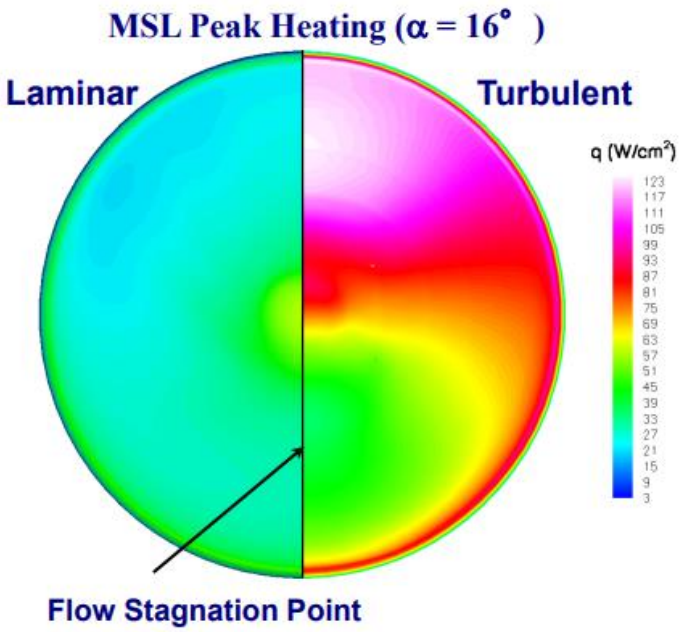

Figure 1.2 Diagram showing the increased heating in turbulent flow for the MSL spacecraft. [2]

The MSL heat shields used an instrumentation suite which consisted of a series of PICA plugs containing thermocouples placed at several points within the heat shield. During reentry of Curiosity, these sensors detected a sharp increase in heating rate that occurred during the most thermally intense part of entry. This heating rate spike was seen first at the sensors near the leeward shoulder, and then it was seen to spread down the length of the heat shield. It was assumed that this sharp increase in the heating rate is due to the flow over the heat shield becoming turbulent [3]. However, CFD models predicted that this transition would occur at a later point in the atmospheric entry. A CFD simulation of the gap-filler fencing on the MSL heat shield, using flow conditions like the real entry is therefore considered here to obtain results which may support the hypothesis that the presence of gap-filler fencing can contribute to the flow to become turbulent.

This section of research was performed at NASA Ames Research Center in Mountain View, California; the work done as a part of the NASA OSTEM internship. Although all of this work is my own, advice and guidance were provided by Patricia Ventura Diaz (NASA).

1.2 Computational Tools

The geometry generation was done using my own python script. The script takes the parameters of the number of gap-fillers, total radius of the heat shield, heat shield angle, flow domain width, and the nose and shoulder diameters, and generates an array of coordinate points with half-geometry of the front face of the heat shield with gap fillers protruding. The array of points is then saved by the code in the .xyz format, and is ready to be imported into the meshing software to create a 2D axisymmetric mesh of the flow domain. The meshing of the flow domain geometry was completed using Fidelity Pointwise. Fidelity Pointwise is a software made for the generation of 2D and 3D meshes and grids, created by the Cadence Design Systems.

The CFD simulation software used for was the NASA's Data-Parallel Line Relaxation (DPLR) code. DPLR is a CFD code written in Fortran 90 by Dr. Michael Wright. It was developed specifically for use in spacecraft atmospheric entry applications for Earth and other planetary atmospheres. Due to this specialized purpose, it contains many built-in features in the code that are pertinent to atmospheric entry cases. Examples include chemical reactions simulation with dissociation and ablation products represented by the blowing surface boundary conditions [2]. The Johnston 2014 Martian chemistry model was used to simulate molecular dissociation and reaction due to the hypersonic nature of the flow.

There are four tools built into DPLR: DPLR2D and DPLR3D, which are the CFD solvers; FCONVERT, which is a mesh pre-processing code used to prepare a mesh for use by the parallel solver DPLR; and POSTFLOW, which is a solution post-processor that exports results files from DPLR that can be read by other post processing software [4]. In this research, all the tools of DPLR were used with the exception of DPLR3D, since only the 2D axisymmetric case was studied. DPLR utilizes a massively parallel algorithm for optimal use of the NASA Ames' supercomputers.

For this research, CFD cases were run on the Aitken, Pleiades, and Electra supercomputers which are managed and maintained by NASA Ames' Advanced Supercomputing Division.

Completed cases were post-processed using DPLR POSTFLOW. While at NASA Ames, results were viewed using Tecplot 360, a CFD postprocessing software. Tecplot 360 was accessed using a license owned by Ames Research Center. After returning to Washington University in St. Louis, results of the research were viewed using ParaView. ParaView is a free CFD postprocessing software that is able to open the .dat file format employed by the DPLR POSTFLOW for its files.

1.3 Geometry

The MSL entry case was modeled as a 2D axisymmetric geometry. This simplification meant that the angle of attack for the capsule was limited to zero, which differs from the real case where the angle of attack is significant to achieve a lifting entry profile. However, due to the time limitation and the main focus and interest of research was on studying the effect of gap-filler fencing on the nature of the flow field and not on recreating a highly accurate entry profile, this simplification was made. To model the non-zero angle of attack, a fully 3D geometry of MSL and mesh around it would be required.

A python script was written that generated an array of coordinates in the flow domain. The initial flow domain consisted of a 2D axisymmetric nose, shield face and shoulder, and extended 2 meters from the solid geometry. The size of the flow domain was refined to cut out many of the unneeded cells after initial simulations revealed the shock location. Figure 1.3 shows the model of the MSL spacecraft showing the modeled geometry in green (on left side of the figure) [5].

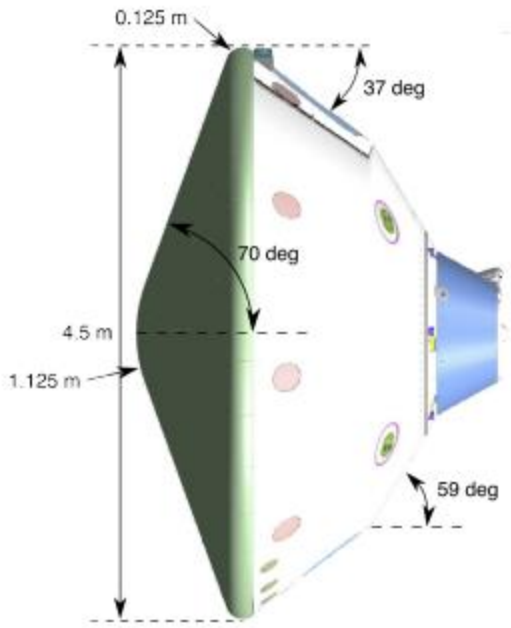

Figure 1.3. Model of the MSL spacecraft showing the modeled geometry in green (on left side of the figure) [5].

1.4 Mesh

The challenge in simulation lay mostly in the meshing. One of the mesh qualities to avoid in creating a mesh is non-orthogonality, which is a measure of how "tilted" a mesh cell is. For example, a mesh cell that is a perfect square or rectangle (it has all four interior angles at 90 degrees) would have a non-orthogonality of zero. Because of the presence of sharp interior and exterior angles on the gap-filler geometry, minimizing the non-orthogonality becomes a challenge. The curves were created which originated at the corners of the gap-filler geometry and adapted the shape of the mesh close to the surface to match with the more uniform mesh far from the surface. Figure 1. shows the view of the fully meshed flow domain and the flow domain near the gap filler showing the refined mesh at the shock. Figure 1.5 shows the zoomed-in view of the mesh near the gap filler showing how the mesh adapts to the uniform mesh farther from the surfaces. Figure 1.6 shows the highly zoomed-in view of the mesh near the surface showing the mesh growth rate.

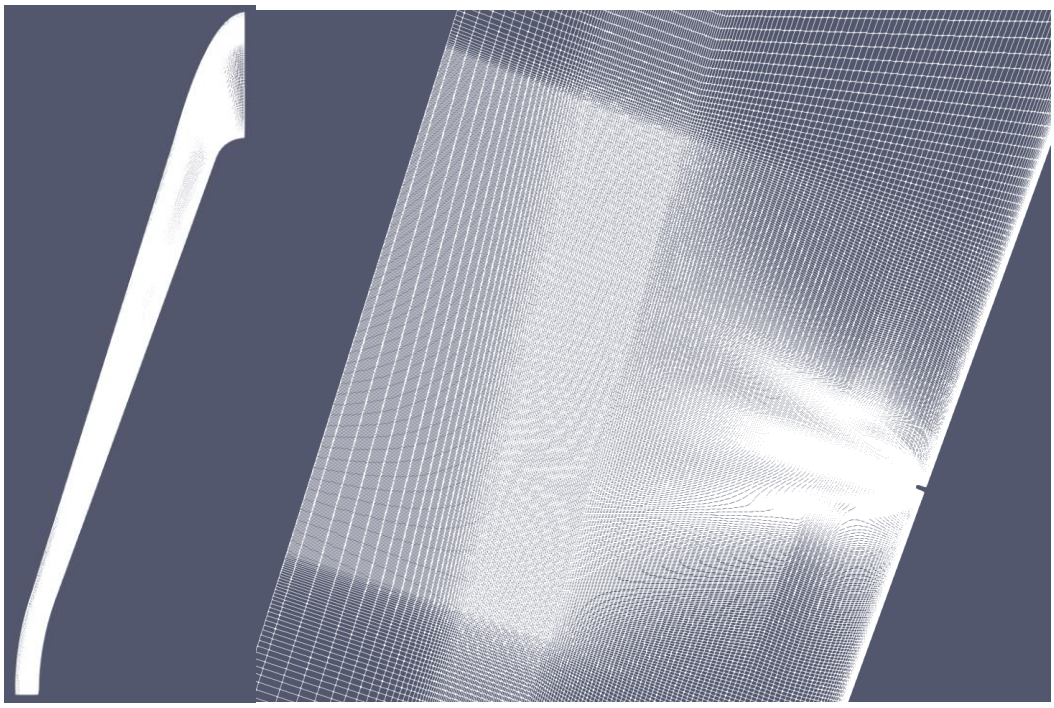

Figure 1.4. View of the full meshed flow domain (left) and flow domain near the gap filler (right), showing the refined mesh at the shock.

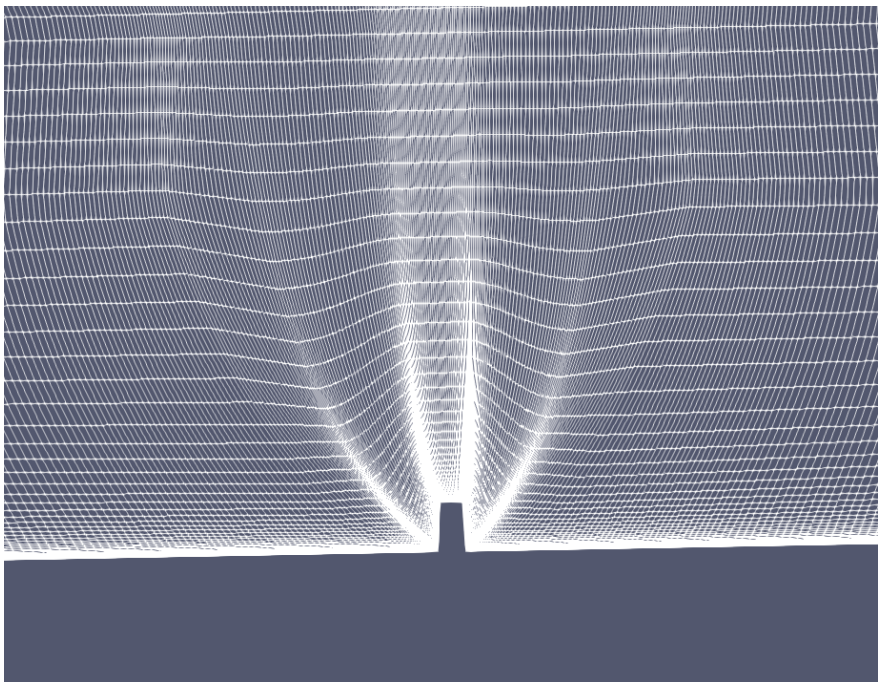

Figure 1.5 Zoomed-in view of the mesh near the gap filler showing how the mesh adapts to the uniform mesh farther from the surfaces.

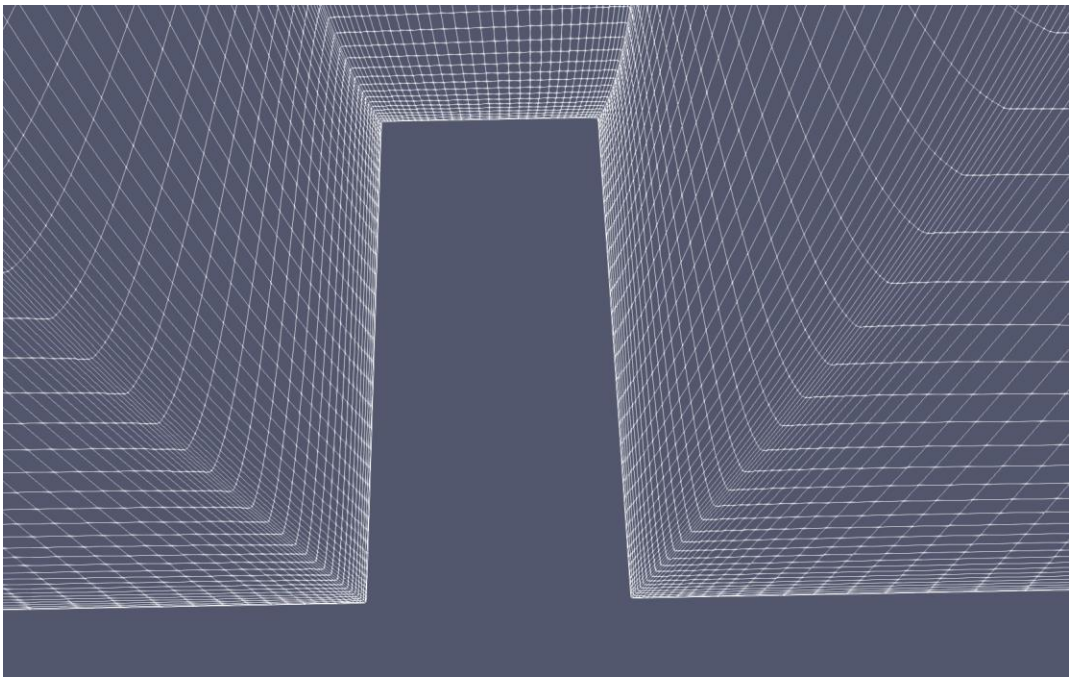

Figure 1.6 Highly zoomed-in view of the mesh near the surface showing the mesh growth rate.

Another challenge in meshing is the major difference in scale between the gap-filler features and the heat shield. The heat shield has a diameter of 4.5 meters, while the gap-fillers are only 1-2 millimeters thick. The gap-fillers needed to be treated with an extremely fine mesh to capture the interactions between the boundary layer and the corners of the fencing. However, if the entire heat shield is meshed to such a fine level, there would be far too many cells, and the computation would be very inefficient. Since the flat sections of the heat shield do not require such a fine mesh, the total number of cells can be significantly reduced, and the computational accuracy can still be maintained. To solve the problem of the differences in the size of the mesh cells in various parts of the flow domain, each gap-filler was surrounded by a box consisting of very fine mesh and a second box which contained the first box that acted as a transition mesh between the relatively coarse heat shield mesh and the very fine gap-filler mesh. The subdivisions of the sides of these boxes were done in a way such that no cell in the mesh exceeded a growth rate of 1.3.

1.5 Flow Field Computations

The computations were first performed on an initial mesh assuming the flow to be laminar as well as turbulent. For turbulent flow simulations, Reynolds-Averaged Navier-Stokes (RANS) equation were employed in conjunction with several turbulence models, including the SST k-omega, the Spalart-Allmaras (SA), and the Baldwin-Lomax model. The SST k-omega model was found to have the most numerical stability in the computations, therefore the results obtained with the SST k-omega model were used to refine the initial mesh. In the mesh refinement, unneeded upstream cells that were well outside the shock region were eliminated. This is because of the nature of supersonic/ hypersonic flows in which the flow field information cannot travel upstream of a shock wave. Therefore, all cells that are upstream of the shock simply reflect the unaltered freestream conditions of the inlet boundary condition, and therefore the number of these cells can be kept small. The shock region should have a more refined mesh than needed in the upstream region. The result using the initial mesh gave a location of the shock wave, which was then used to refine the mesh near this initial shock location. Figure 1.7 shows the Mach number contours with mesh overlay depicting the refined mesh near the shock.

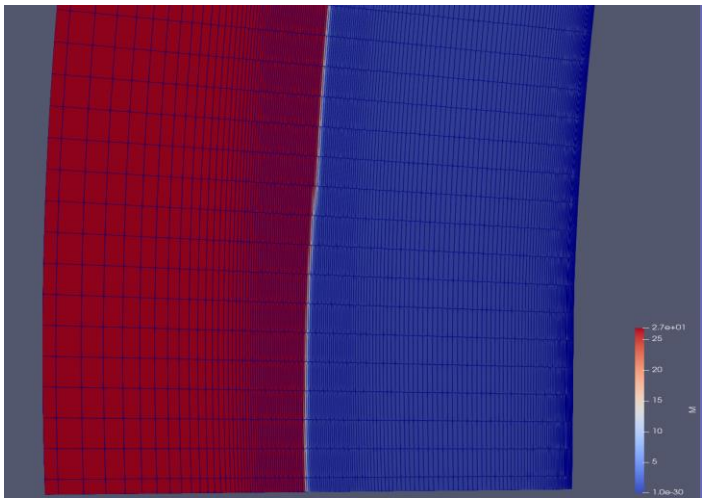

Figure 1.7 Mach number contours with mesh overlay showing the refined mesh near the shock.

Due to the time constraints, it was possible to complete only one mesh refinement. The SST k-omega turbulence model was chosen to complete the simulations on the refined mesh, since it had no computational stability issues on the initial mesh, and it is a well-tested and widely used turbulence model. On the refined mesh, the Mach 26 case was conducted, which matched the real-life flow conditions at the peak heating point. Studies were also completed for Mach 20, 35, 40, 45, and 50 cases. Although these additional cases do not correspond to any point in the real flight trajectory of the two MSL spacecraft, it was surmised that by increasing the Mach number, the qualitative effect of the presence of the gap filler fencing on the flow would be exacerbated, and therefore would be easier to analyze. Furthermore, by testing a range of Mach numbers, it could be inferred if the effects of the fencing on the flow was sensitive to the freestream Mach number.

1.6 Results and Discussion

The results using the refined grid and the SST k-Omega turbulence model are presented in this section. Computations were continued until the residuals of the flow quantities reached below 10^-4. In the actual flight conditions of the MSL spacecraft, peak heating occurred at roughly Mach 26 [6]. One case was computed at Mach 26 to analyze the effect of the gap-filler on the flow. Figure 1.8 shows the velocity contours near and just downstream of the gap-filler at Mach 26. The deep blue region downstream of the gap-filler represents the recirculation region. Here, the nature of the geometry prevents the flow from adhering to the wall as it goes over the gap-filler fencing. The flow layer thus detaches into a separation layer, and the space below the separation layer becomes a recirculation region in which fluid particles become trapped. The fluid-to-fluid interactions in the interface between the recirculation region and the separated flow increases the turbulence of the flow in the separation layer. Therefore, a large recirculation region, as seen in this figure supports the hypothesis that the presence of the gap-filler fencing is a major contributor

to the onset of turbulent flow over the surface. Figure 1.9 shows the pressure contours close to the gap-filler. There is a significant pressure gradient between the leading and trailing side of the gap-filler, and the difference in pressure has a large gradient at the top leading edge of the gap-filler fencing. This suggests that with this geometry, the top leading edge is the point of flow separation as the flow goes over the fencing.

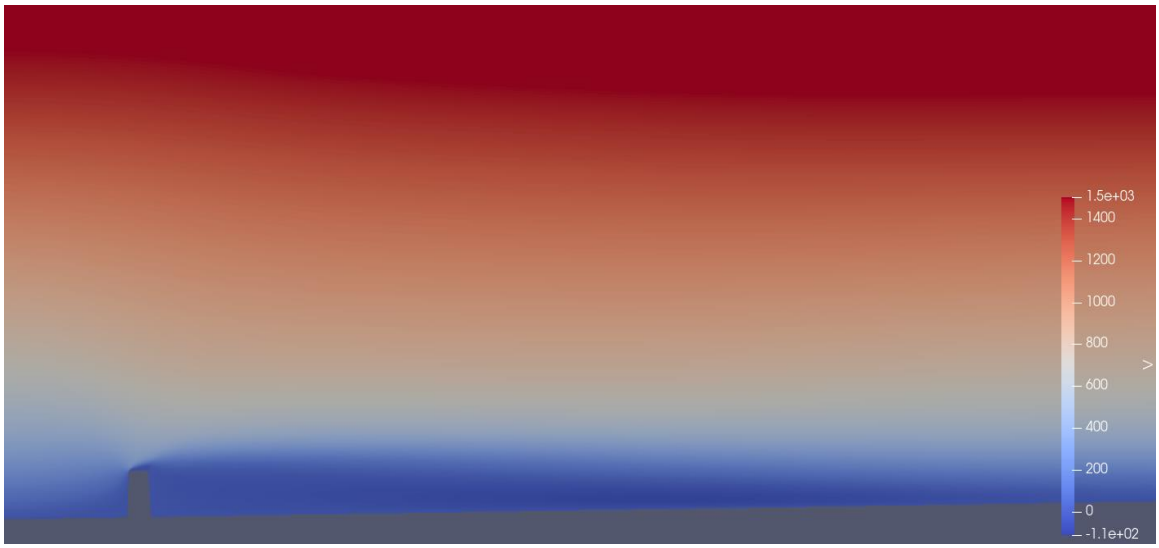

Figure 1.8 Velocity contours near the gap filler at Mach 26.

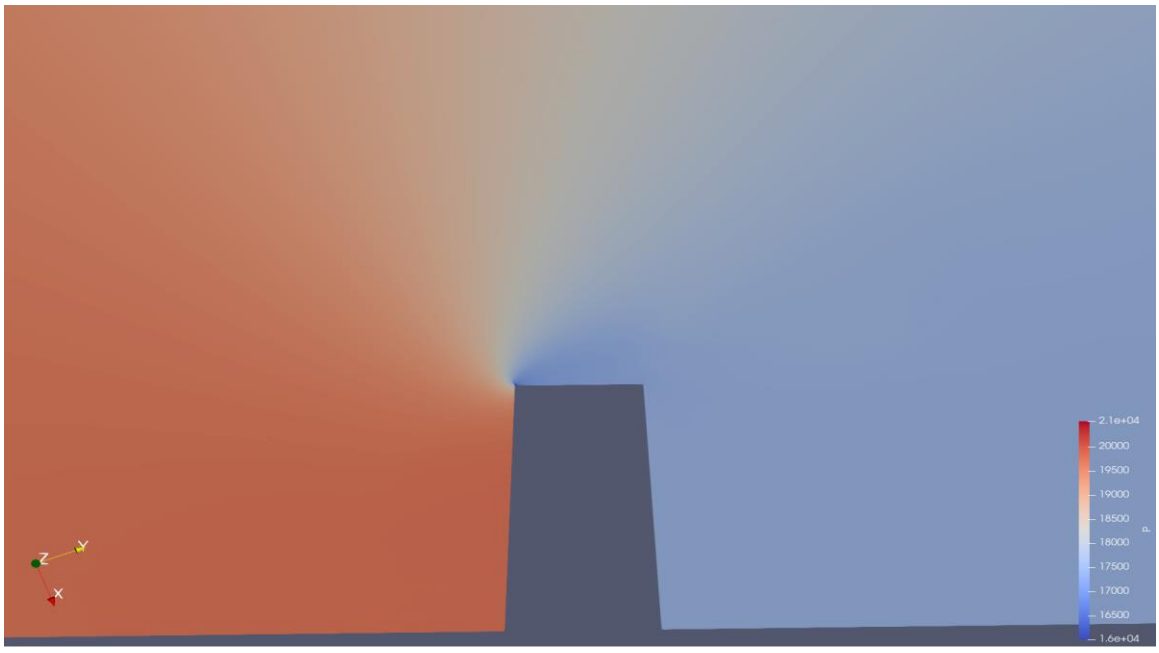

Figure 1.9 Pressure contours near the gap filler at Mach 26.

Figures 1.10 to 1.14 show the unit Reynolds number Re/L in the flow passing over the gap filler fencing at various Mach numbers. The unit Reynolds number Re/L is a localized Reynolds number that acts as a measure of the extent of turbulence in the flow in each location. It is shown in these figures that there is a sharp increase in the localized flow Reynolds number at the top leading edge of the gap filler fencing. This increase in Re/L supports the hypothesis that the gap filler fencing is encouraging the onset of turbulence in the flow over the face of the heatshield, and thus is the reason for the earlier-than-expected onset of turbulence in the MSL atmospheric entry.

The severity of the increase in Re/L is dependent on freestream Mach number of the flow. In the lower Mach number flows (M = 20, 35), the severity in the increase in Re/L is greater than that in the higher Mach number flows (M = 45, 50). This suggests that the presence of the gap-filler fencing encourages the onset of turbulence to a greater degree when the freestream Mach number is lower. Although it cannot be considered as a definitive conclusion, it suggests that the presence of the fencing encourages the onset of turbulent flow to a greater degree as the Mach number of the entry capsule decreases during heating.

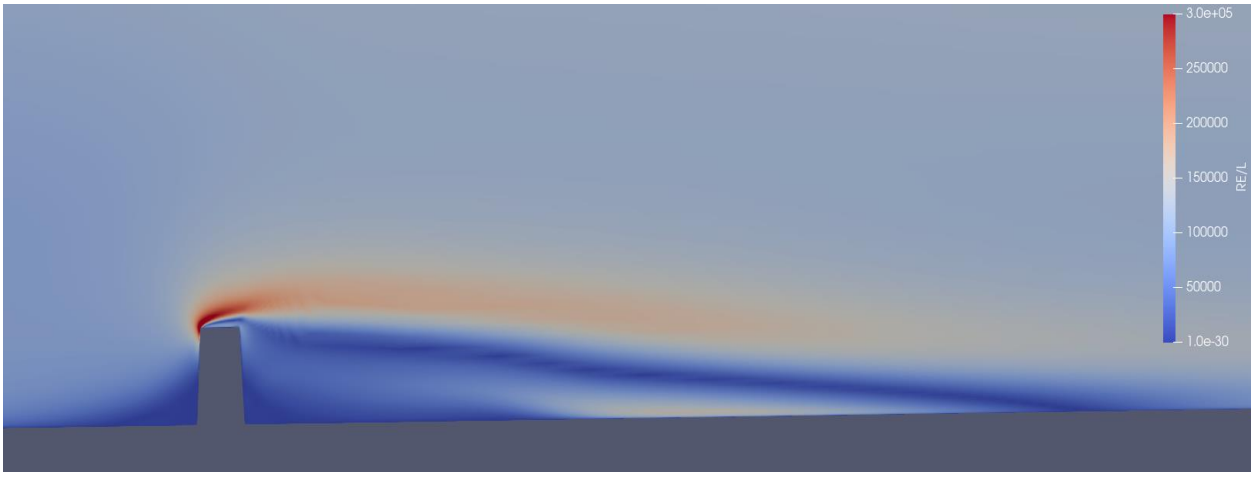

Figure 1.10 Re/L contour plots at Mach 20.

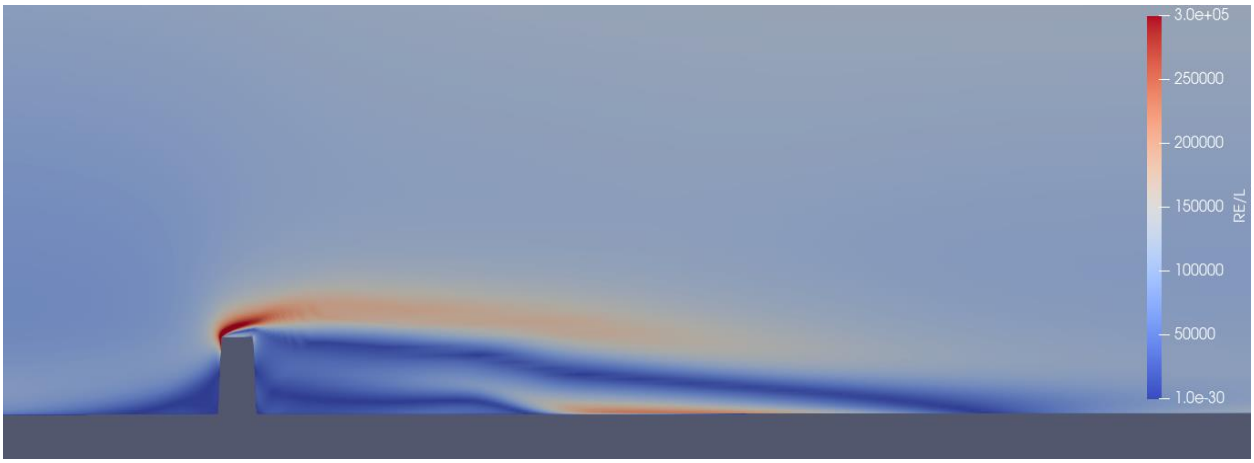

Figure 1.11 Re/L contour plots at Mach 35.

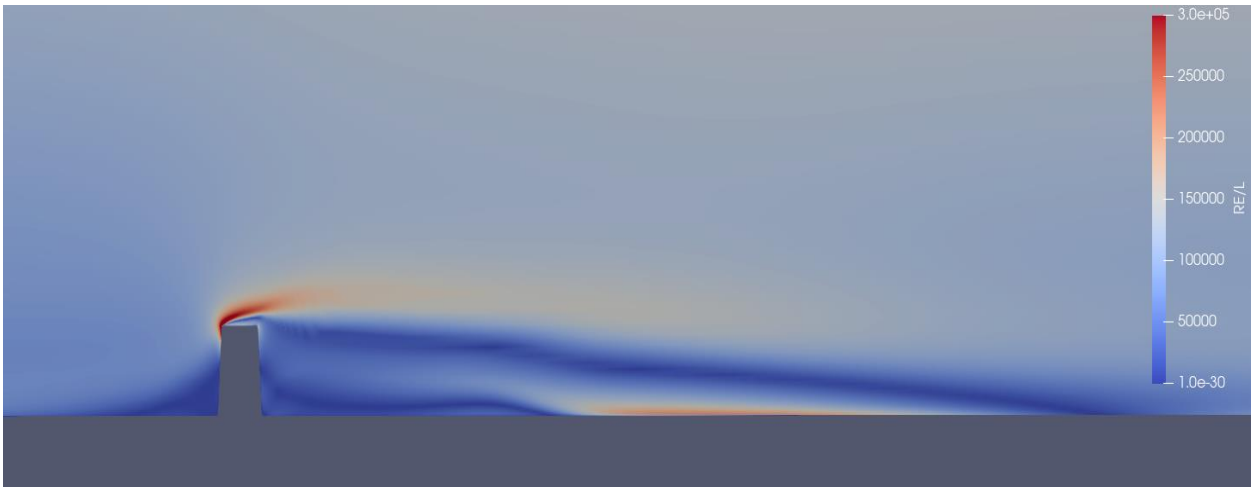

Figure 1.12 Re/L contour plots at Mach 40.

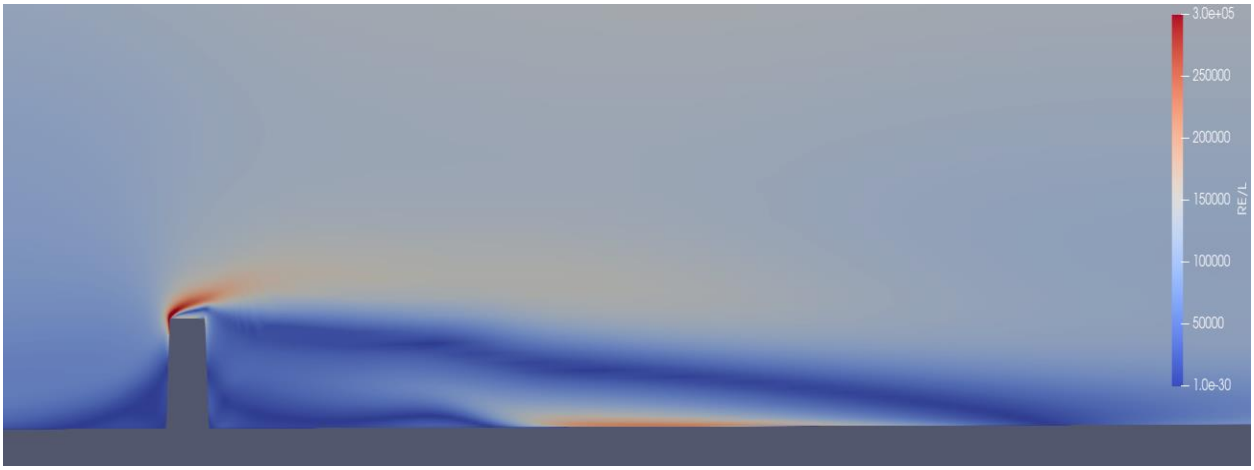

Figure 1.13 Re/L contour plots at Mach 45.

Figure 1.14 Re/L contour plots at Mach 50.

1.7 Future Work

The depth of research described in this chapter was limited by the length of the small duration of ten-week stay at NASA Ames Research Center, where the research for this chapter was performed. If this simulation case is revisited in the future, a more reliable solution could be achieved by refining the mesh further to better capture the shock and the flow features near the wall and the gap filler. With significantly more computational effort, the effect of the angle of attack on the entry of the 3D Mars spacecraft could be simulated by using a 3D geometry and refined mesh. The NASA 3D geometry of the MSL entry capsule is already available, and for this research project a python script has already been written which adds gap-filler fencing to the existing 3D MSL geometry. Nevertheless, even with the 3D geometry already completed, generating the mesh for the 3D model with gap filler fencing would be a significant undertaking.

On the refined mesh, the only turbulence model that was used in the research reported in this chapter was the SST k-Omega model. It would be interesting to determine if other turbulence models such as the SA model give similar results and conclusions regarding the fencing's influence of the onset of turbulent flow. Given that only one turbulence model was tested, no definitive

conclusion can be made about the reliability of the SST k-omega model to accurately simulate the turbulence effects for the MSL entry problem. Additionally, it would also be interesting to implement the Wray-Agarwal model described in chapter 2 into the DPLR CFD code and compare its results to the SST k-Omega and SA results.

In terms of gaining more confidence in the engineering of gap-filler fencing in the heat shields, there is a major constraint in the ability to collect experimental data. No ground testing facilities can create conditions that adequately recreate the conditions of the real atmospheric entry. For example, the wind tunnels and the arc jets cannot achieve the Mach numbers that are found in the atmospheric entry, and the shock tubes cannot simulate the prolonged heating effects that come with a several-minute long trajectory. Unfortunately, due to the efforts to minimize the budget of robotic missions, most unmanned atmospheric entry capsules are not equipped with thermal sensors inside the heat shield for gathering flight performance data that can be used in improving the computational models for atmospheric entry. In terms of validation, the CFD codes are limited to manned capsules, as well as the few robotic missions that do contain sensor suites for the heatshield. Therefore, as more entry data becomes available from spaceflight programs such as Artemis, there will be the opportunity to conduct further experimental and computational comparisons related to the flow field and other heating effects on the surface of the atmospheric entry capsules.

Chapter 2: Supersonic/Hypersonic Flows in Compression Corners

2.1 Introduction

Today, computational fluid dynamics (CFD) technology has achieved the level of maturity that it is considered as the single most powerful tool in the analysis and design of fluid systems. Unlike the most analytical methods and simpler equations sets, it can solve the full Navier-Stokes equations without simplifications accounting for unsteadiness, compressibility and viscosity and can be applied to solve the complex three-dimensional flows in natural and industrial fluid systems. However, although in principle it is true, it is still not feasible to solve the 3D complex turbulent flows from first principles due to the computational requirements of resolving the predominant length and time scales of turbulence for a given problem. Currently, the problem of solving the turbulent flows is addressed by employing the Reynolds-Averaged Navier-Stokes (RANS) equations which have the so called "Closure" problem due to the appearance of unknown "Reynolds Stresses" in the RANS equations. These Reynolds Stresses are expressed in terms of a strain tensor via an eddy viscosity using the Boussinesq approximation. This approximate modeling of turbulent stresses is called the "Turbulence Modeling."

Thus, to simulate the effects of turbulence in a fluid system, RANS equations are solved in conjunction with a turbulence model. There is not a single universal turbulence model. Over a century, many turbulence models have been developed with each having its own merits and drawbacks. The majority of the turbulence models employ one- or two transport equations involving one or two prominent turbulence variables such as turbulent kinetic energy and turbulent dissipation or specific dissipation. Thus they add extra equations to the RANS equations that must

be solved by the CFD solver such as ANSYS Fluent, CFX or COMSOL. Although the computation time required by a CFD solution to converge is more than just a function of the number of equations solved per grid cell in the computational domain, one-equation turbulence models are computationally more efficient than the two-equation models as expected. There are also zero-equation models which do not add any new equations, but they are not used in this research because of very poor accuracy for flows considered in this chapter.

At the present state of CFD practice, the two most commonly used turbulence models are the Spalart-Allmaras (SA) model and the Shear Stress Transport k-Omega (SST k-Omega) model, which are one-equation and two-equation model, respectively. A relatively new turbulence model, the Wray-Agarwal (WA) model, is also employed in this research to evaluate its performance vis-a-vis SA and SST k-Omega models by comparing the simulations against the available experimental data. The SA model calculates the turbulent eddy viscosity from a transport equation for the eddy viscosity [7]. The SST k-Omega model calculates the kinematic eddy viscosity based on the solution of two transport equations, one for the turbulent kinetic energy and the other for the specific turbulent dissipation rate [8]. The WA model solves the turbulent eddy viscosity using a single equation for the variable "*R*", which represents a ratio of the turbulent kinetic energy to the specific dissipation rate, which are the two variables used in SST k-Omega model [9]. Thus, the one-equation WA model is somewhat related to the two-equation SST k-Omega model. Further details on all the turbulence models are given in later sections of the thesis.

The experimental case employed to test the performance of various turbulence models is the supersonic/hypersonic flow in a compression corner. A compression corner consists of a flat wall upstream of the corner angle with fluid flowing parallel to it. It is followed by a sudden change in the angle of the horizontal wall creating a corner. Thus the corner changes the direction of the

incoming flow suddenly. The schematic of the compression corner is shown in Fig. 2.1. The compression corner is a simple geometry commonly used for studying the shock-boundary layer interaction (SBLI) in the supersonic and hypersonic regimes. The SBLI is especially of interest because of interesting flow features including the shock induced separation; it is often used to test the accuracy of various turbulence models. The physics of shock/turbulent boundary layer interaction is very complex and cannot be simulated from first principles due to the immense computing cost. Therefore, the simulation of SBLI is conduced in this thesis by RANS equations in conjunction with a turbulence model.

Figure 2.1 Schematic of the compression corner geometry. [11]

The compression corner cases simulated in this research are: (a) the flow at Mach 2.85 with corner angles of 8, 16, 20, and 24 degrees considered in the experiments of Settles et al. [10] and (b) the flow at Mach 8 with corner angles of 27, 30, 33, and 36 degrees and at Mach 11 with corners angles of 12 and 36 degrees considered in the experiments of Holden et al. at [11].

In addition to the shock-boundary layer interaction, the higher angle compression corners produce significant recirculation in the corner region. The accurate circulation of the extent of the recirculation region and its effect on the wall static pressure and temperature using various turbulence models is one of the key goals of the thesis. A good turbulence model should be able to reproduce the static pressure and temperature measurements as well as predict the flow features

of shock-boundary layer interaction and the recirculation region in the corner for higher corner angles.

The compression corner is not only an important but simple geometry to study these rich flow features in supersonic/hypersonic flow but also because it is a geometric archetype found in many hypersonic vehicles. Hypersonic weapons, spacecraft reentry vehicles, and even commercial supersonic transport aircraft currently being developed have compression corners in their geometry. Therefore, the study of compressions corners has remained a topic of interest for over half a century. With the availability of advanced computing platforms, they are being studied using the RANS equations with a variety of turbulence models, LES, DES and even DNS to understand the rich flow physics.

2.2 Experimental Case 1 – Settles et al. [10]

The Settles supersonic compression corner case was experimentally performed in the Princeton University's high Reynolds number channel [10]. The experimental setup is shown in Fig. 2.2. A point of note in the experimental setup for this case is that the compression corner model is mounted directly to the floor of the test chamber. This is a significant detail since it implies that the boundary layer has already developed as it reaches the compression corner; it is a continuation of the boundary layer that comes out the nozzle of the test chamber. The experimental boundary layer in this case has thickness of ~2.3 cm as it reaches the compression corner, and to achieve a boundary layer of this thickness requires the upstream length of the flat plate to be of the order of kilometers, which is computationally impractical. Therefore instead of letting the boundary naturally develop from a top hat profile as it reaches the corner, a user-defined boundary layer profile at the inlet of the computational domain is used which has the same characteristic thickness as the turbulent boundary layer measured in the experiment. It requires one meter

upstream length on the flat plate leading up to the compression corner in order to have the same boundary layer profile as in the experiment. It turns out that the choice of the turbulence model does affect the upstream profile to some extent, but not significant.

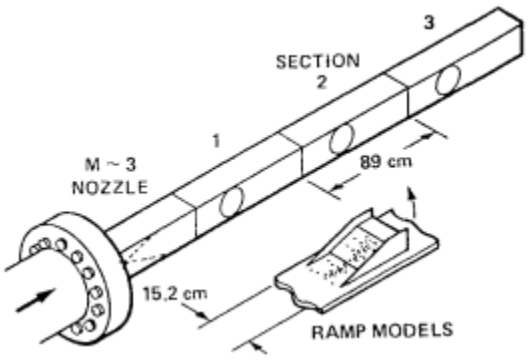

Figure 2.2 Schematic of Settles Mach 3 compression corner experimental setup. [10]

The flow conditions for this case are sufficiently close to the steady state conditions. The wall boundary condition is no-slip and adiabatic. The experimental measurements were taken such that the probe interference was minimal, and the exact extent of the probe interference was tested and found to be negligible [10]. The working fluid was dry air. The collected data included surface pressure, optical flow visualization, velocity profiles, and skin friction. The exact flow conditions in the experiment are described later in the thesis.

2.3 Experimental Case 2 – Holden et al. [11]

The experiments for hypersonic flow in compression corners were conducted by Holden et al. [11] in the CUBRC shock tunnel facilities with test times of the order of 10 ms. These test times, although short, are sufficient to treat the measurements as representative of the steady flow conditions. The pressure measurements were taken using the piezoelectric pressure transducers. The heat transfer measurements were taken with thin film heat transfer gages. The skin friction measurements were taken with the floating element piezoelectric skin friction gages. The working

fluid used was standard dry air. Uncertainty in the freestream conditions was quantified as 5% for the pressures and 1.5% for the Mach number. Uncertainty in the data measurements were 3% for pressures, 5% for the heat transfer, and 12% for the skin friction.

In this experimental case, the compression corner was mounted as part of a geometry that was lifted off the wall of the test chamber as shown in Fig. 2.3. At the leading edge of this test geometry, there is a knife edge. This implies that the boundary layer upstream of the compression corner begins its development at the point of this edge. For this experimental setup, the CFD simulations can be set up with a uniform velocity inlet flow condition exactly at the horizontal point of the edge, and the development of the boundary layer is entirely handled by the numerical solver with the turbulence model.

For the Mach 11 cases, the upstream length of the flat plate from the knife-edge to the compression corner was 40.3 inches (1.02362 m). For the Mach 8 cases, it was 39.2 inches (0.99568 m) [11]. The exact flow conditions used in the CFD simulation cases are described later in the thesis.

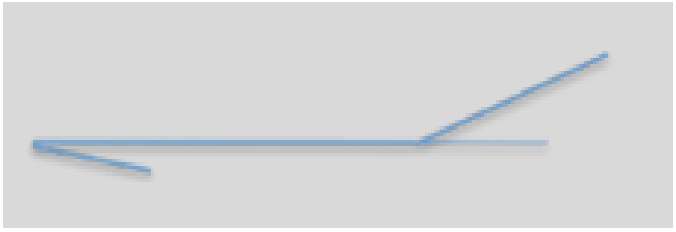

Figure 2.3 General layout (side view) of the knife-edged test stand for the Holden's compression corner experiments

2.4 Computational Setup

The computational solver used in this study is a steady-state density-based RANS compressible equation solver in ANSYS Fluent. A second-order upwind scheme is employed for the convection terms and viscous terms are central-differenced. The geometry modeling, meshing,

and post-processing are all done using the built-in tools provided by the ANSYS Workbench package.

2.4.1 Geometry of Flow Domain

The geometries of flow domain are simple 2D planar compression corners generated using ANSYS SpaceClaim as a part of the ANSYS Workbench tools suite. For the Settles experimental test cases, upstream leading edge of the flat plate for inlet flow is at 1-meter from the compression corner. For the Holden's experimental test cases, the leading edge of the flat plate is at 1.02362 m for the Mach 11 cases and is at 0.99568 m for the Mach 8 cases. The dimensions of the ramp in both cases were modeled following the dimensions in the experimental ramp; both experimental setups have ramps of sufficient length to create an outlet boundary condition in Fluent [10, 11]. Figure 2.4. shows a typical flow domain geometry of the 16-degree Settles' compression corner.

Figure 2.4. Flow domain geometry of the 16-degree Settles' compression corner.

Mesh in the Flow Domain:

The mesh in the geometry of the flow domain consists of a combination of three different types of 2D quadrilateral polygons as shown in Fig. 2.5. From left to right, the first set of polygons

are simple rectangles that represents the inlet region of the flow domain just before the start of the compression corner ramp. It is in this region of the flow domain that the boundary layer is generated for the Holden's cases, and the boundary layer develops from the upstream specified velocity profile (by a UDF in ANSYS) in the Settles' cases.

Next, smaller rectangles are put in the center of the geometry in a length of 0.1 m. The reason for this being a separate mesh from the first is twofold. First, it can be anticipated just from an intuitive understanding of supersonic compressible flow that in most of the cases with large corner angles, one should expect the CFD results to contain a significant recirculation in the region of the compression corner. This region has a finer mesh than needed in the upstream boundary layer region. The third region in the flow domain represents the point of the compression corner to the outlet of the flow domain, which is the end of the flow domain of the compression corner. The mesh is again fine in the corner region because of the shock/boundary layer interaction.

In meshing, there are several important factors to take into consideration. First, there must be sufficient mesh refinement in the region near the solid surface of the domain to capture the high gradients associated with the boundary layer. To assure that the mesh is sufficiently refined in this region, a dimensionless cell distance value, $y+$, is used. In many subsonic CFD applications, a $y+$ value of 1 is the standard. However, because this flow is highly energetic at Mach 2.85, and since the WA turbulence model was found to be highly sensitive to the near-wall flow behavior, this study employed a very fine mesh with $y+$ value of 0.05. In addition to the $y+$ value, the high growth rates in the mesh near the wall must also be avoided. This is due to the inaccuracies that occur in the CFD numerical schemes when the size of one mesh cell with respect to its neighbor is greater than around 1.2. This means that, while the near-wall cells must be highly refined, and the cells outside the boundary layer can be coarse, there must be a smooth transition in cell size

between the two where the growth rate does not exceed 1.2. Figure 2.5 shows an example of the mesh with mesh growth rate of 1,2 near the wall.

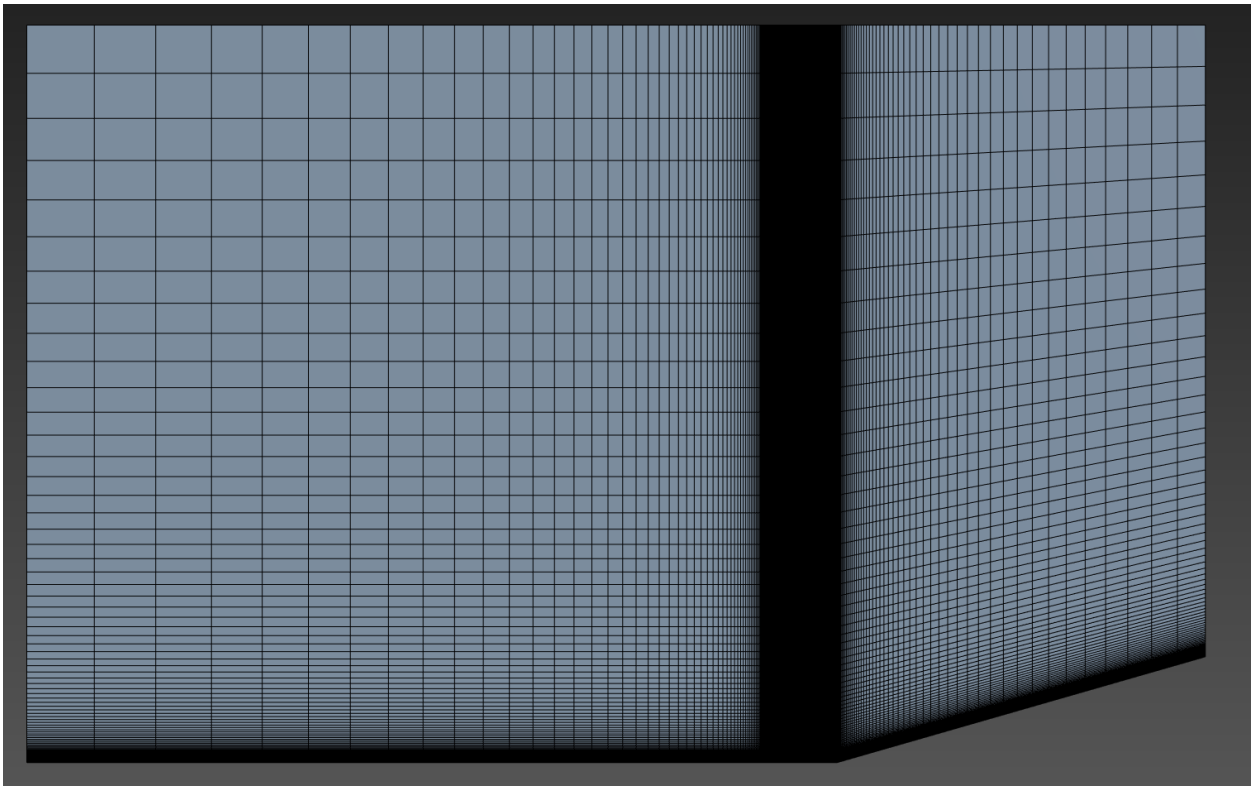

Figure 2.5 Mesh inside the flow domain of 16-degree Settles' compression corner.

For the higher corner angles, a recirculation region is expected in the corner region beginning slightly upstream of the corner and ending on the compression ramp slightly downstream of the corner. A proper mesh can be generated for the recirculation region by creating a zone upstream of the corner that is more finely meshed with a smooth transition both upstream and downstream of this finely meshed zone. Figure 2.6 shows the mesh in the recirculation region for a 24-degree compression corner. Notice that the growth rate and number of cells in the zones left and right of this finely meshed region are such that the size of the cells at the interface between the zones are near equal ensuring that no part of the mesh exceeds a growth rate of 1.2.

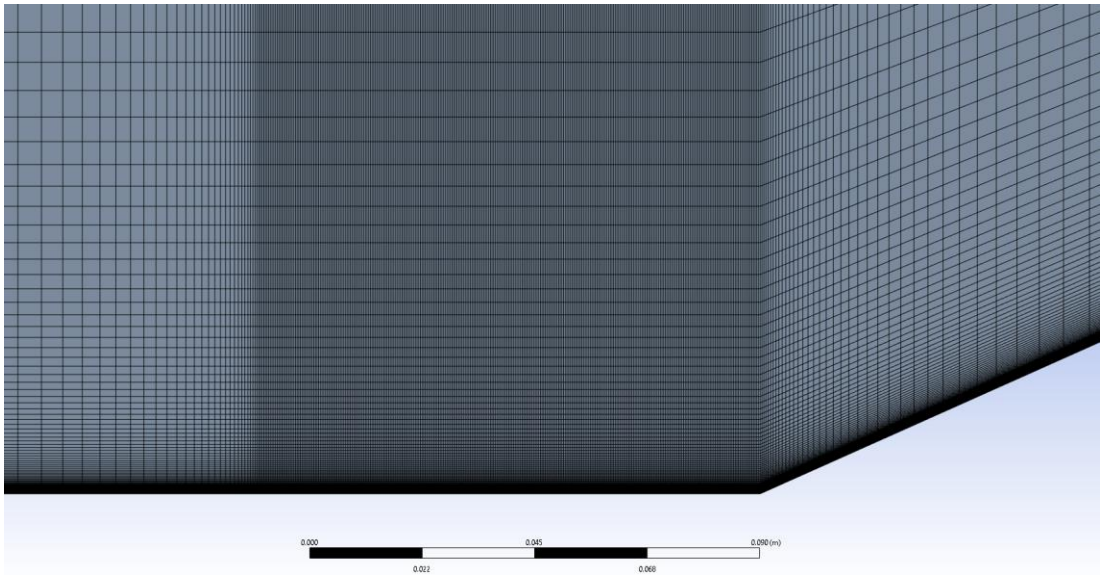

Figure 2.6 Mesh in the recirculation region of a 24-degree compression corner.

2.4.3 Boundary Conditions – Settles's Experimental Test Cases

Inlet boundary conditions for the 24-degree Settles' case are listed in Table 2.1. The boundary conditions do not vary significantly for the other three experimental cases with different corner angles. The inlet boundary condition was set in Fluent as pressure-inlet type, which is the recommended setting for compressible flow cases. The static pressure on the inlet boundary is defined at all points as 23,457 Pa. To achieve the desired boundary layer thickness from a user-defined boundary layer profile, a piecewise function was written where all points at a distance greater than 2.3 cm from the wall had a total pressure or stagnation pressure of 689,010 Pa. Between the wall and a height of 2.3 cm, the total pressure value varied linearly from 23,457 Pa (the same as the static pressure) to 689,010 Pa. In terms of the velocity distribution in the inlet boundary layer profile, there is an exponential growth in velocity from zero at the wall to the freestream velocity 2.3 cm away from the wall. The piecewise user-defined expression used for the inlet boundary condition in Fluent for the total pressure is as follows:

IF (y <= 0.023[m], 23457[kg m^-1 s^-2] + 665553[kg m^-1 s^-2] *(y/0.023[m]), 689010[kg m^-1 s^-2])

Table 2.1 Flow Conditions in the experiments of Settles et al. [10]

Freestream Mach Number	M_∞	2.85
Freestream Temperature	T_∞	268 K
Freestream Static Pressure	P_∞	23.5×10^3 Pa
Freestream Density	ρ_∞	$0.6815\ kg/m^3$
Reference Dynamic Viscosity	μ_{ref}	$1.7894 \times 10^{-5}\ kg/(m \cdot s)$
Freestream Velocity	V_∞	588.59 m/s

The top boundary of the geometry is modelled using the 'Wall' boundary condition in ANSYS Fluent. It can be modelled as a wall because it is sufficiently far away from the region of interest and it is outside the shock, therefore it will not affect the results in the corner. The wall conditions used for the Settles' cases are an adiabatic smooth wall with no-slip boundary condition. These boundary conditions are used for all walls present in the geometry. The outlet is modelled as a pressure-outlet boundary condition with a no reverse flow condition.

2.4.4 Boundary Conditions – Holden's Experimental Test Cases

The boundary conditions used in the Holden's Mach 8 experimental test cases for various corner angles are given in Tables 2.2-2.5. The process for determining the boundary conditions was to set the inlet boundary condition to a pressure-far-field type. This is a boundary condition in Fluent in which a static pressure and Mach number are specified, as well as the flow direction. First, the inlet flow temperature was set as specified in the experimental data. Then, the inlet flow pressure was varied until the inlet density matched the value in the experiment. Then, the Mach number was varied slightly from that which was specified in the experiment to match the flow velocity at the inlet to the specified value. It is important to note that the variation in Mach number in this process difd not exceed not exceed 1.5%, as was the uncertainty in the Mach number specified by Holden et al. [11]. The exact flow conditions at inlet are given in Tables 2.2 to 2.5.

Table 2.2 Holden's inlet flow conditions at Mach 8 for 27-degree corner

Freestream Mach Number	M_∞	8.23
Freestream Temperature	T_∞	71.7 K
Freestream Static Pressure	P_∞	10228 Pa

Table 2.3 Holden's inlet flow conditions at Mach 8 for 30-degree corner

Freestream Mach Number	M_∞	8.266
Freestream Temperature	T_∞	68.9 K
Freestream Static Pressure	P_∞	10007 Pa

Table 2.4 Holden's inlet flow conditions at Mach 8 for 33-degree corner

Freestream Mach Number	M_∞	8.20
Freestream Temperature	T_∞	70.45 K
Freestream Static Pressure	P_∞	9910 Pa

Table 2.5 Holden's inlet flow conditions at Mach 8 for 36-degree corner

Freestream Mach Number	M_∞	8.22
Freestream Temperature	T_∞	70 K
Freestream Static Pressure	P_∞	10027 Pa

2.4.5 Numerical Methods

The generally accepted rule of thumb in aerodynamics is that a flow must be considered compressible if it is above a Mach number of 0.3. Obviously, this puts all the cases considered in this thesis well into the compressible regime, and therefore pressure-based numerical solvers are not inappropriate for computing these flows. Instead, the flows were computed using numerical methods based on the density-based formulation of the Reynolds-Averaged Navier-Stokes (RANS) equations using ANSYS Fluent. The gravitational force was not included in the calculations since the effect of gravity on the fluid particles moving with such high energy is negligible.

Due to the high energy nature of the flow, conservation of energy equation was used to ensure that the temperature in the flow was calculated accurately. This was done by enabling the "energy equation" in Fluent. For all the cases besides the heat transfer cases, the working fluid used was standard dry air. The wall material used was set to aluminum, although for the pressure field computations, it did not matter since all the walls were set as adiabatic.

The numerical method employed was explicit Roe-FDS solver. Implicit formulation was found to be unstable even with CFL numbers less than 1. The spatial discretization of the gradients was done by the least squares cell based technique, and for the initial runs the convection terms in RANS equations and the turbulence models were calculated using a first order upwind scheme for reasons of numerical stability. Once the solution converged and was stable, the numerical method was switched to a second-order upwind scheme. The convergence was considered achieved when all residuals of the governing equations and flow variables became less than E10-4.

The implementation of the WA turbulence model required special consideration compared to the implementation of SST k-Omega and SA models, since the WA model is not included as a built-in turbulence model in the ANSYS Fluent. For WA model, a user-defined function (UDF) was implemented which was provided by the CFD lab research group. The WA model had trouble starting a case on its own, therefore the SA model was used for the first few iterations before the WA model was applied. The WA model implementation guide recommends that the SA model be run on a case for the first 50 iterations, but it was found that some cases would diverge when the WA model was applied after 50 iterations of the SA model. Therefore, the SA model with first order upwind scheme was used for the first 1000-5000 iterations, just to be safe, and then the WA model was applied.

The Courant number, also commonly known as the Courant-Friedrichs-Lewy (CFL) number, is a dimensionless value that represents the number of cells that a traveling wave will cross per iteration. For maximum stability, the CFL number should be kept below 1 for both the explicit and implicit algorithms. During the convergence process, a user can increase the CFL number significantly without triggering divergence so long as the solution has sufficiently converged. Increasing the CFL number allows the solution to converge quickly in fewer iterations.

Since the supersonic and hypersonic flow cases tend to be generally numerically more unstable, therefore a constant CFL number of 0.8 was used for reasons of numerical stability. The under-relaxation factors were adjusted on a case-by-case basis but were always kept below 1.

2.4.6 Grid Independence of Solution

It is important in CFD simulations to ensure that a sufficiently refined grid is used such that the computed solutions are grid independent. This issue is generally resolved by conducting a grid-independence of solution study in which the solution is computed on at least three different grids and then the numerical value of a physical quantity computed on the three grids is compared. The number of mesh elements on the three grids vary from a small number to a large number doubling from coarse grid with lowest number of mesh points to medium grid with double the number of mesh points to fine grid with double the number of mesh points on the intermediate grid. For example, three grids were used to compute the Holden's case at Mach 8.2 with 36-degree corner angle and the physical value of drag force on the sloped segment of the compression corner was tracked. The medium grid gave a drag value of 90.0 kN/m whereas the refined grid computed a drag value of 89.8 kN/m. The percentage difference between the two drag values is 0.22% which is very small. Therefore, it was concluded that intermediate grid was sufficient to provide grid independent solution. All solutions presented in this thesis are grid independent.

2.4.6 Thermal Wall Boundary Condition

Two sets of boundary conditions were used for the Holden's Mach 8 cases with different corner angles. The first boundary condition used was adiabatic for calculating the velocity and static pressure field, and the recirculation region in the corner. The isothermal wall boundary condition was also used for computing the wall shear stress and heat transfer rates. The results

from the two thermal boundary conditions were compared to assess the change in the energy of the flow due to the heat transfer at the wall due to isothermal and adiabatic wall boundary conditions. A computational study was conducted for Holden's case at Mach 8.2 with 33-degree corner angle to compare the static pressure results in the corner region using the isothermal and adiabatic wall boundary conditions. The computed turbulent flow results using the RANS equations with the SA turbulence are shown in Fig. 2.7. It can be seen from this figure that there is little effect of the two boundary conditions on results for the static pressure in the corner region. This results assures that the results for pressure and velocity field computed by using the adiabatic wall boundary condition can be considered reasonably accurate for the study of shock/boundary layer interaction in the corner region for supersonic/hypersonic flow. However, this is unlikely be true for heat transfer results.

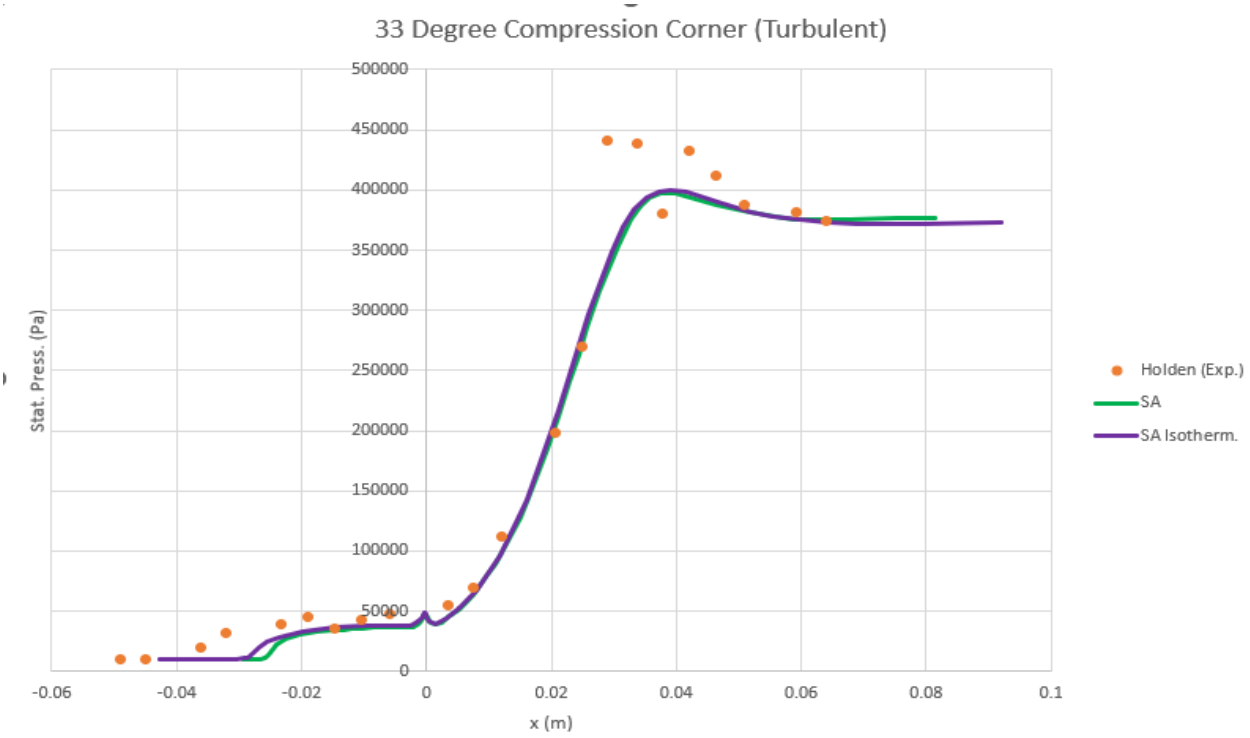

Figure 2.7 Comparison of the experimental static pressure results for the Holden's test case at Mach 8.2 and 33-degree corner angle with RANS computations and SA model using the isothermal and adiabatic wall conditions.

2.5 Turbulence Models

Three turbulence models are used in this study, namely the SA, SST k-ω, and WA turbulence models. The SA model is given by the transport equation for kinematic turbulent viscosity as follows [7]:

$$\frac{\partial}{\partial t}(\rho\nu) + \frac{\partial}{\partial x_i}(\rho\nu u_i) = G_\nu + \left[\frac{\partial}{\partial x_j}\left\{(\mu + \rho\nu)\frac{\partial \nu}{\partial x_j}\right\} + C_{b2}\rho\left(\frac{\partial \nu}{\partial x_j}\right)^2\right] - Y_\nu + S_\nu \qquad (2.1)$$

where ν and μ are the kinematic turbulent viscosity and dynamic laminar viscosity respectively. The details of the model can be found in Ref. [7].

The SST *k-ω* model is given by the two transport equations (2.2) and (2.3) for *k* and *ω* respectively as shown below [8]:

$$\frac{\partial k}{\partial t} + U_j\frac{\partial k}{\partial x_j} = P_k - \beta^* k\omega + \frac{\partial}{\partial x_j}\left[(\nu + \sigma_k\nu_T)\frac{\partial \omega}{\partial x_j}\right] \qquad (2.2)$$

$$\frac{\partial \omega}{\partial t} + U_j\frac{\partial \omega}{\partial x_j} = \alpha S^2 - \beta\omega^2 + \frac{\partial}{\partial x_j}\left[(\nu + \sigma_\omega\nu_T)\frac{\partial \omega}{\partial x_j}\right] + 2(1 - F_1)\sigma_{\omega 2}\frac{1}{\omega}\frac{\partial k}{\partial x_j}\frac{\partial \omega}{\partial x_i}. \qquad (2.3)$$

The details of the model can be found in Ref. [8].

The Wray-Agarwal (WA) model is a one-equation model that has been derived from the two-equation *k-ω* model. It combines the benefits of the *k-ω* model in the near wall region and that of *k-ε* model in the free stream region of the flow. The $R = (k/\omega)$ variable in the WA model is defined by the following equation [9]:

$$\frac{\partial R}{\partial t} + \frac{\partial u_j R}{\partial x_j} = \frac{\partial}{\partial x_j}\left[(\nu + \sigma_R R)\frac{\partial R}{\partial x_j}\right] + C_1 RS + f_1 C_{2k\omega}\frac{R}{S}\frac{\partial R}{\partial x_j}\frac{\partial S}{\partial x_j} - (1 -$$

$$f_1)min\left[C_{2k\epsilon}\left(\frac{\frac{\partial S}{\partial x_j}\frac{\partial S}{\partial x_j}}{S^2}\right), C_m\frac{\partial R}{\partial x_j}\frac{\partial R}{\partial x_j}\right] \qquad (2.4)$$

The details of the WA model can be found in Ref. [9]. The SA and SST k-ω models are included in ANSYS Fluent. The WA model, however was added using the Fluent's built in system for user-defined functions (UDFs) to define the function R, which is related to the turbulent eddy viscosity in the flow. The UDF used in this thesis is for the implementation of WA2017m version of the WA model.

Chapter 3: Results for Supersonic/ Hypersonic Flow in Compression Corner

3.1 Settles' Mach 2.85 Cases

3.1.1 Visual Results

The results collected from the Settles' compression corner experiment include the shadowgraphs that clearly show the locations of the shock [10]. These shadowgraph images can be compared to the CFD contour plots to qualitatively compare the experimental and CFD results for the behavior of the shock. The comparisons are shown in Figs. 3.1 to 3.13. The flow quantity plotted in the CFD contour plots is the static pressure.

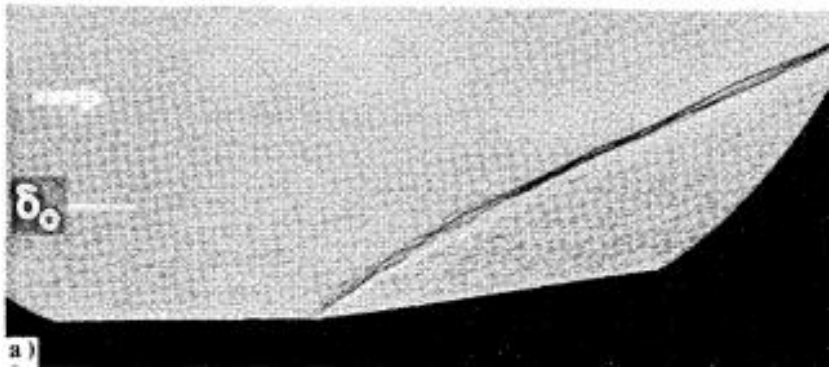

Figure 3.1. Shadowgraph of Settles' case at M = 2.85 and 8-degree corner angle [10].

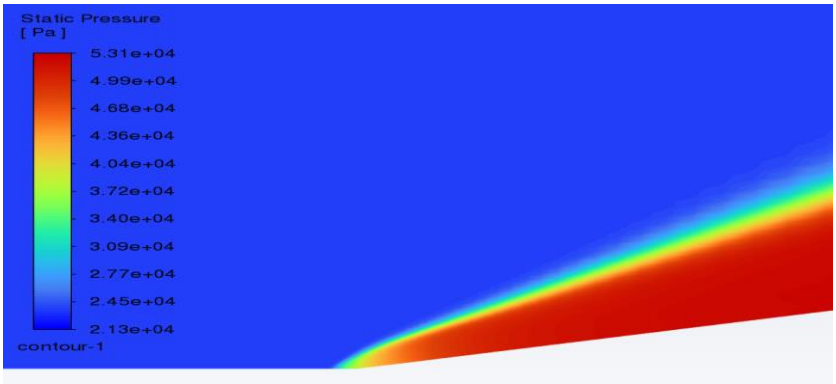

Figure 3.2 Computed static pressure contours for Settles' case at M = 2.85 and 8-degree corner angle using the SST k-Omega turbulence model

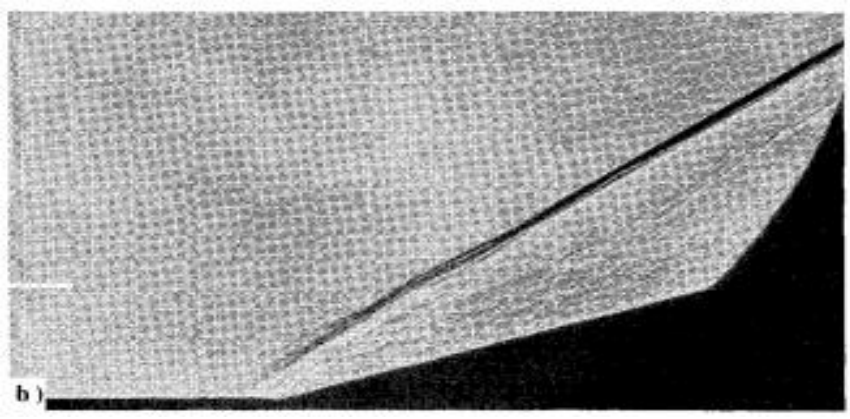

Figure 3.3. Shadowgraph of Settles' case at M = 2.85 and 16-degree corner angle [10].

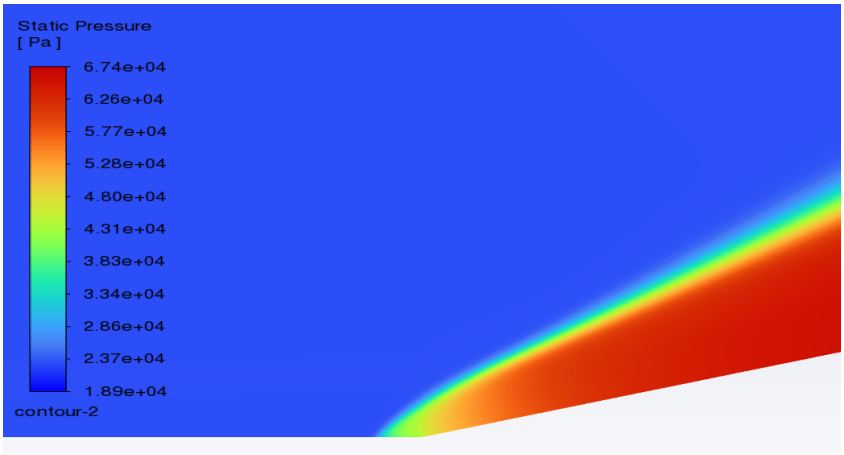

Figure 3.4 Computed static pressure contours for Settles' case at M = 2.85 and 8-degree corner angle using the SA turbulence model

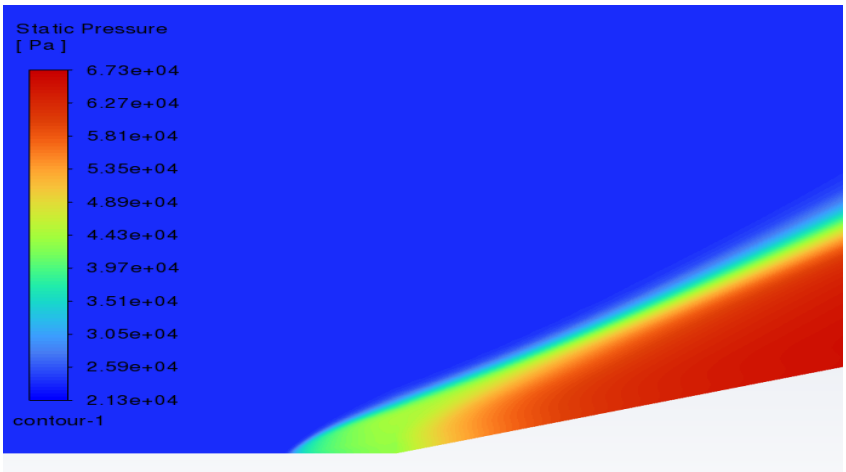

Figure 3.5 Computed static pressure contours for Settles' case at M = 2.85 and 16-degree corner angle using the SST k-Omega turbulence model

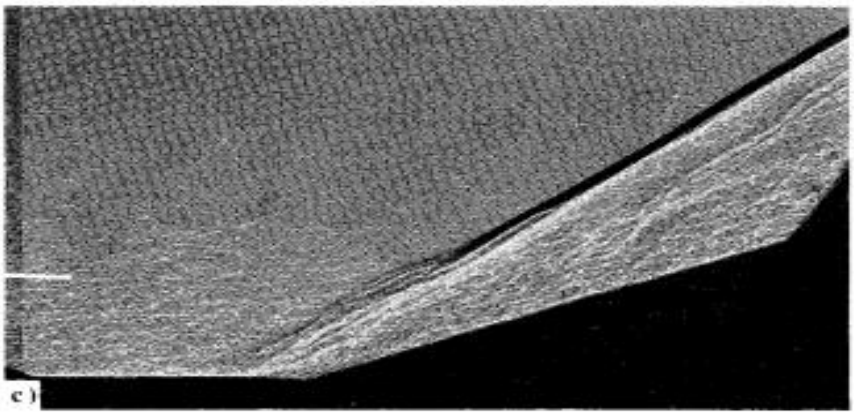

Figure 3.6. Shadowgraph of Settles' case at M = 2.85 and 20-degree corner angle [10].

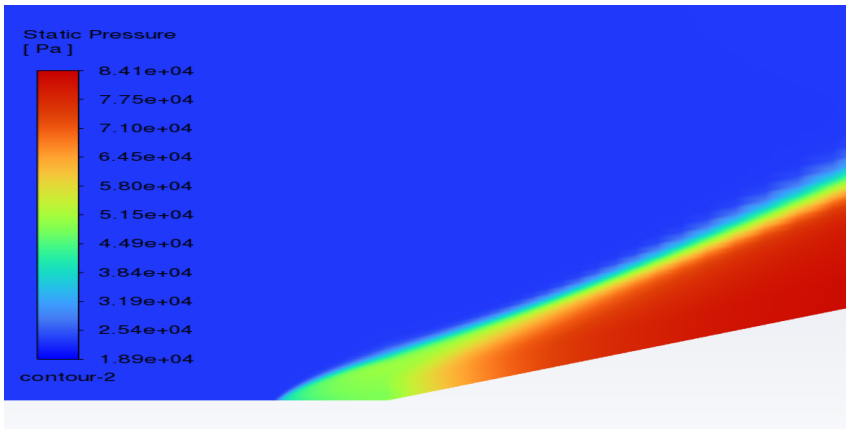

Figure 3.7 Computed static pressure contours for Settles' case at M = 2.85 and 20-degree corner angle using the SA turbulence model

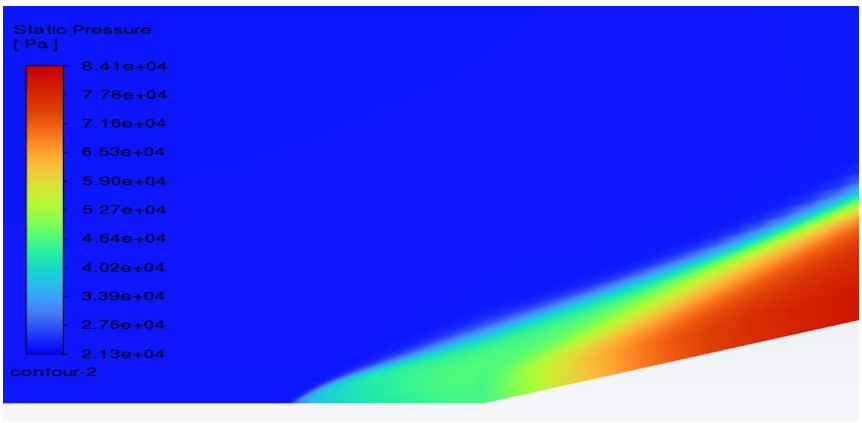

Figure 3.8 Computed static pressure contours for Settles' case at M = 2.85 and 20-degree corner angle using the SST k-Omega turbulence model

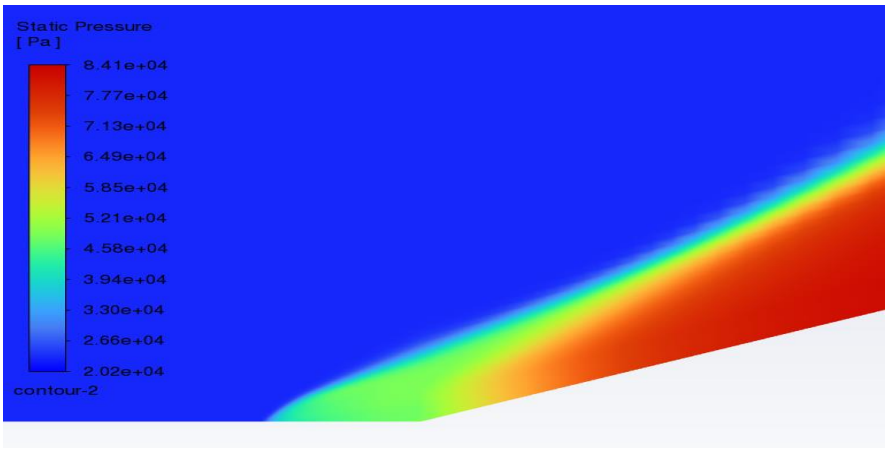

Figure 3.9 Computed static pressure contours for Settles' case at M = 2.85 and 20-degree corner angle using the WA turbulence model

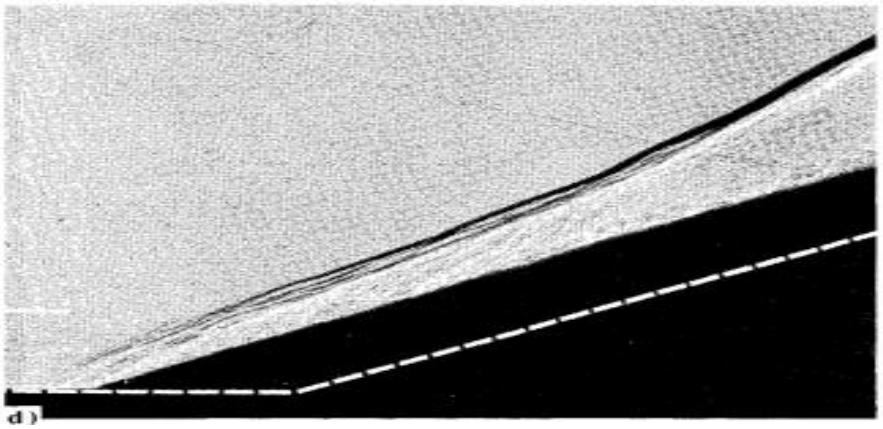

Figure 3.10. Shadowgraph of Settles' case at M = 2.85 and 24-degree corner angle [10].

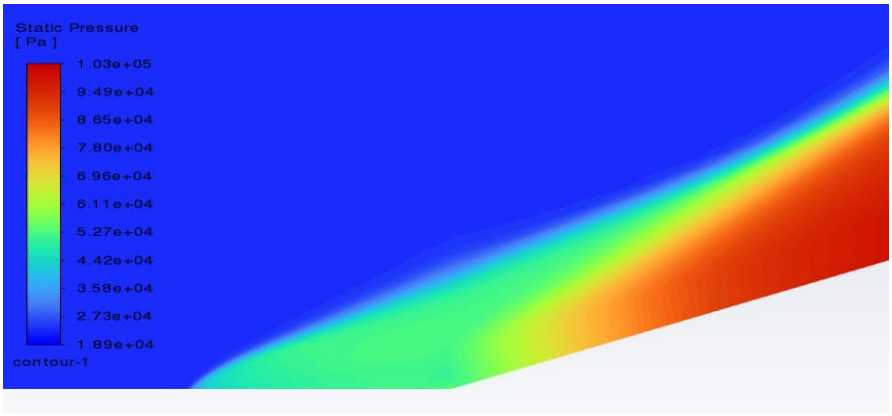

Figure 3.11 Computed static pressure contours for Settles' case at M = 2.85 and 24-degree corner angle using the SA turbulence model

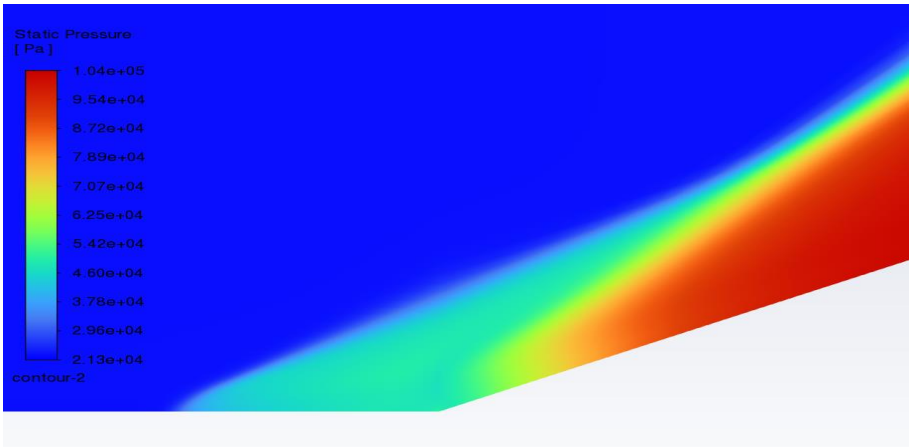

Figure 3.12 Computed static pressure contours for Settles' case at M = 2.85 and 24-degree corner angle using the SST k-Omega turbulence model

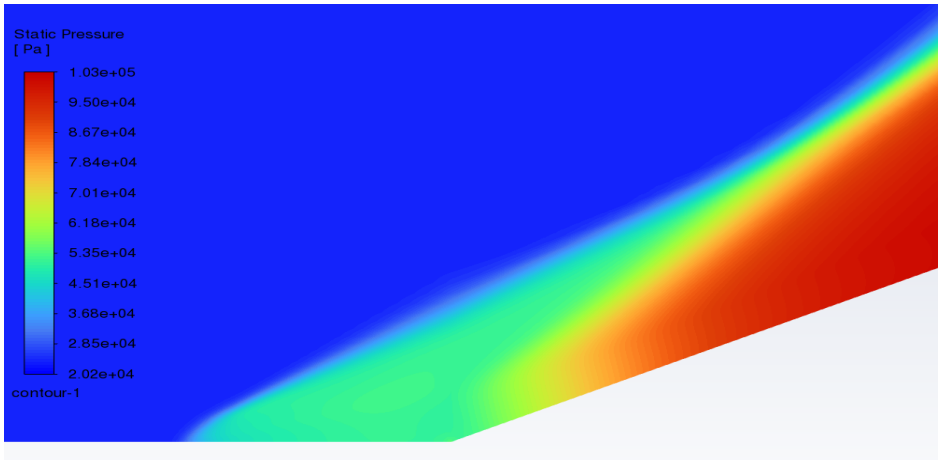

Figure 3.13 Computed static pressure contours for Settles' case at M = 2.85 and 20-degree corner angle using the WA turbulence model

The details of the shock boundary layer interaction can be seen with contour plots of velocity magnitude. The zoomed-in views of the shock boundary layer interaction for each CFD case are shown in Figs. 3.14 to 3.21.

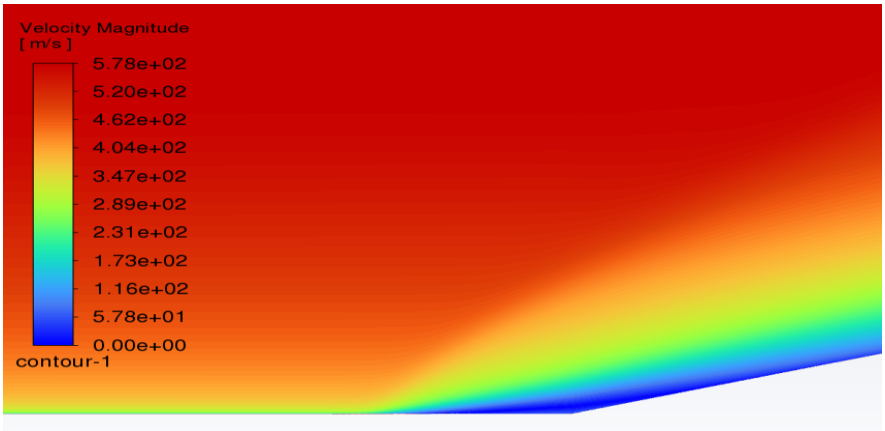

Figure 3.14 Zoomed-in view of corner region showing shock-boundary layer interaction for Settles' case at Mach 2.85 for 16-degree corner angle using the SA model.

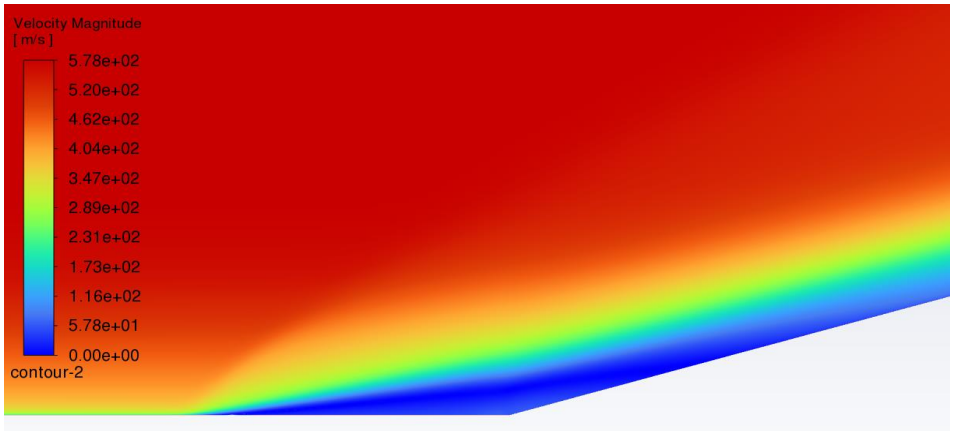

Figure 3.15 Zoomed-in view of corner region showing shock-boundary layer interaction for Settles' case at Mach 2.85 for 16-degree corner angle using the SST k-Omega model.

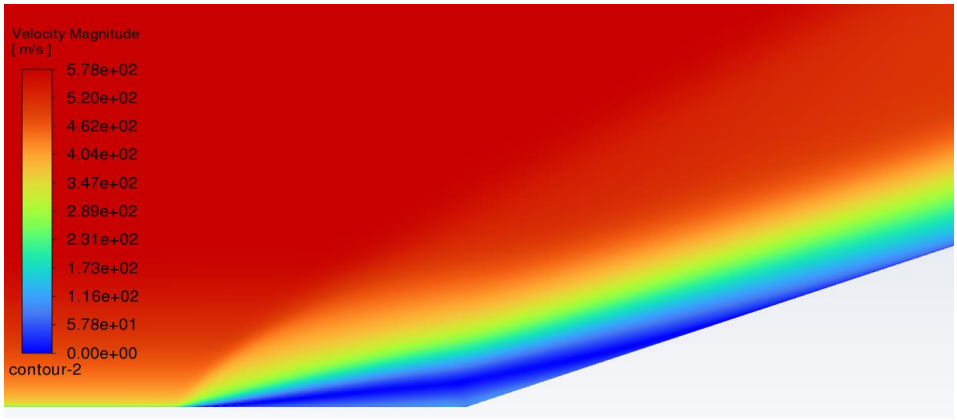

Figure 3.16 Zoomed-in view of corner region showing shock-boundary layer interaction for Settles' case at Mach 2.85 for 20-degree corner angle using the SA model.

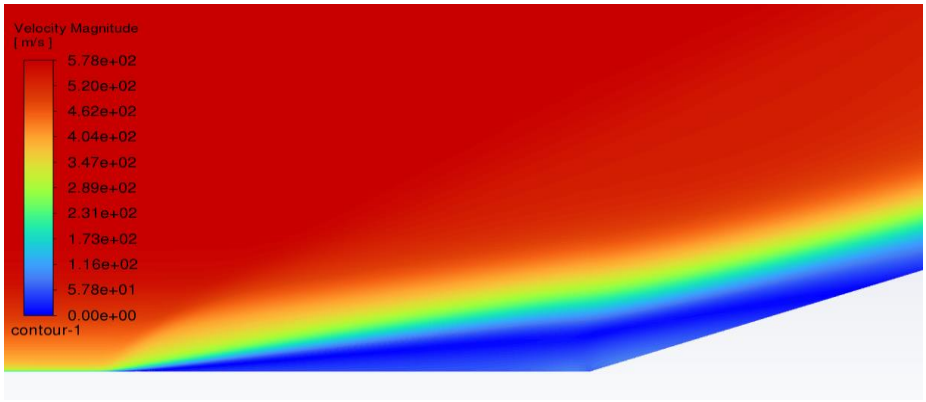

Figure 3.17 Zoomed-in view of corner region showing shock-boundary layer interaction for Settles' case at Mach 2.85 for 20-degree corner angle using the SST k-Omega model.

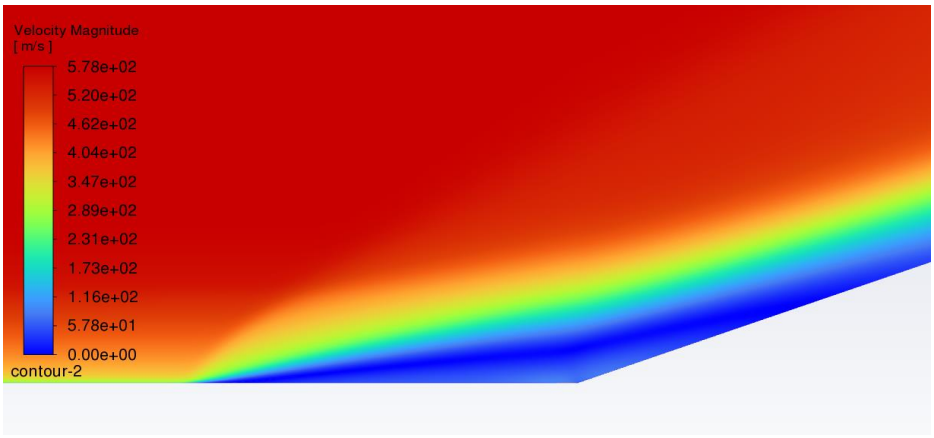

Figure 3.18 Zoomed-in view of corner region showing shock-boundary layer interaction for Settles' case at Mach 2.85 for 20-degree corner angle using the WA model.

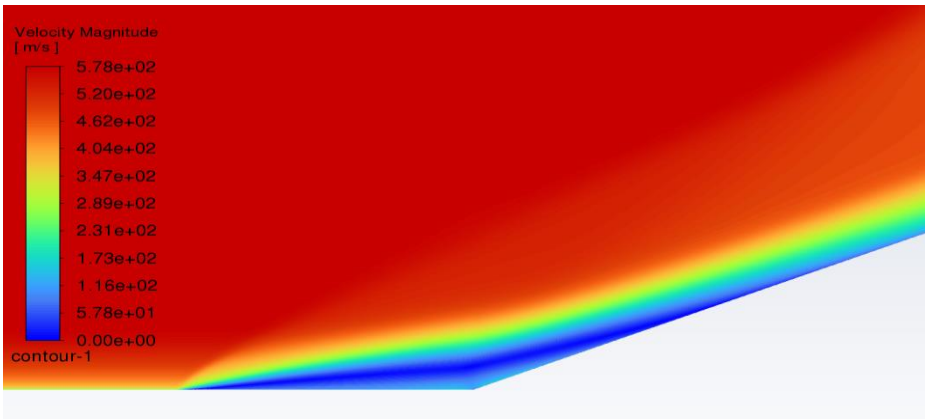

Figure 3.19 Zoomed-in view of corner region showing shock-boundary layer interaction for Settles' case at Mach 2.85 for 24-degree corner angle using the SA model.

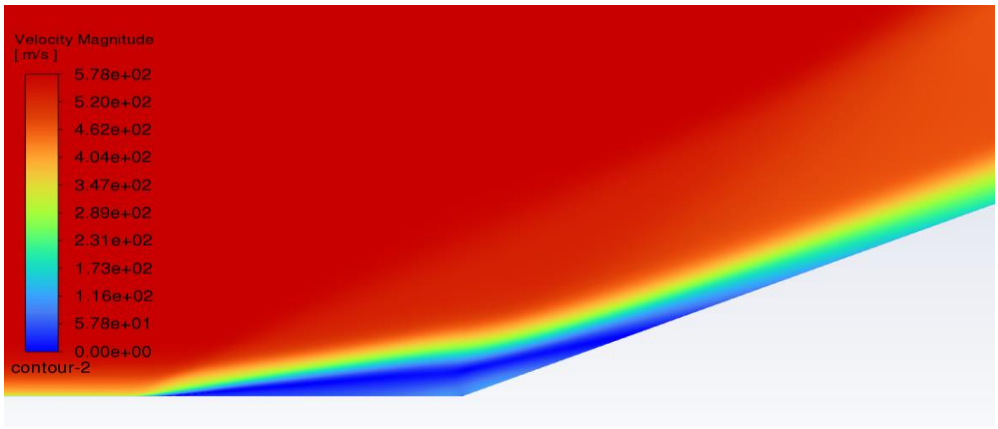

Figure 3.20 Zoomed-in view of corner region showing shock-boundary layer interaction for Settles' case at Mach 2.85 for 24-degree corner angle using the SST k-Omega model.

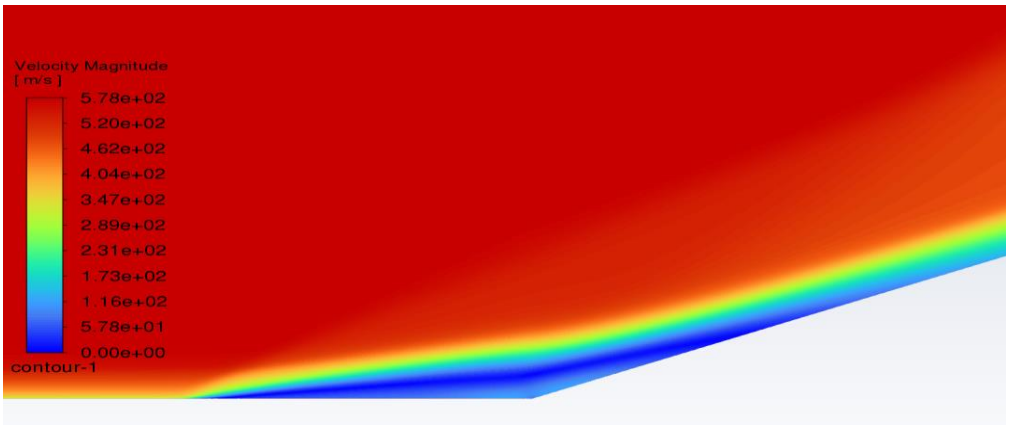

Figure 3.21 Zoomed-in view of corner region showing shock-boundary layer interaction for Settles' case at Mach 2.85 for 24-degree corner angle using the WA model.

3.1.2 Static Pressure Results

Figures 3.22 -3.24 show the comparison of the static pressure distribution along the bottom wall and the slope of the compression corner for Settles' case at Mach 2.85 for corner angles of 16-, 20- and 24-degrees using the three turbulence models. Results show that SA model is in best agreement with experimental data followed by the WA model and then the SST k-Omega model.

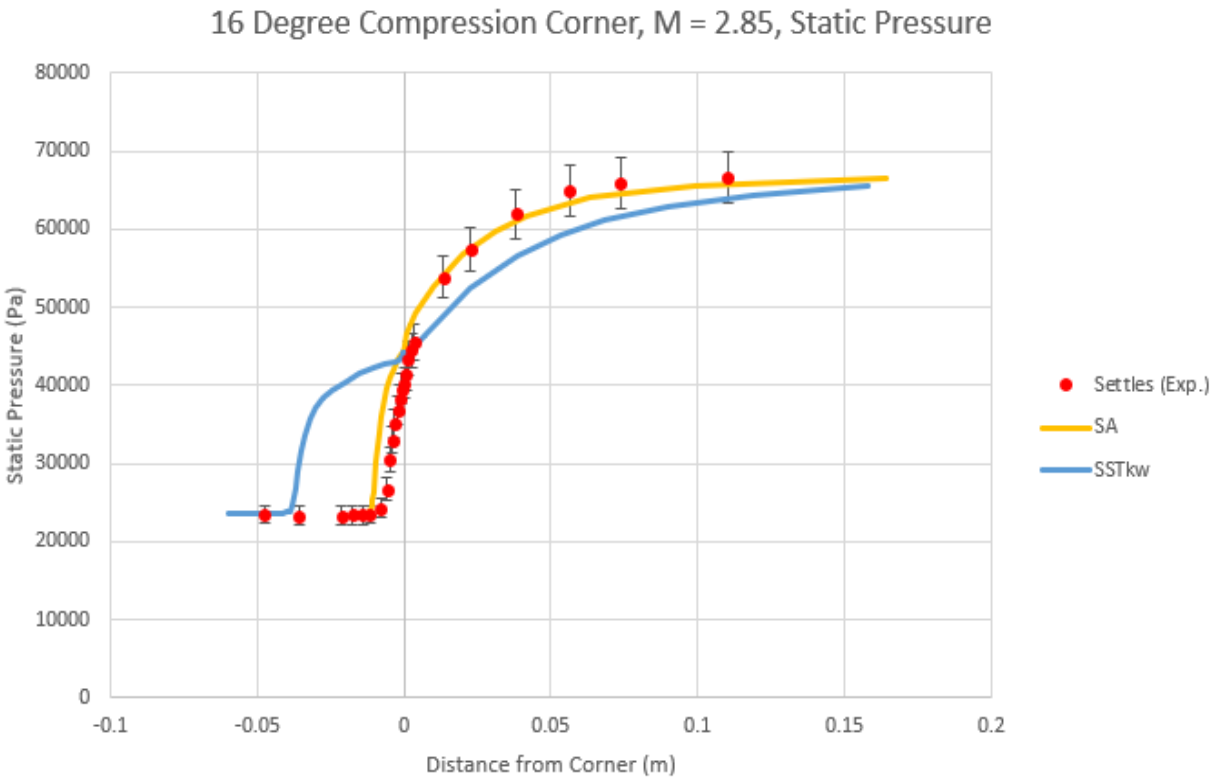

Figure 3.22 Comparison of the static pressure distribution along the bottom wall and the slope of the compression corner for Settles' case at Mach 2.85 for corner angle of 16 degrees using the SA and SST k-Omega turbulence model.

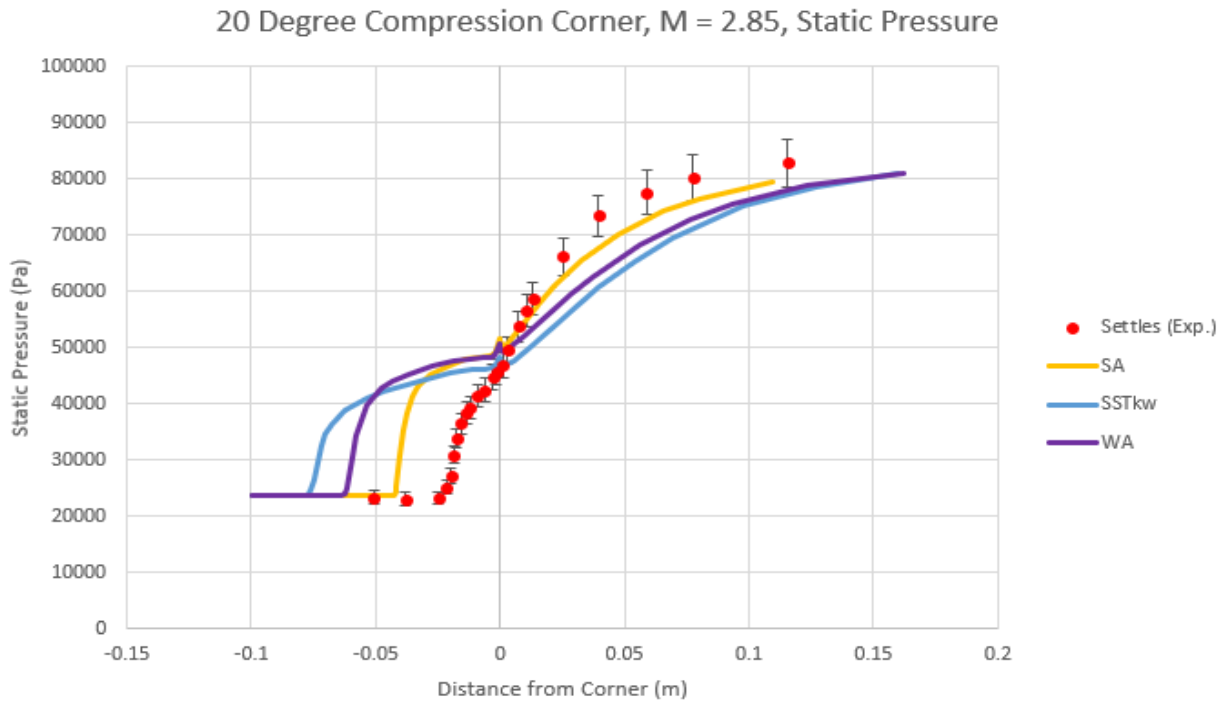

Figure 3.23 Comparison of the static pressure distribution along the bottom wall and the slope of the compression corner for Settles' case at Mach 2.85 for corner angle of 20 degrees using the three turbulence models.

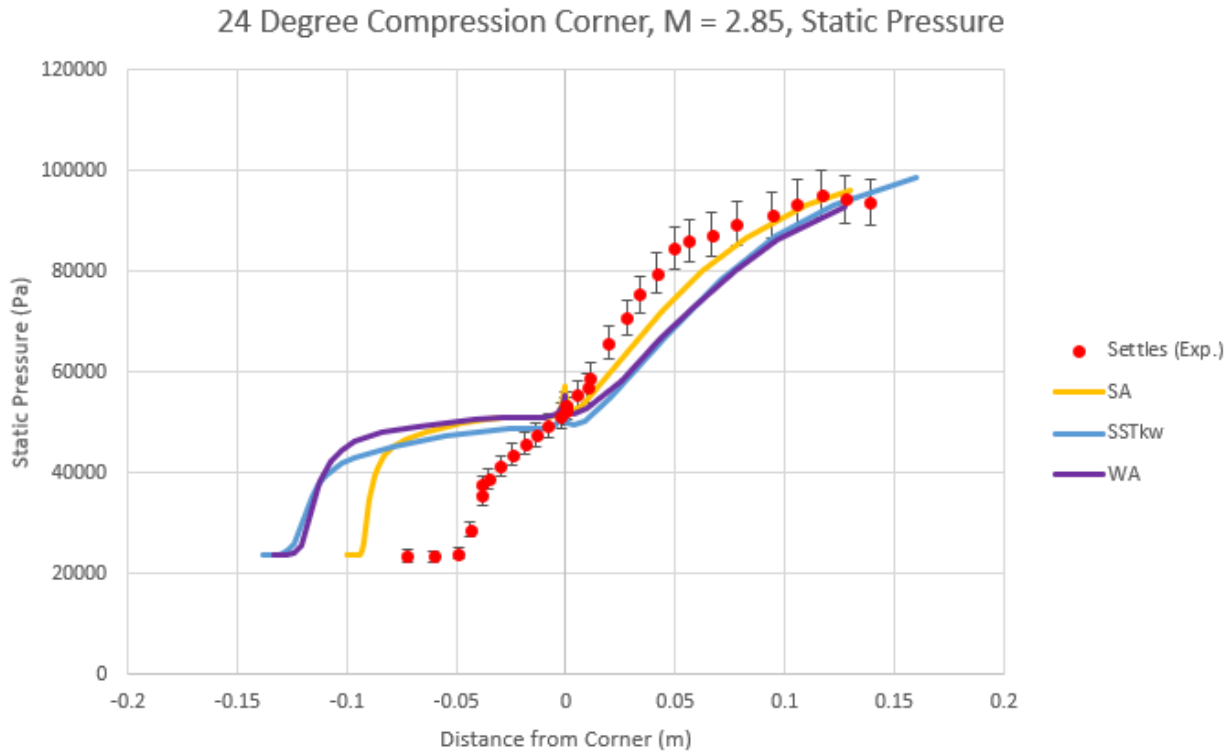

Figure 3.24 Comparison of the static pressure distribution along the bottom wall and the slope of the compression corner for Settles' case at Mach 2.85 for corner angle of 24 degrees using the three turbulence models.

3.1.3 Recirculation Region in the Corner

It turns out that the lowest corner angle for Settles's cases at Mach 2.85 that exhibits a significant recirculation region in the corner is 20 degrees. The circulation region can be visualized in the CFD results by tracking the particle path-lines (same as the streamlines due to steady nature of the flow) in the recirculation region. These streamlines are plotted for the 20- and 24- degree cases in Figs. 3.25 - 3.30 for various turbulence models.

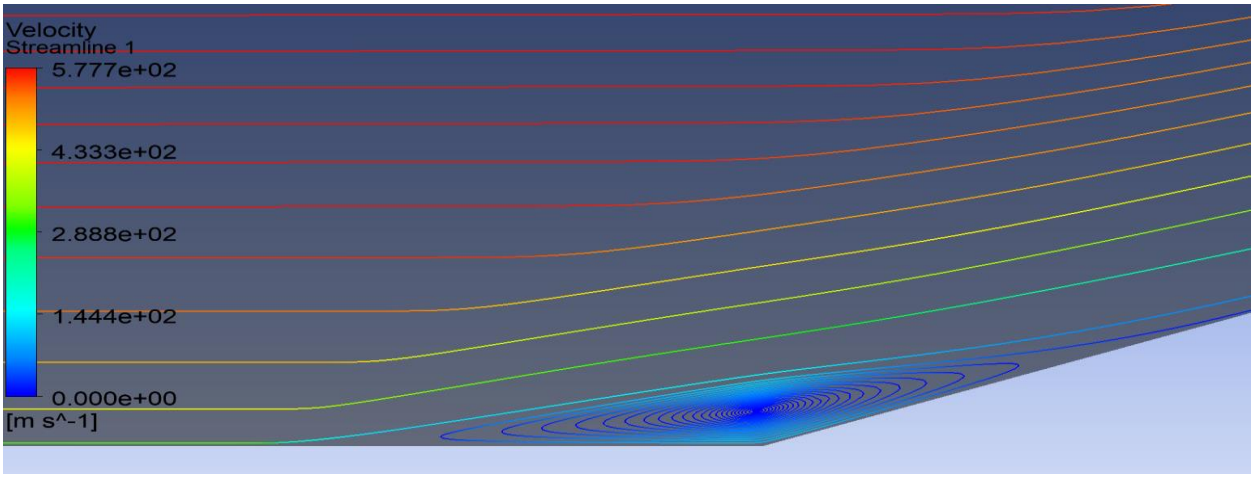

Figure 3.25 Streamlines in the recirculation region for Settles' case at Mach 2.85 for 20-degree corner angle computed using the SA model.

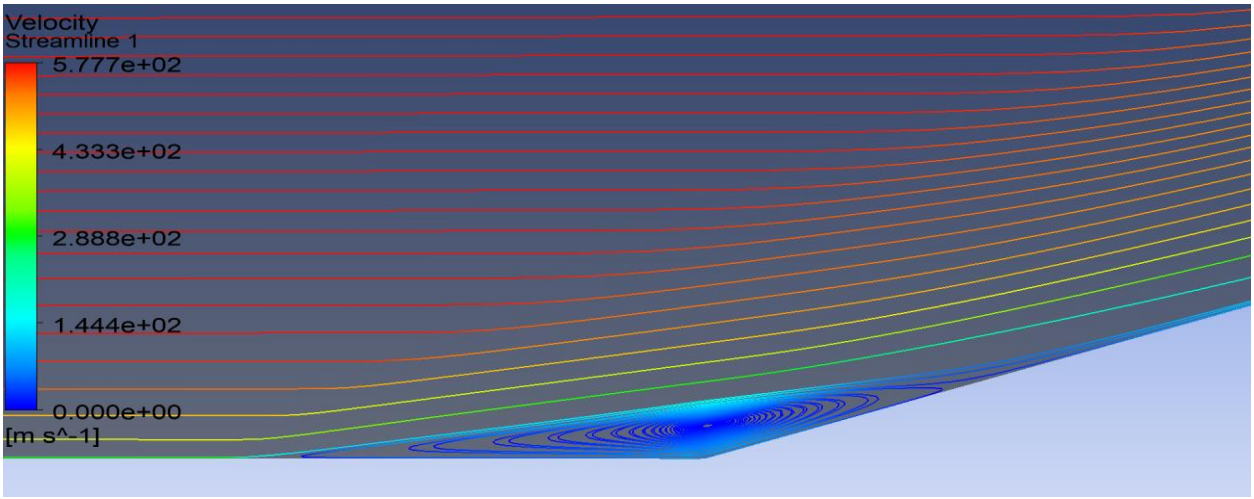

Figure 3.26 Streamlines in the recirculation region for Settles' case at Mach 2.85 for 20-degree corner angle computed using the SST k-Omega model.

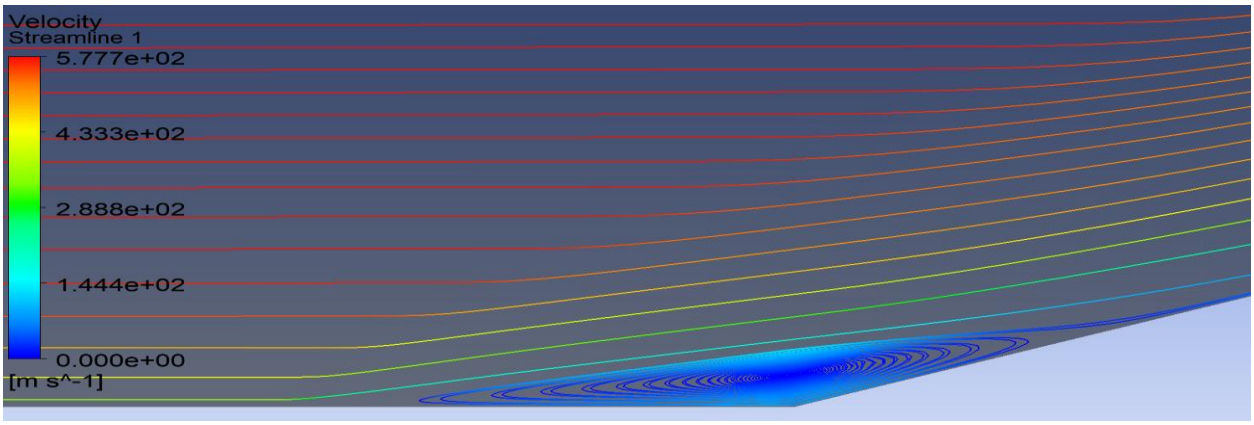

Figure 3.27 Streamlines in the recirculation region for Settles' case at Mach 2.85 for 20-degree corner angle computed using the WA model.

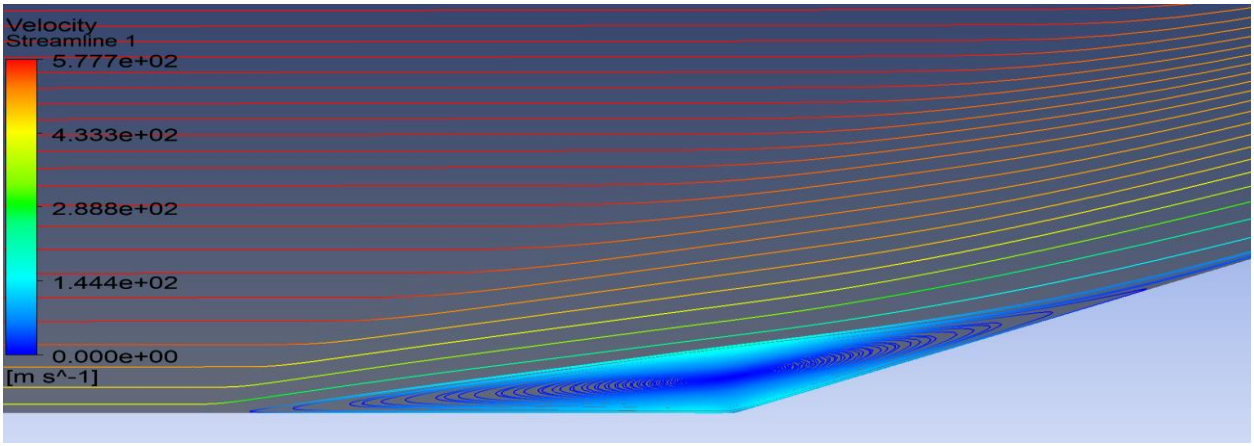

Figure 3.28 Streamlines in the recirculation region for Settles' case at Mach 2.85 for 24-degree corner angle computed using the SA model.

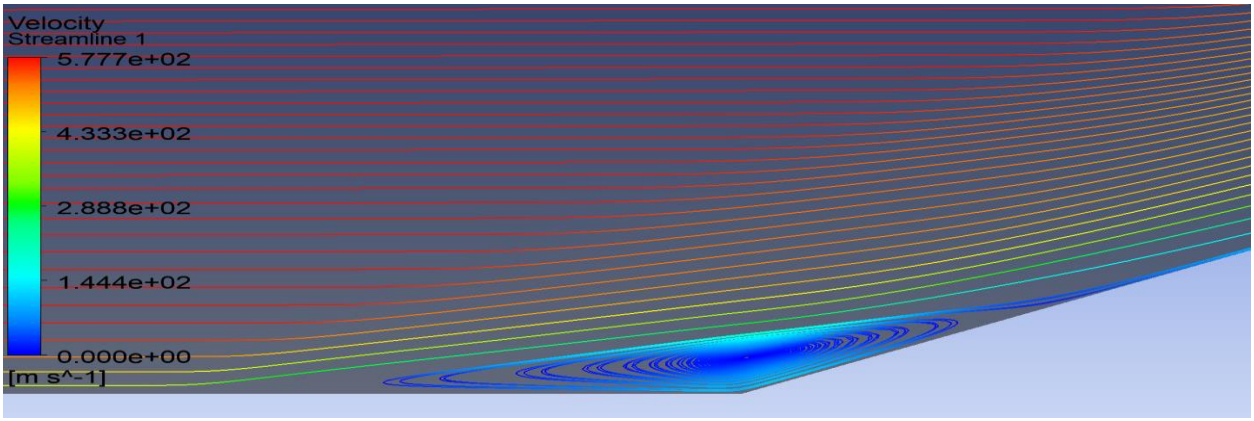

Figure 3.29 Streamlines in the recirculation region for Settles' case at Mach 2.85 for 24-degree corner angle computed using the SSST k-Omega model.

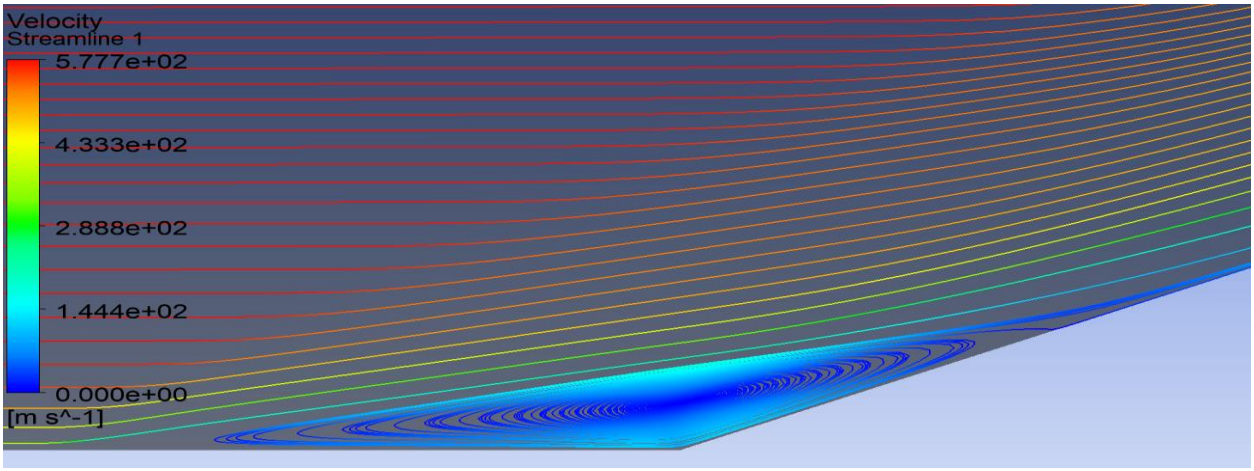

Figure 3.30 Streamlines in the recirculation region for Settles' case at Mach 2.85 for 24-degree corner angle computed using the WA model.

Table 3.1 compares the size of the computed recirculation region for various corner angles using different turbulence models. The size is given by the length in meters upstream from the compression corner when the recirculation region starts. This is judged by both the experimental data and the CFD results as the point where the static pressure is at least 10% higher than the freestream static pressure. A relative percentage error for each turbulence model's recirculation region is computed against the experimental data.

Table 3.1 Size of the recirculation region in meters with % error with respect to experimental values for Settles' case at M-2.85 for various corner angles using different turbulence models.

Angle	Exp	WA	% diff.	SA	% diff.	SST k-ω	% diff.
8							
16	-0.01167			-0.01171	0.338562	-0.03694	216.4837
20	-0.02144	-0.05953	177.7248	-0.04215	96.60397	-0.07534	251.4389
24	-0.04911	-0.121	146.3606	-9.22E-02	87.65985	-0.12403	152.5229

The major discrepancy between the experimental and computed sizes of the recirculation region is likely due to the way the boundary layer was defined and computed in Settles' case. The boundary layer velocity profile was guessed to be 2.3 cm high at the inflow boundary, which matched the measured boundary layer height in the experimental data. However, due to the

assumed distance of 1-meter between the inlet and the compression corner, the initial guess of the exponential velocity distribution in the boundary layer transformed over distance by the various turbulence models. In this process of transformation, the total size of the boundary layer grew considerably. Perhaps, this created the discrepancy in the sizes of the recirculation regions obtained with different turbulence models.

3.2 Holden's Mach 8.1 to 8.3 Flow Cases

3.2.1 Pressure Contours and Oblique Shock

Figures 3.31-3.42 show the pressure contours and oblique shock for Holden's case at Mach 8.1 for various corner angles using different turbulence models.

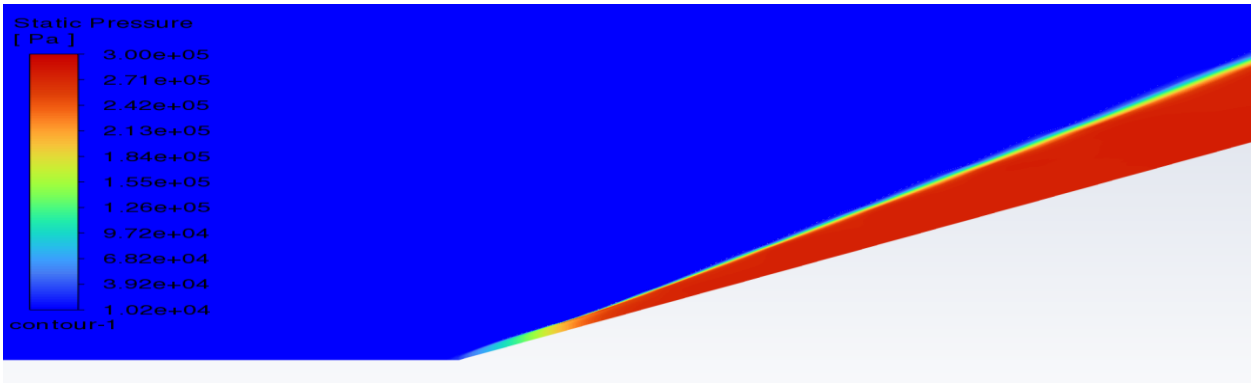

Figure 3.31 Pressure contours and oblique shock for Holden's case at Mach 8.2 for 27-degree corner angles using SA model.

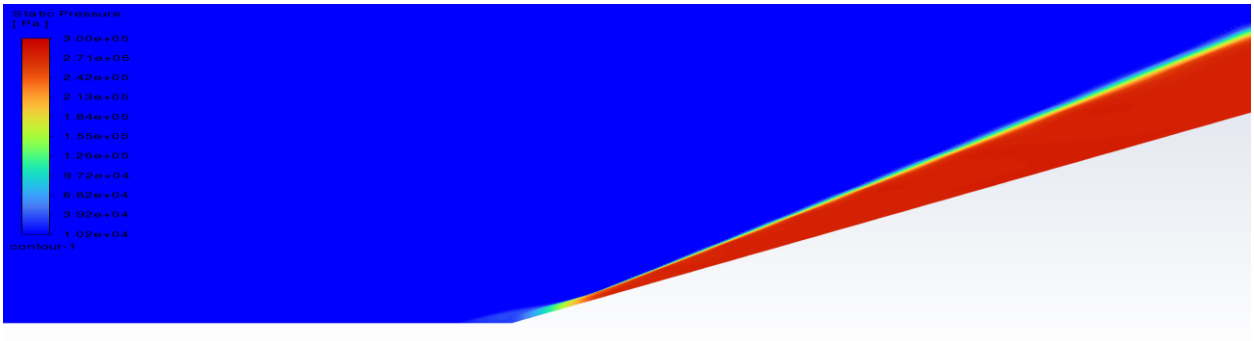

Figure 3.32 Pressure contours and oblique shock for Holden's case at Mach 8.2 for 27-degree corner angles using SST k-Omega model.

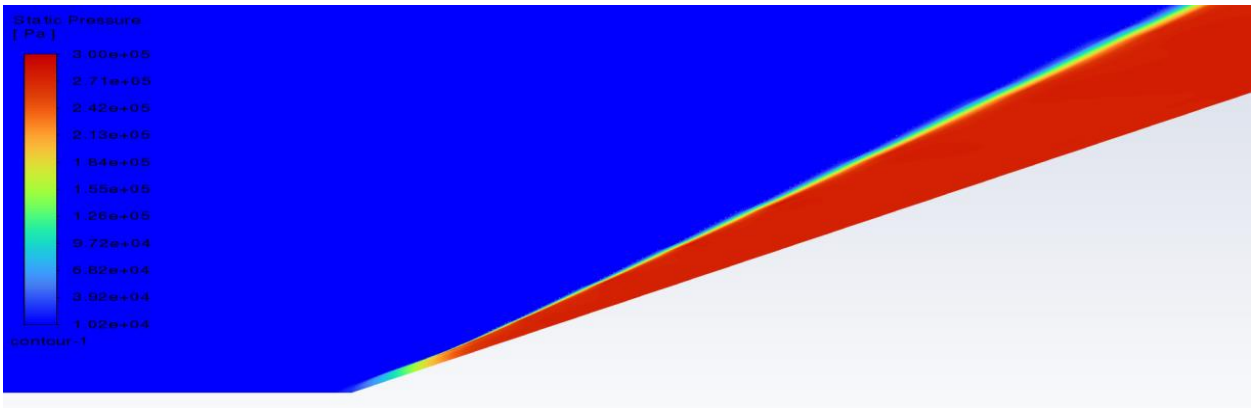

Figure 3.33 Pressure contours and oblique shock for Holden's case at Mach 8.2 for 27-degree corner angles using WA model.

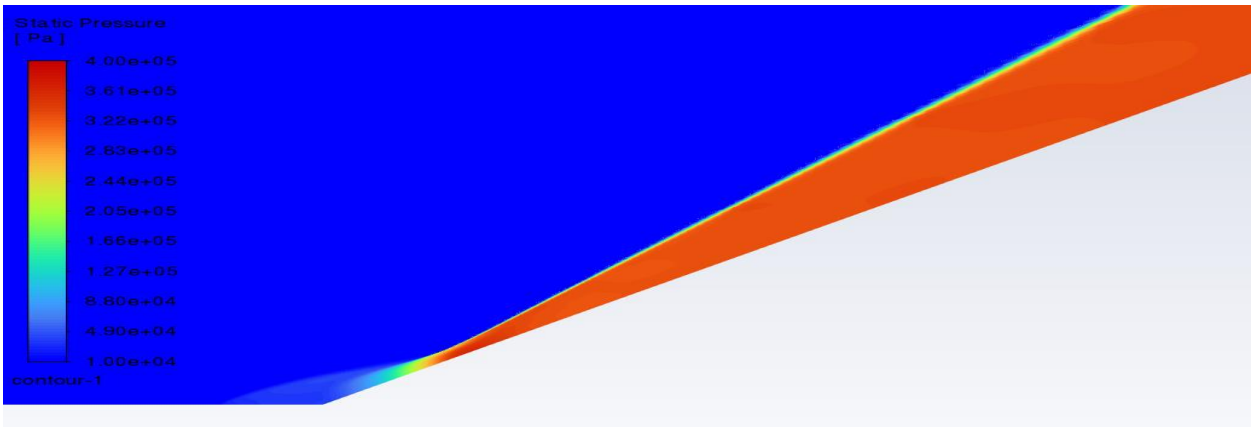

Figure 3.34 Pressure contours and oblique shock for Holden's case at Mach 8.3 for 30-degree corner angles using SA model.

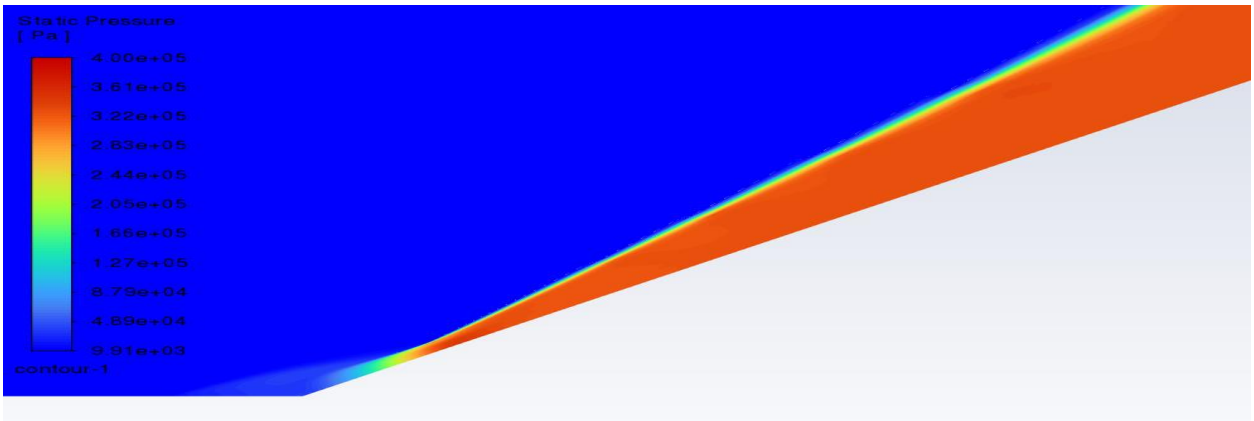

Figure 3.35 Pressure contours and oblique shock for Holden's case at Mach 8.3 for 30-degree corner angles using SST k-Omega model.

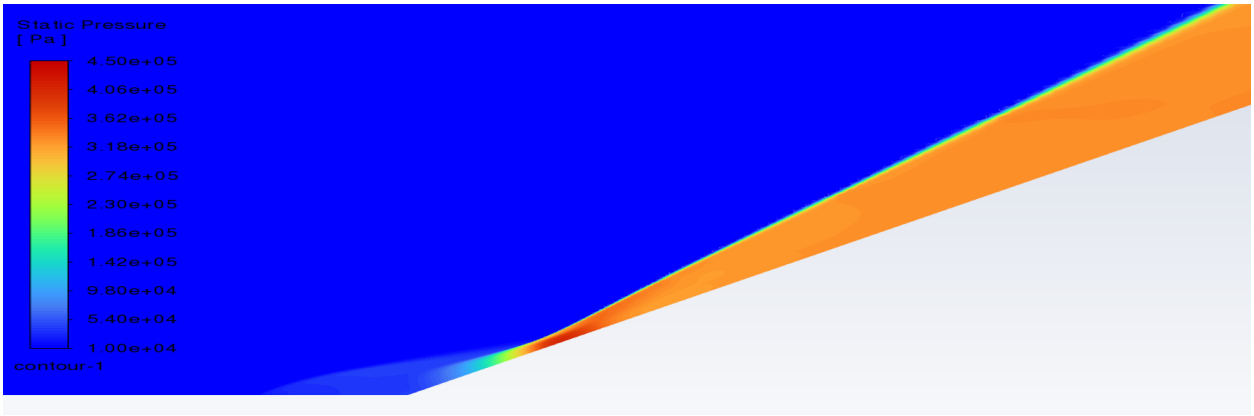

Figure 3.36 Pressure contours and oblique shock for Holden's case at Mach 8.3 for 30-degree corner angles using WA model.

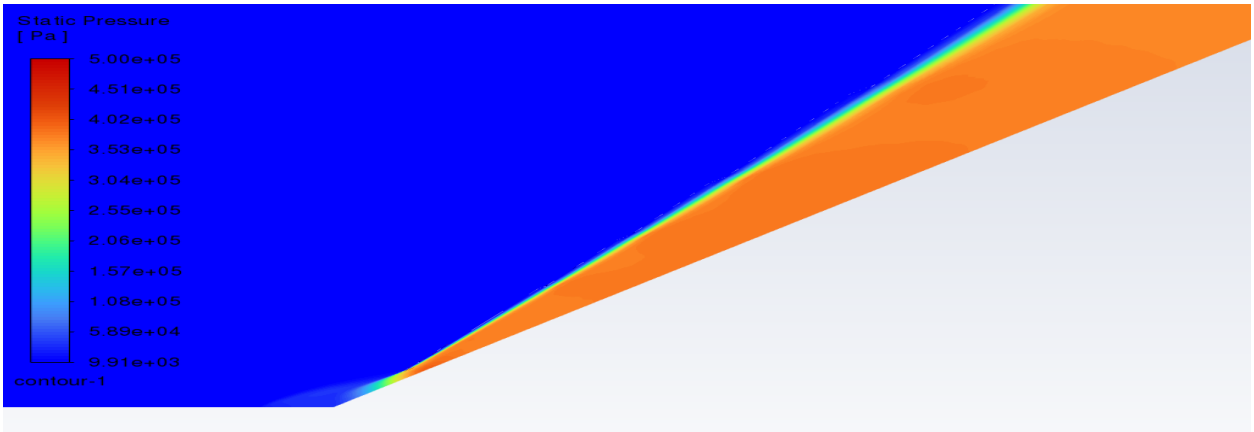

Figure 3.37 Pressure contours and oblique shock for Holden's case at Mach 8.1 for 33-degree corner angles using SA model.

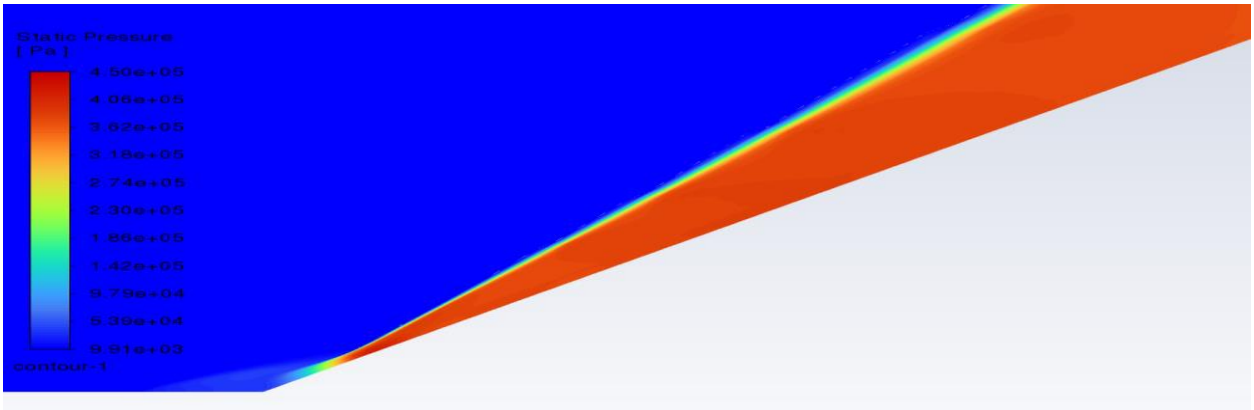

Figure 3.38 Pressure contours and oblique shock for Holden's case at Mach 8.1 for 33-degree corner angles using SST k-Omega model.

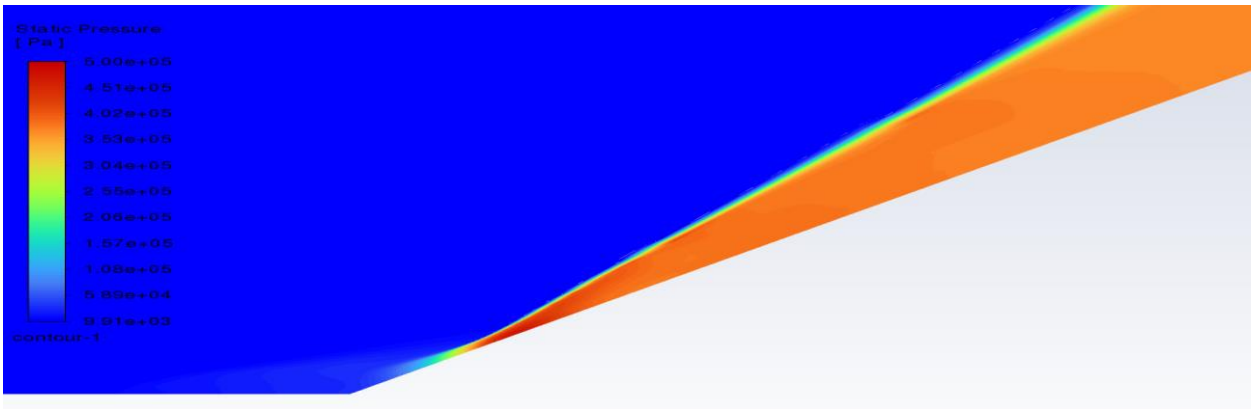

Figure 3.39 Pressure contours and oblique shock for Holden's case at Mach 8.1 for 33-degree corner angles using WA model.

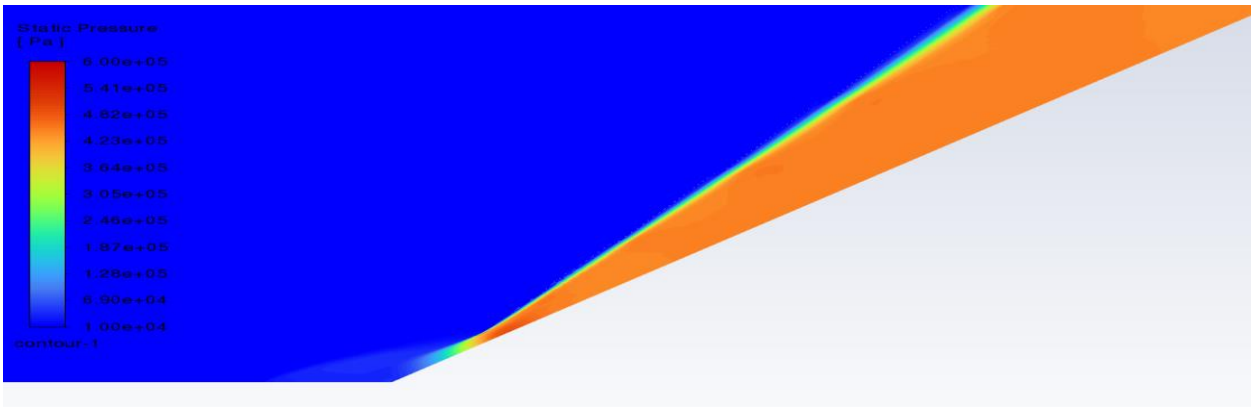

Figure 3.40 Pressure contours and oblique shock for Holden's case at Mach 8.2 for 36-degree corner angles using SA model.

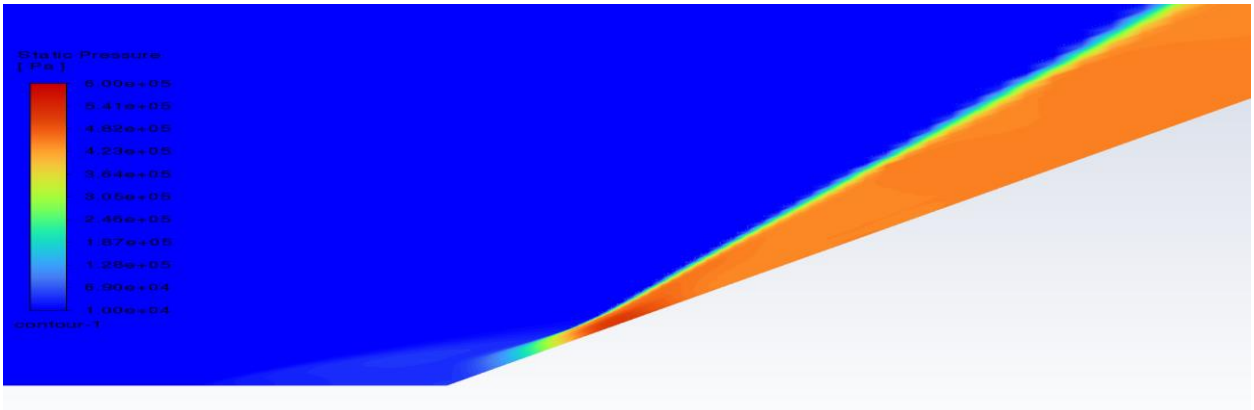

Figure 3.41 Pressure contours and oblique shock for Holden's case at Mach 8.2 for 36-degree corner angles using SST k-Omega model.

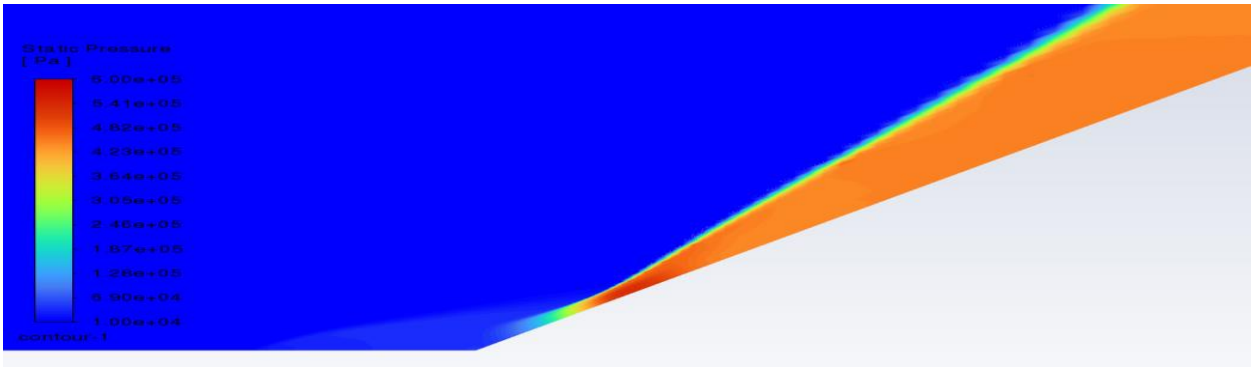

Figure 3.42 Pressure contours and oblique shock for Holden's case at Mach 8.2 for 36-degree corner angles using WA model.

3.2.2 Velocity Contours and Recirculating Region in the Corner

Figures 3.43-3.54 show the velocity contours and recirculation region for Holden's case at Mach 8.1 for various corner angles using different turbulence models.

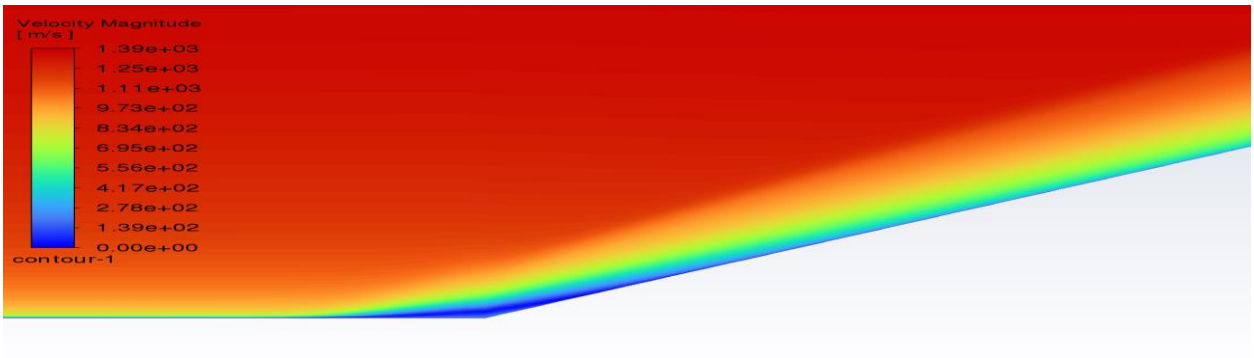

Figure 3.43 Velocity contours and recirculation region in the corner for Holden's case at Mach 8.2 for 27-degree corner angles using SA model.

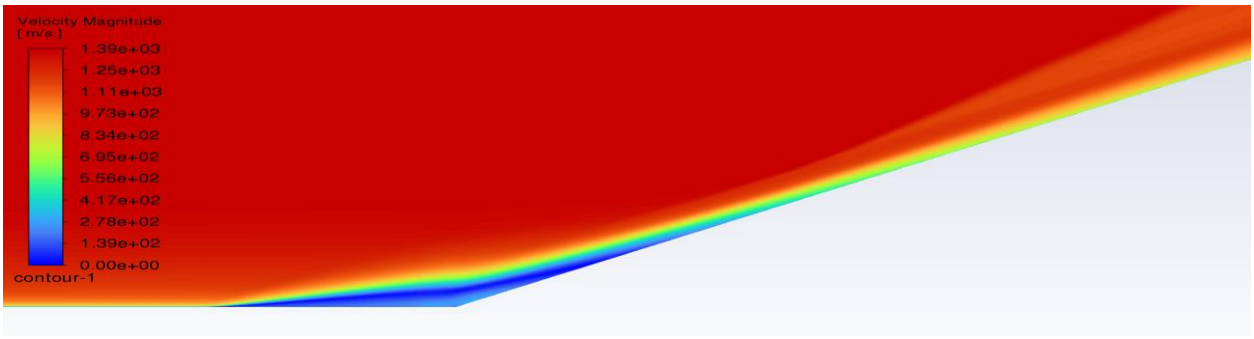

Figure 3.44 Velocity contours and recirculation region in the corner for Holden's case at Mach 8.2 for 27-degree corner angles using SST k-Omega model.

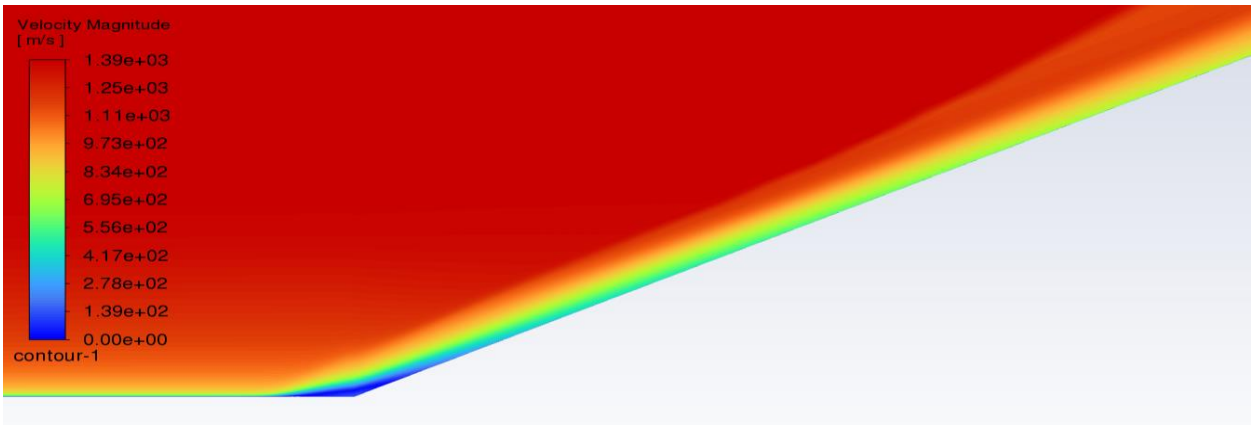

Figure 3.45 Velocity contours and recirculation region in the corner for Holden's case at Mach 8.2 for 27-degree corner angles using WA model.

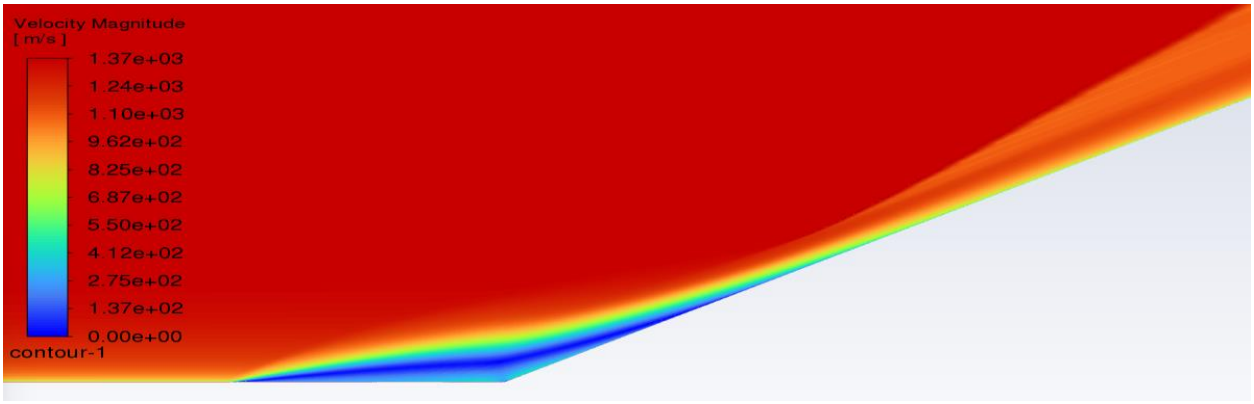

Figure 3.46 Velocity contours and recirculation region in the corner for Holden's case at Mach 8.3 for 30-degree corner angles using SA model.

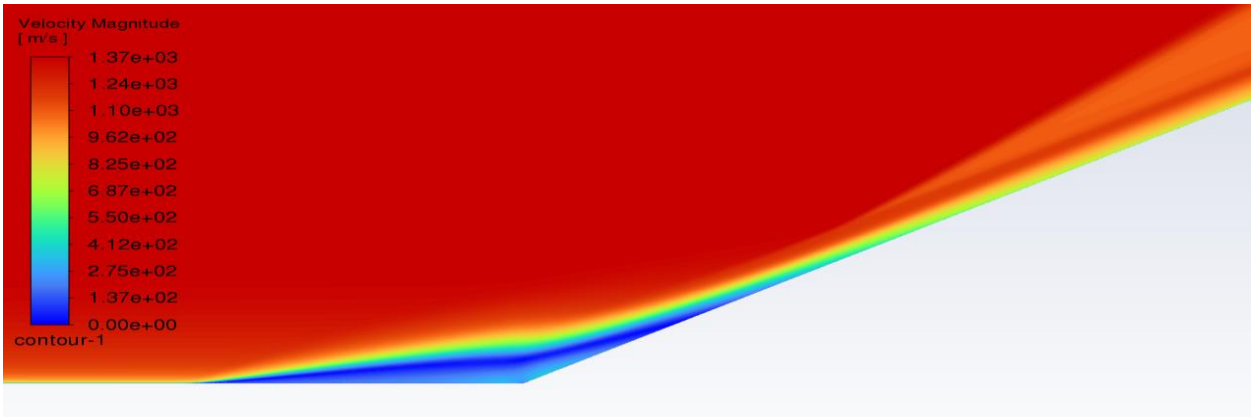

Figure 3.47 Velocity contours and recirculation region in the corner for Holden's case at Mach 8.3 for 30-degree corner angles using SST k-Omega model.

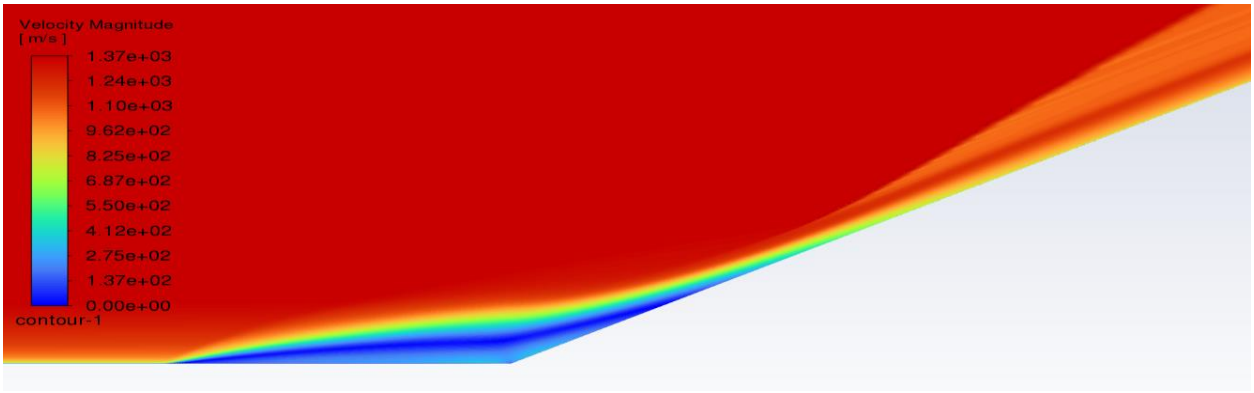

Figure 3.48 Velocity contours and recirculation region in the corner for Holden's case at Mach 8.3 for 30-degree corner angles using WA model.

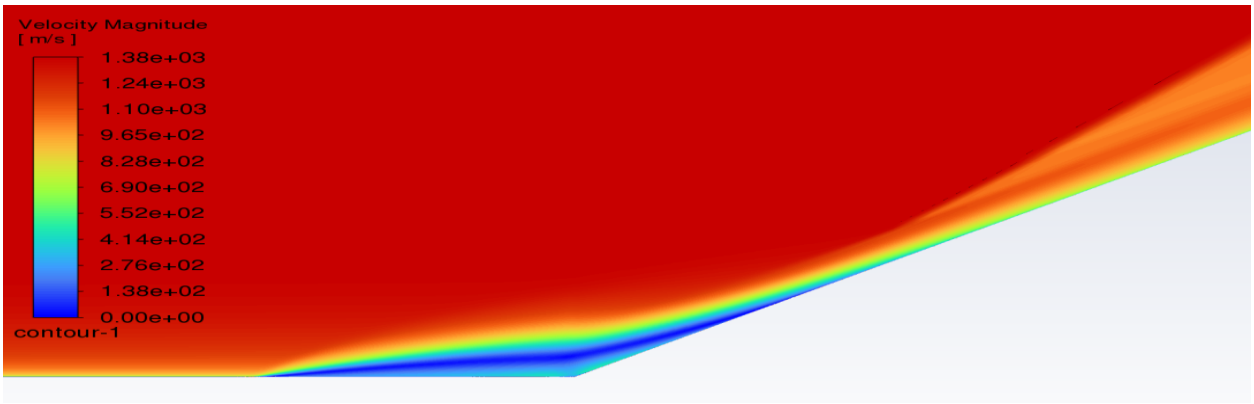

Figure 3.49 Velocity contours and recirculation region in the corner for Holden's case at Mach 8.1 for 33-degree corner angles using SA model.

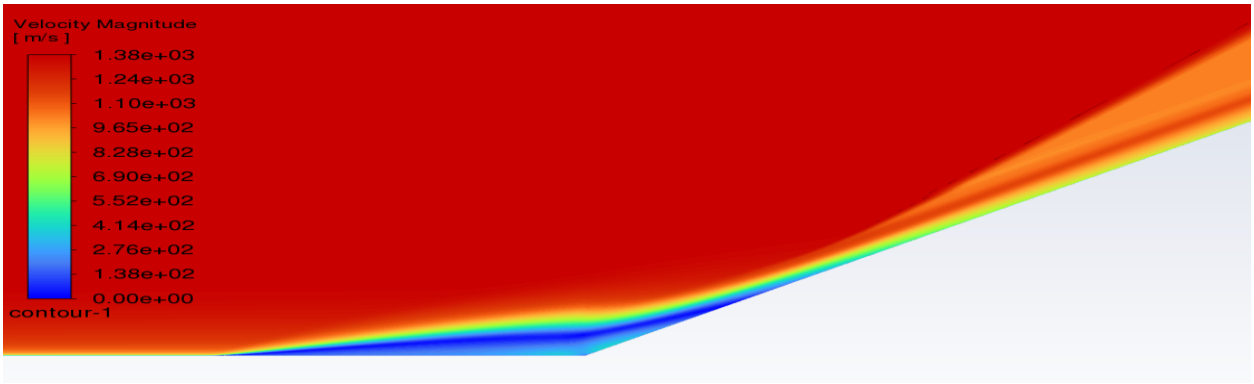

Figure 3.50 Velocity contours and recirculation region in the corner for Holden's case at Mach 8.1 for 33-degree corner angles using SST k-Omega model.

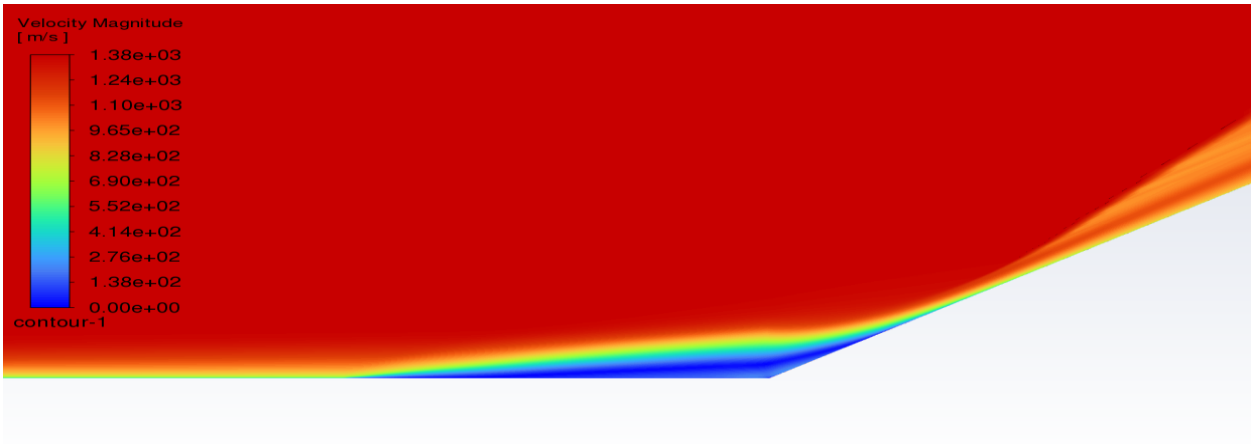

Figure 3.51 Velocity contours and recirculation region in the corner for Holden's case at Mach 8.1 for 33-degree corner angles using WA model.

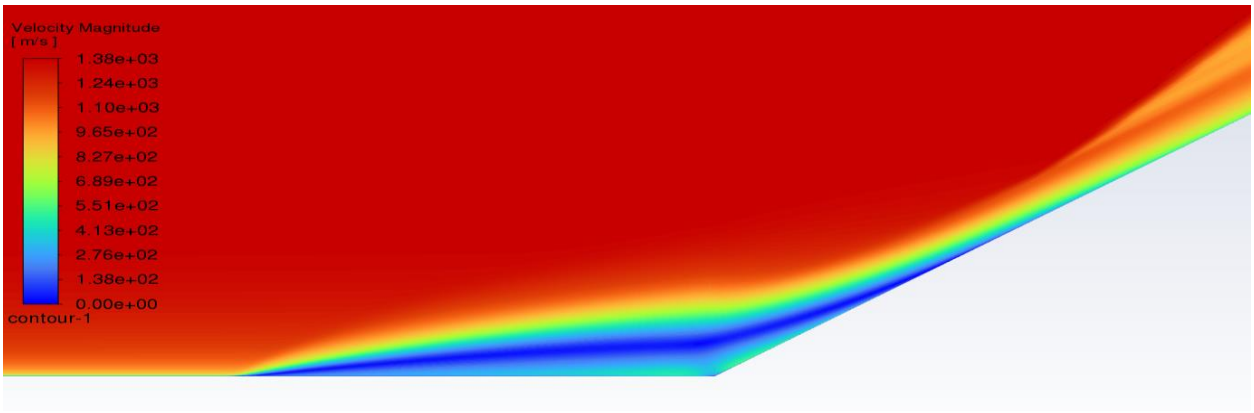

Figure 3.52 Velocity contours and recirculation region in the corner for Holden's case at Mach 8.2 for 36-degree corner angles using SA model.

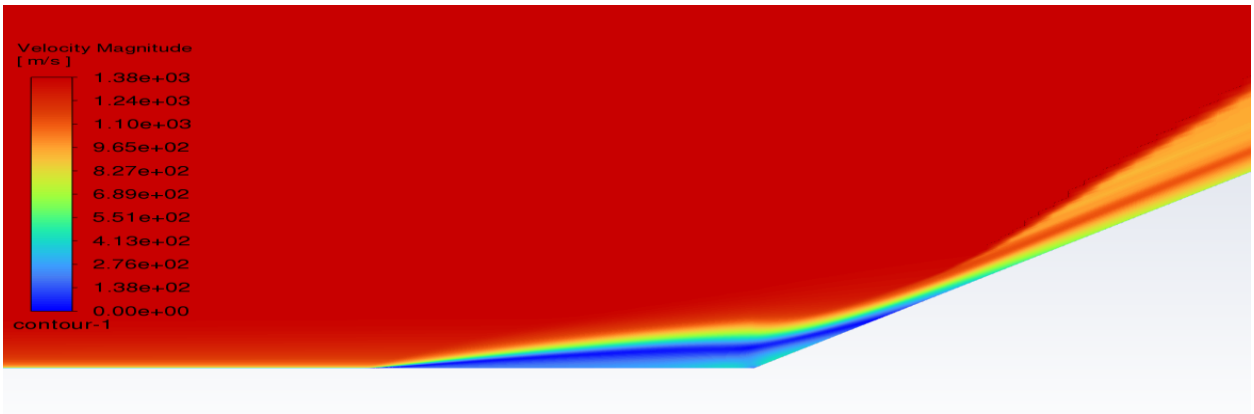

Figure 3.53 Velocity contours and recirculation region in the corner for Holden's case at Mach 8.2 for 36-degree corner angles using SST k-Omega model.

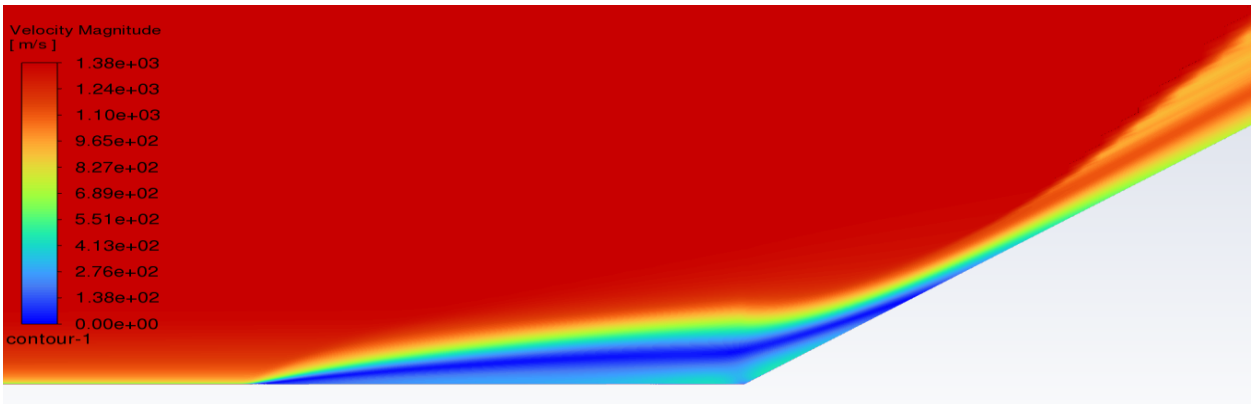

Figure 3.54 Velocity contours and recirculation region in the corner for Holden's case at Mach 8.2 for 36-degree corner angles using WA model.

3.2.3 Surface Static Pressure in the Corner

Figures 3.50 – 3. 53 show the comparison of experimental surface static pressure distribution for Holden's case at Mach ~ 8 for various corner angle with computations using the three-turbulence models.

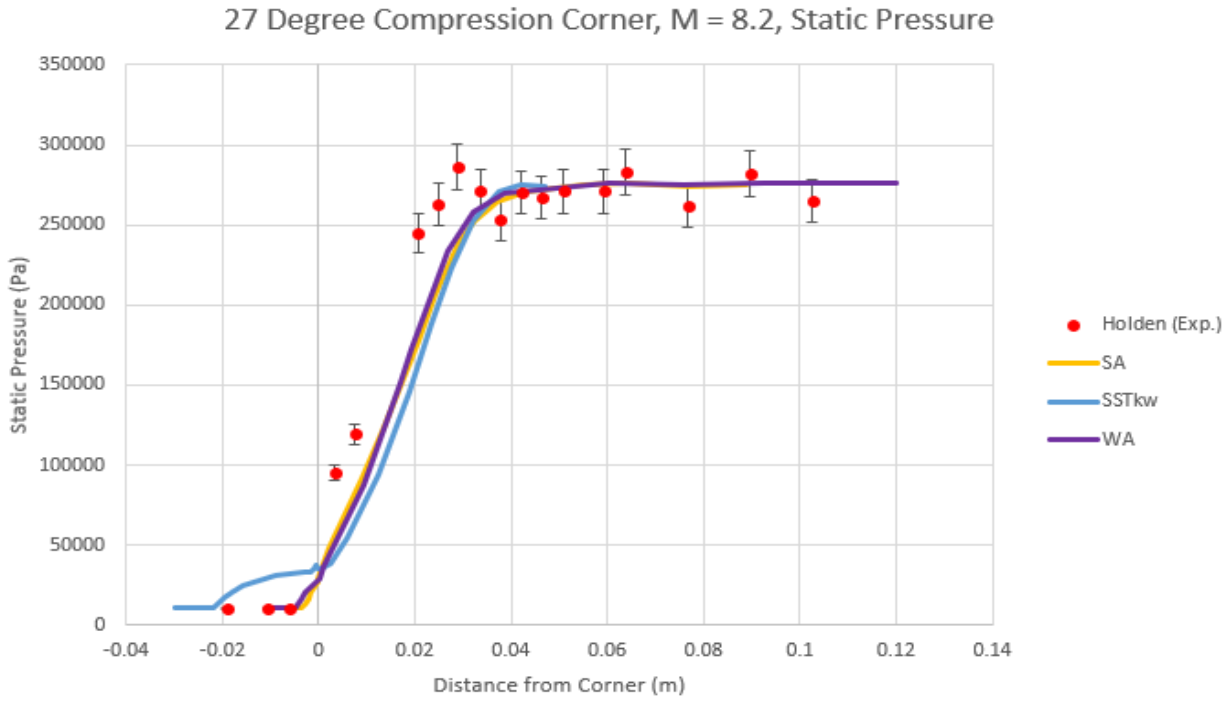

Figure 3.55 Comparison of experimental surface static pressure distribution for Holden's case at Mach 8.2 for 27-degree corner angle with computations using the three-turbulence models.

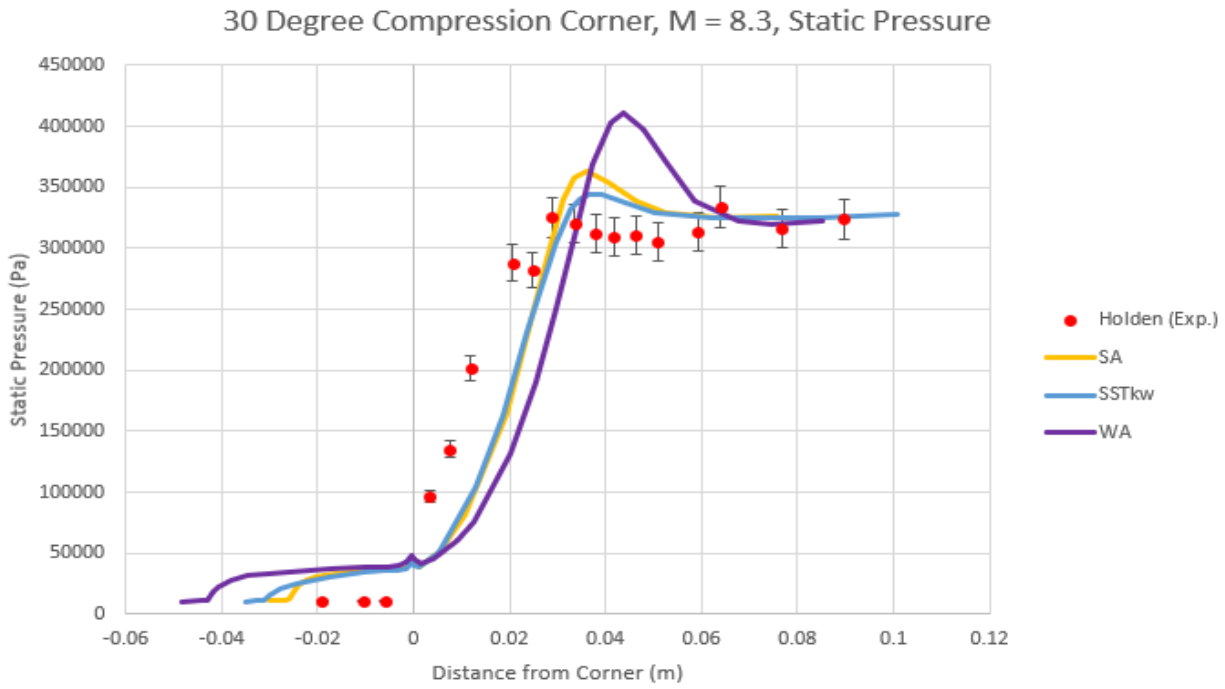

Figure 3.56 Comparison of experimental surface static pressure distribution for Holden's case at Mach 8.3 for 30-degree corner angle with computations using the three-turbulence models.

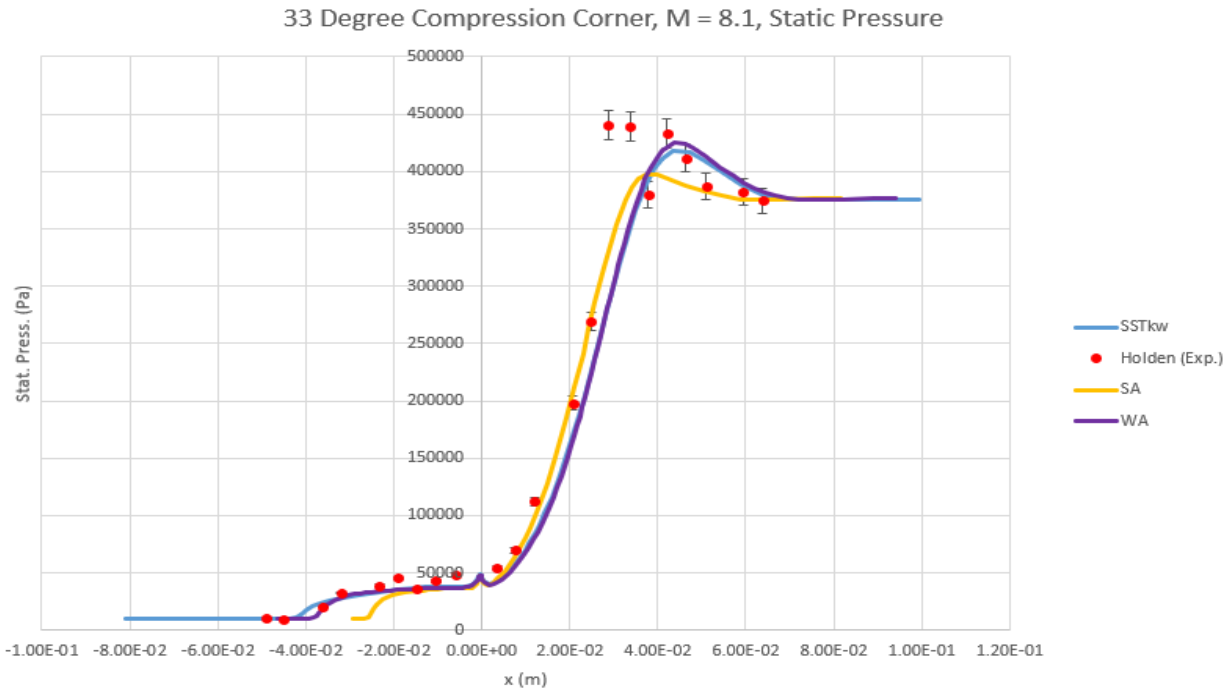

Figure 3.57 Comparison of experimental surface static pressure distribution for Holden's case at Mach 8.1 for 33-degree corner angle with computations using the three-turbulence models.

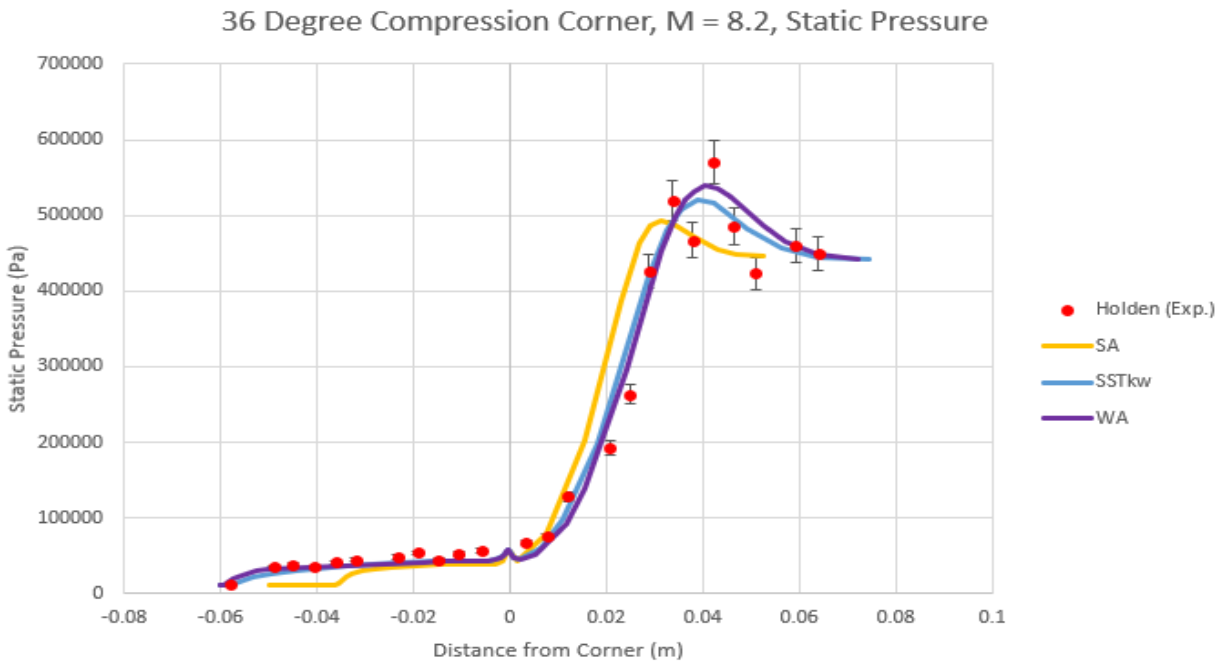

Figure 3.58 Comparison of experimental surface static pressure distribution for Holden's case at Mach 8.2 for 36-degree corner angle with computations using the three-turbulence models.

3.2.4 Recirculation Region

Holden's Mach 8.1, 33-degree corner angle case includes a significant recirculation region in both the experimental data and in the computations using the three turbulence models. Figures 3.54 - 3.59 show the recirculation region at various Mach numbers and corner angles using the three turbulence models.

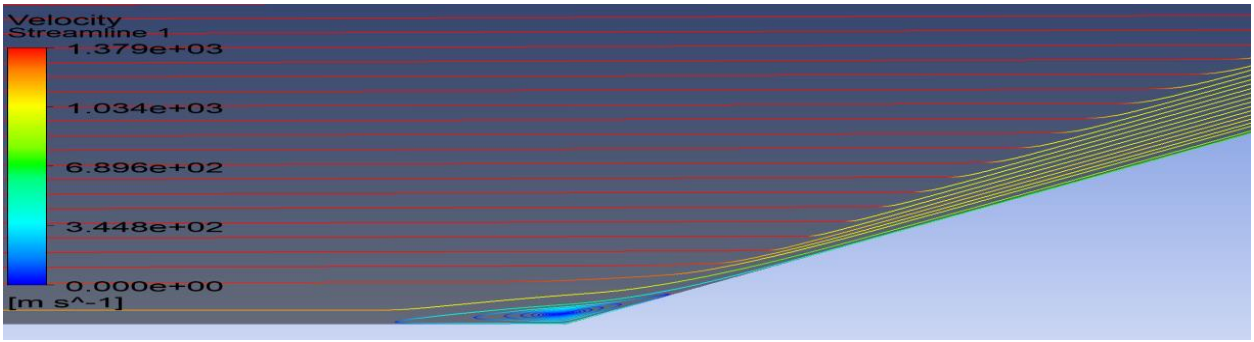

Figure 3.59 Streamlines in the corner showing recirculation region for Holden's case at Mach 8.3 for 33-degree corner angle using the SA model.

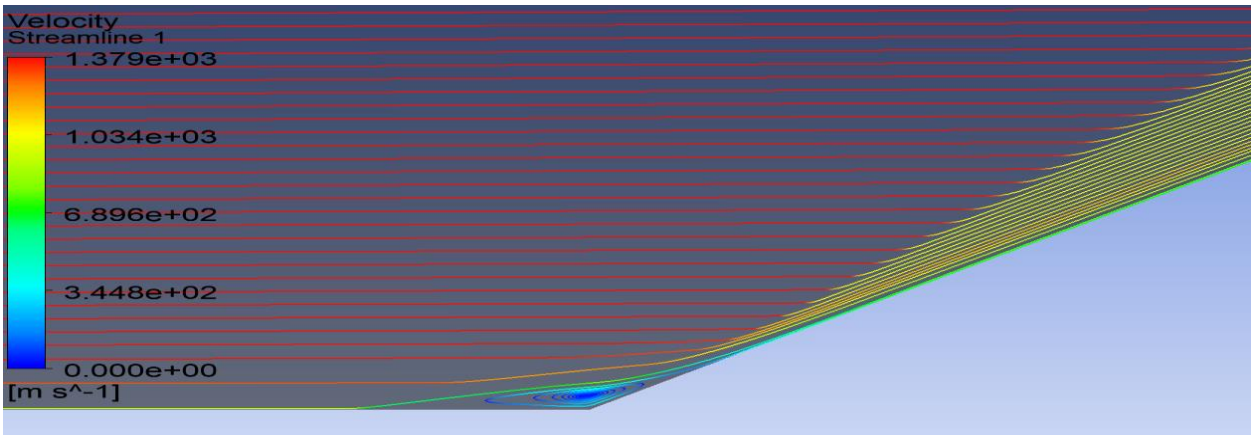

Figure 3.60 Streamlines in the corner showing recirculation region for Holden's case at Mach 8.3 for 33-degree corner angle using the SST k-Omega model.

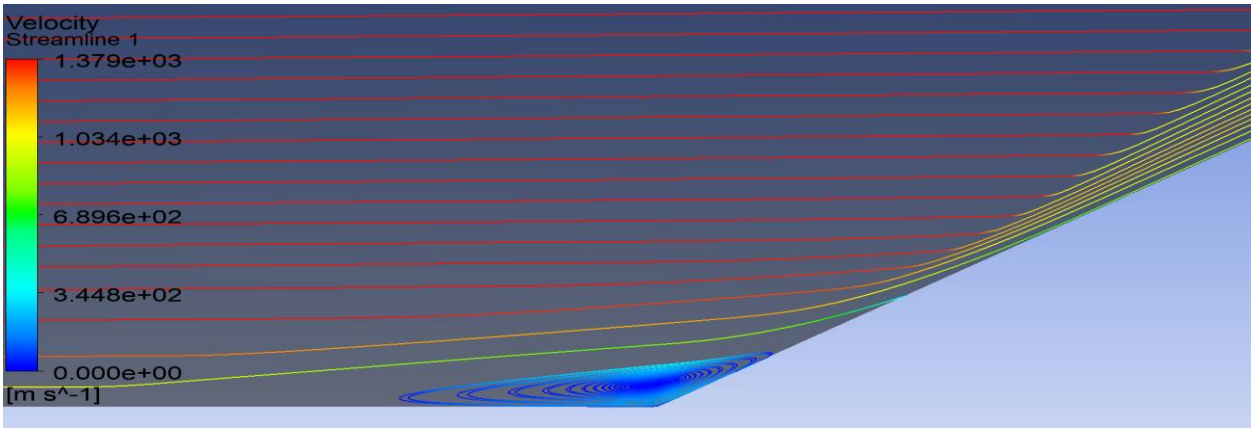

Figure 3.61 Streamlines in the corner showing recirculation region for Holden's case at Mach 8.3 for 33-degree corner angle using the WA model.

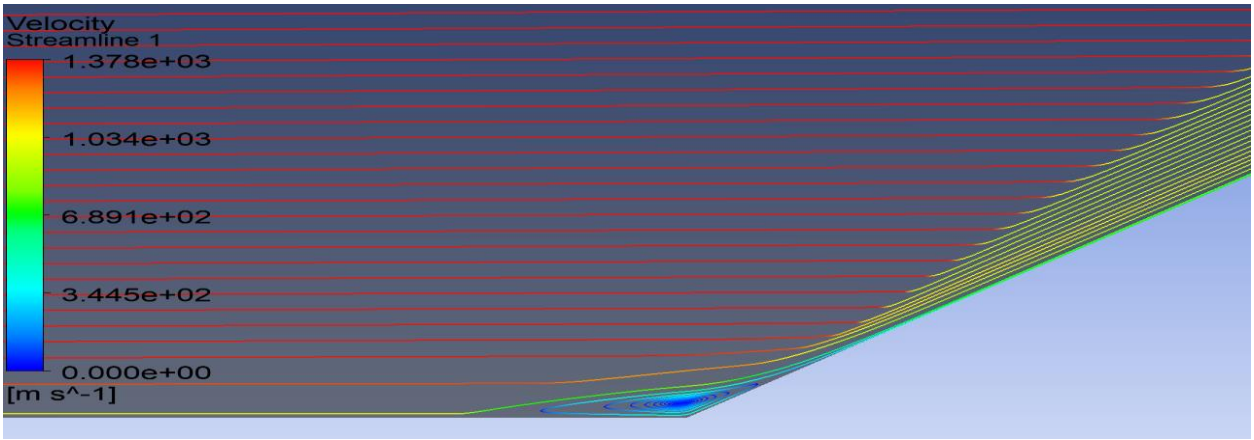

Figure 3.62 Streamlines in the corner showing recirculation region for Holden's case at Mach 8.2 for 36-degree corner angle using the SA model.

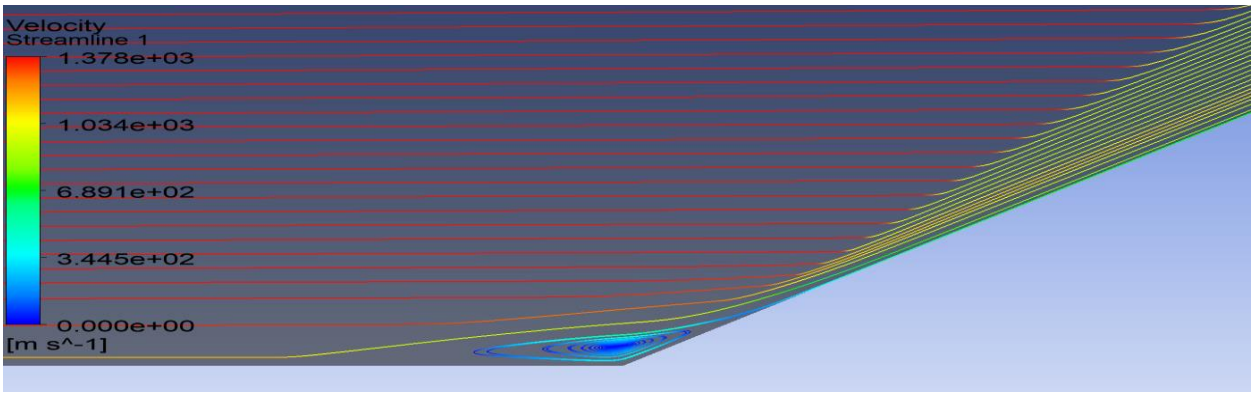

Figure 3.63 Streamlines in the corner showing recirculation region for Holden's case at Mach 8.2 for 36-degree corner angle using the SST k-Omega model.

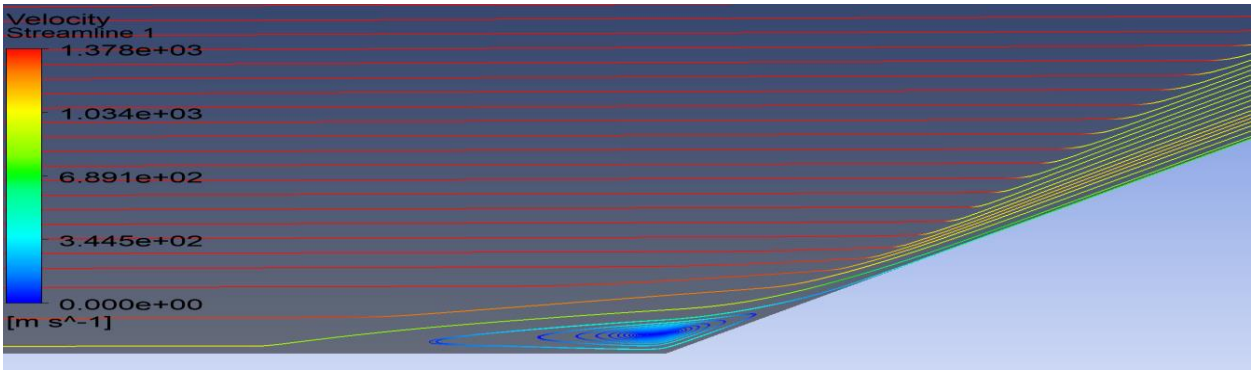

Figure 3.64 Streamlines in the corner showing recirculation region for Holden's case At Mach 8.2 for 36-degree corner angle using the WA model.

Table 3.2 shows the distance in meters from the compression corner at which the recirculation regions starts, The beginning of the recirculation region is determined by the first point where the static pressure reaches 10% or more above the freestream static pressure. The percentage difference between the computed results using various turbulence models and the experimental result is also shown in Table 3.2.

Table 3.2 Size of the recirculation region in meters with % error with respect to experimental values for Holden's case at M~8 for various corner angles using different turbulence models.

Angle	Exp	WA (m)	% diff.	SA (m)	% diff.	SST kω (m)	% diff.
33	-0.03607	-0.03744	3.802808	-0.0258	-28.41	-0.04219	16.97888
36	-0.05791	-0.05721	-1.21055	-0.0354	-38.87	-0.05696	-1.64525

.

3.3 Holden's Mach 11.3 Flow Cases

3.3.1 Pressure Contours and Shock Wave

Figures 3.60-3.62 show the pressure contours and oblique shock for Holden's case at Mach 11.3 for various corner angles using different turbulence models.

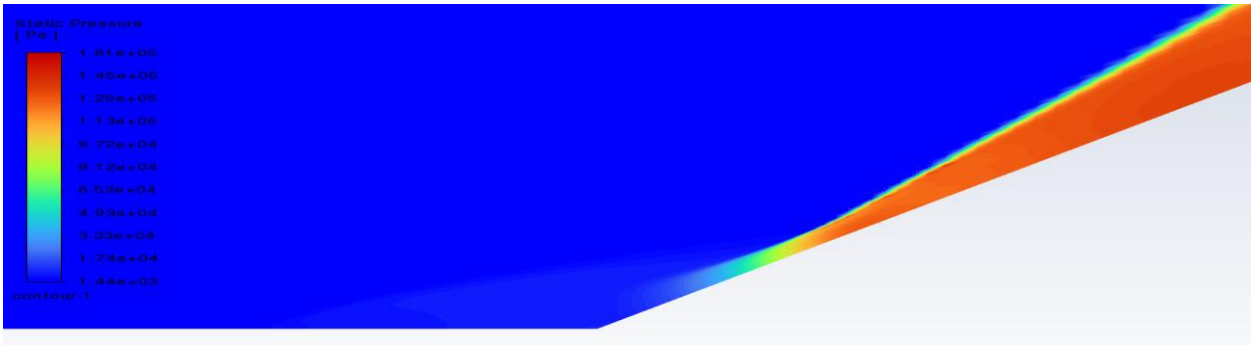

Figure 3.65 Pressure contours and oblique shock for Holden's case at Mach 11.3 for 36-degree corner angles using SA model.

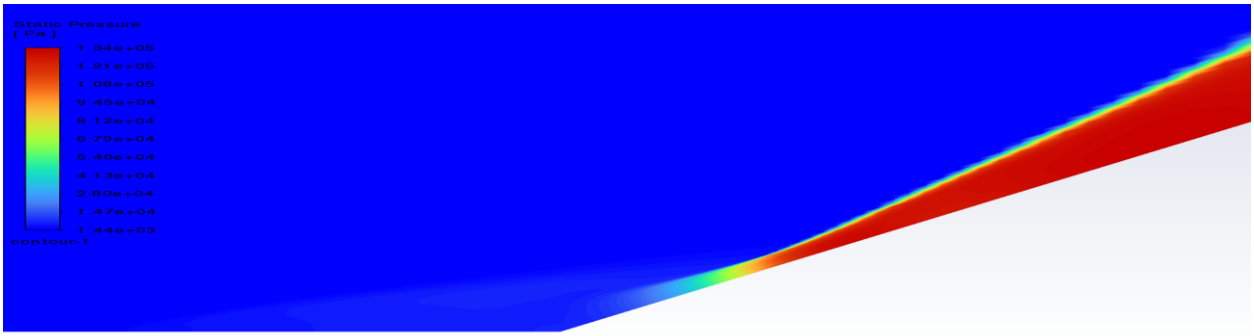

Figure 3.66 Pressure contours and oblique shock for Holden's case at Mach 11.3 for 36-degree corner angles using SST k-Omega model.

Figure 3.67 Pressure contours and oblique shock for Holden's case at Mach 11.3 for 36-degree corner angles using WA model.

3.3.2 Velocity Contours and Recirculation Region

Figures 3.63-3.65 show the velocity contours and recirculation region for Holden's case at Mach 11.3 for various corner angles using different turbulence models.

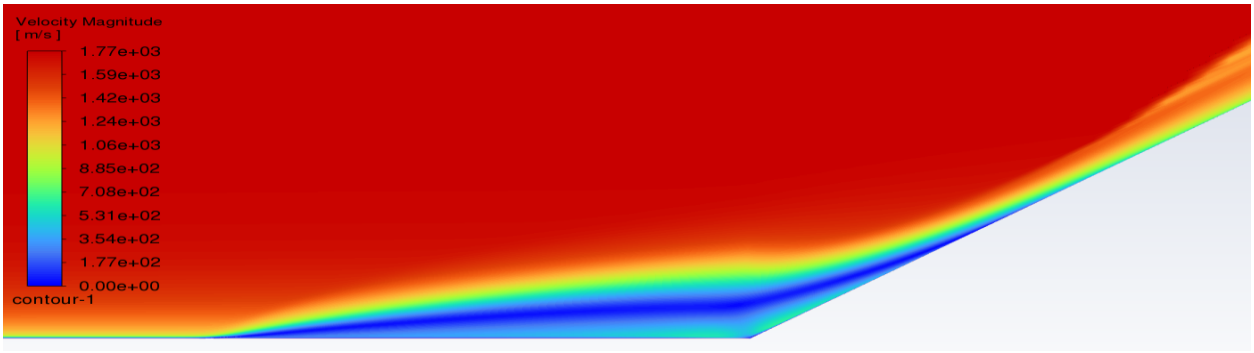

Figure 3.68 Velocity contours and recirculation region in the corner for Holden's case at Mach 11.3 for 36-degree corner angles using SA model.

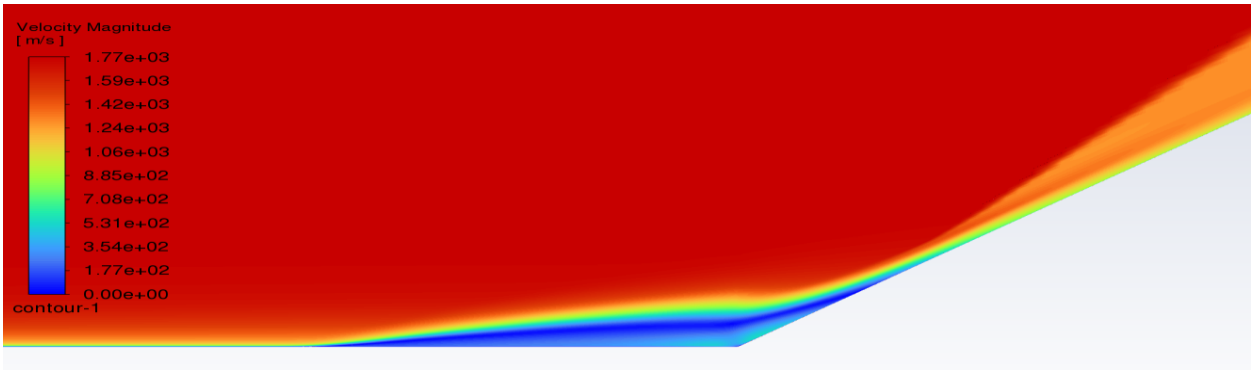

Figure 3.69 Velocity contours and recirculation region in the corner for Holden's case at Mach 11.3 for 36-degree corner angles using SST k-Omega model.

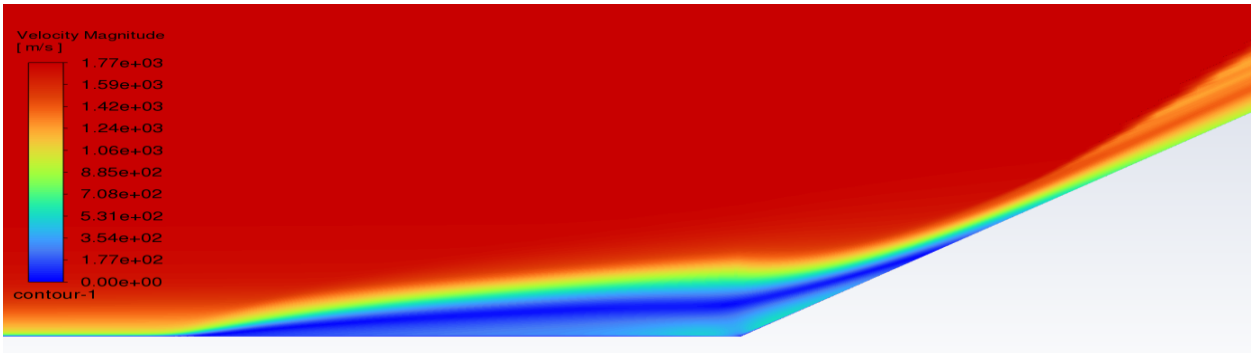

Figure 3.70 Velocity contours and recirculation region in the corner for Holden's case at Mach 11.3 for 36-degree corner angles using WA model.

3.3.2 Surface Static Pressure in the Corner

Figures 3.66 shows the comparison of experimental surface static pressure distribution for Holden's case at Mach 11.3 at 36-degree corner angle with computations using the three-turbulence models.

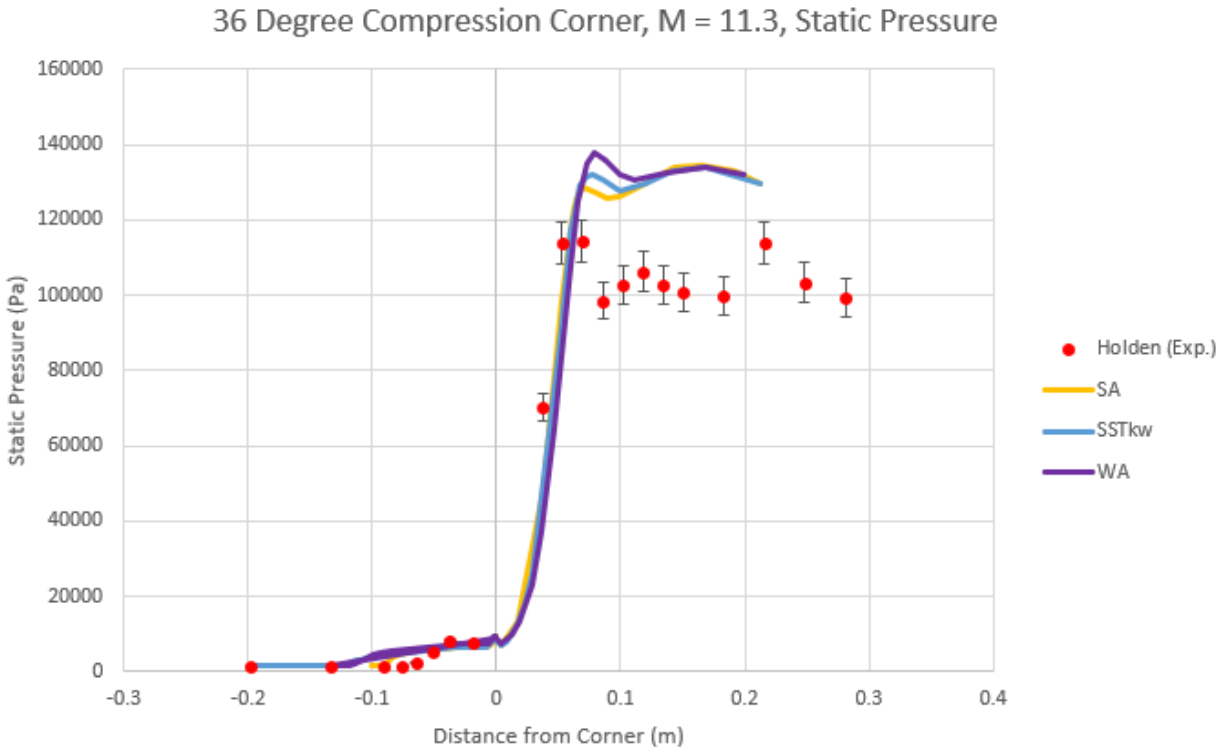

Figure 3.71 comparison of experimental surface static pressure distribution for Holden's case at Mach 11.3 for 36-degree corner angle with computations using the three-turbulence models.

3.3.3 Recirculation Region

Holden's Mach 11.3, 36-degree corner angle case includes a significant recirculation region in both the experimental data and in the computations using the three turbulence models. Figures 3.67 - 3.69 show the recirculation region using the three turbulence models.

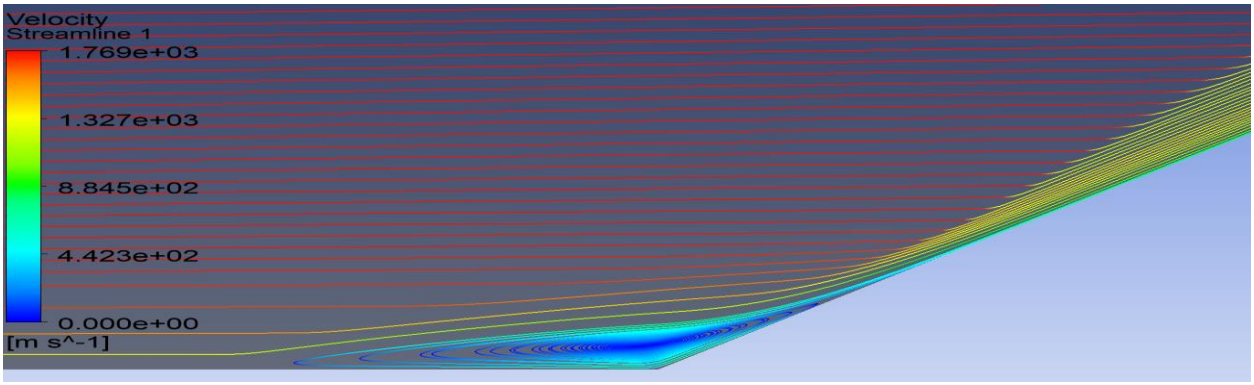

Figure 3.72 Streamline and recirculation region in the corner for Holden's case at Mach 11.3 for 36-degree corner angles using SA model.

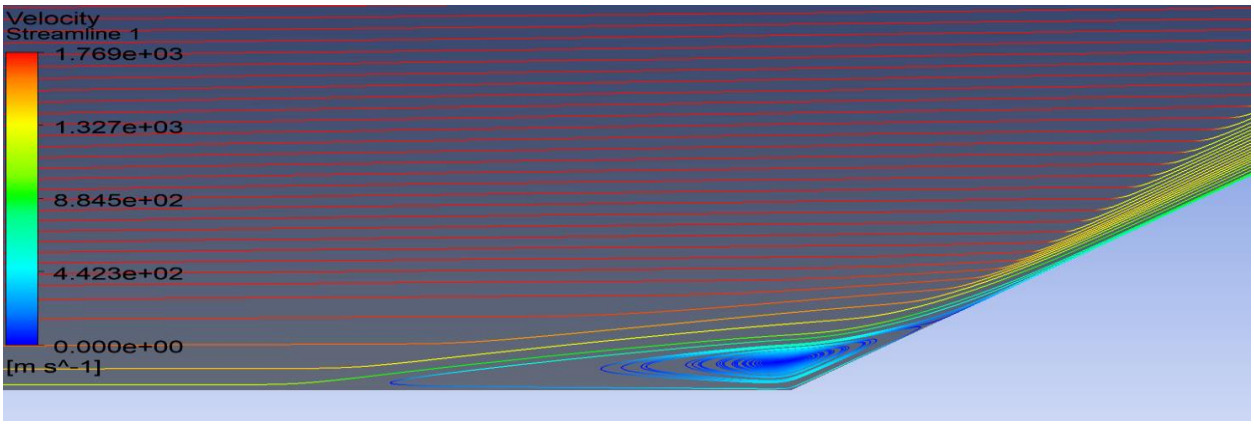

Figure 3.73 Streamline and recirculation region in the corner for Holden's case at Mach 11.3 for 36-degree corner angles using SST k-Omega model.

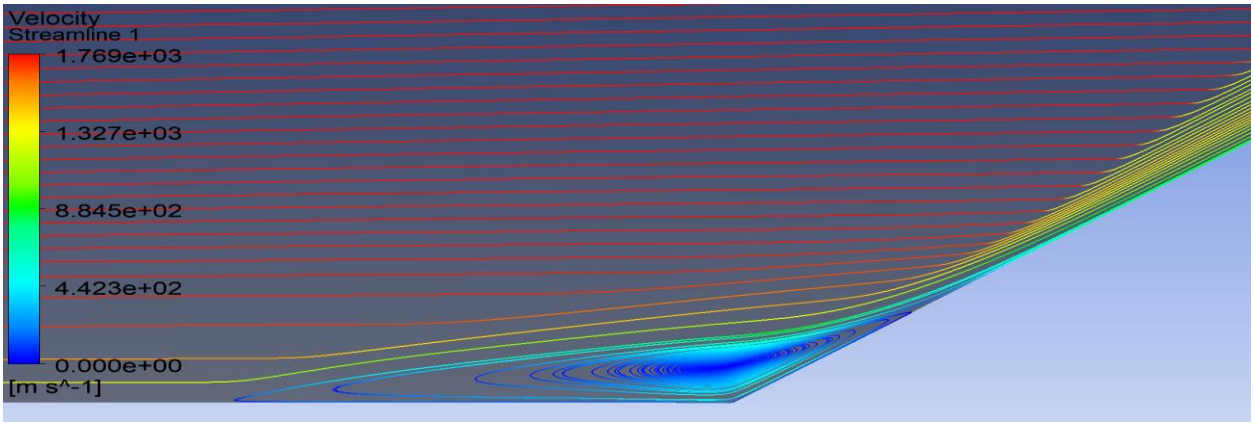

Figure 3.74 Streamline and recirculation region in the corner for Holden's case at Mach 11.3 for 36-degree corner angles using WA model.

Chapter 4: Conclusions and Future Work

4.1 Conclusions

For supersonic flow in a compression corner, in the Settles' experimental cases at Mach 2.85, as implemented, computations with all the three turbulence models have difficulty in matching with the data and in predicting the features of the shock/ boundary layer interactions. The recirculation regions for the corner angles of 20 and 24 degree are predicted to be significantly larger than in the experiment. It is surmised that this is perhaps due to the approximate implementation of the experimental value of the upstream turbulent boundary layer thickness as the inlet velocity boundary condition in the CFD simulations. The boundary layer profile at the inlet of the computational domain was defined by an exponential velocity profile with boundary layer thickness of 2.3 cm, which was close to the thickness of the experimental boundary layer. However, over a distance of one meter, the CFD solver transformed the initial guess of the boundary layer into a more fuller boundary layer profile when the flow reached the compression corner. As a result, the boundary layer thickness increased by a significant amount in the simulations. Therefore, it is not entirely due to the empiricism in the turbulence models that there was discrepancy in the size of experimental and computed recirculation region but can also be attributed to the difference in the experimental and computed boundary layer thickness at the compression corner.

In the simulation of Holden's Mach 8 experimental hypersonic compression corner flow cases, it is found that the SST k-Omega model and WA model perform generally similarly to each other as expected. For the 33-degree corner angle, WA model showed the best performance with a 3.8% difference between the simulated and experimental recirculation region size, whereas the SA and SST k-Omega model had 28.4% and 17.0% difference respectively.For the 36-degree

corner angle, the WA model again showed the best performance with only 1.2% difference in the size of the recirculation region compared to experiment, while the SA and the SST k-Omega had 38.9% and 1.6% difference respectively.

The SA model consistently underpredicted the size of the recirculation region in these higher Mach number Holden's experimental cases. The WA model, on the other hand, performed well in these high Mach number cases. It slightly outperformed the SST k-Omega model in the 33- and 36- degree corner angle cases, and interestingly it greatly outperformed the SST k-Omega model in the 27-degree corner angle case. At 27-degree corner angle, the experimental data showed no recirculation region in the corner. Both the SA model and the WA model matched the experimental result predicting that no recirculation region exists; however the SST k-Omega model predicts a major recirculation region, which is certainly an error.

Similar to the Settles' experimental Mach 2.85 cases, in case of Holden's experimental Mach 11 case, all turbulence models predicted a larger recirculation region than was found in the experimental data. However, in contrast to the Settles's cases, in this case of Holden the boundary layer was able to develop from the uniform velocity profile at the inlet. In addition, at very high Mach numbers and low densities, the flow can become rarefied and chemical dissociation can begin to occur. In the literature, these high Mach number phenomena have been addressed by changing the specific heat of the working fluid to be non-constant, following the NASA's 9-part polynomial that is built into Fluent, and the viscosity of the air defined by Sutherland's law.

Overall, the WA model performed favorably compared to the SA and SST k-Omega turbulence models. It provided results similar to the SST k-Omega model despite being a one-equation model whereas SST k-Omega is a two-equation model. It often gave more accurate

predictions in the shock/boundary layer interaction region compared to the SA model, especially for the Mach 8 cases.

As hypersonic aerodynamics becomes a more active field in the next few years, it is expected that the hypersonic CFD will play a major role in the design and development of new hypersonic vehicles. Given this relatively new emphasis in the field of aerodynamics of hypersonic flows, it is necessary that the appropriate and accurate simulation tools are available to the designers. The results of this thesis suggest that the WA turbulence model may be a good choice for use in hypersonic CFD based on the RANS equations, since it has demonstrated good accuracy at high Mach shock/boundary layer interaction flows.

4.2 Future Work

The work done in this thesis could be expanded and investigated more deeply by further work and research. The compression corner is one of the best flow geometries for investigating the shock/boundary layer interactions in supersonic and hypersonic flow, and there are quite a number of experimental wind tunnel data sets and shock tube results available for this geometry. The conclusions found regarding the accuracy of the turbulence models could be tested and reinforced by testing more cases of supersonic and hypersonic compression corner flows at a wide range of Mach numbers. Furthermore, there exist experimental cases of hypersonic compression corner flows that do not use air as a working fluid. The accuracy/performance of the turbulence models in a non-air working fluid would be especially of interest for their application in interplanetary spaceflight. Since different planets and their moons can have vastly different atmospheric compositions, turbulence models used in such simulations should be improved if needed to obtain accurate results independent of the working fluid.

Additionally, there are other geometries that can be used to test a turbulence model's accuracy/performance in capturing more complex shock/shock and shock/boundary layer interactions in the supersonic and hypersonic flows. One such geometry is the axisymmetric flare, which is essentially an axisymmetric variation of the compression corner. Due to the similarity of these geometries, a researcher could adapt a mesh for a 2D compression corner into an axisymmetric flare case without much difficulty and study the performance of the turbulence models at high Mach number for the axisymmetric flare. Another fundamental supersonic flow phenomenon occurs when a shock impinges on a flat plate and goes through shock/boundary layer interaction with a small region of separation. This phenomenon can be observed in the supersonic/hypersonic vehicle intakes. The development of accurate turbulence models for hypersonic cold and hot wall flows both in adverse and favorable pressure gradients currently is a very important and fruitful area of research.

References

[1] B. V. Hove and O. Karatekin, “Atmospheric Reconstruction with Stagnation Pressure Flight Data from Mars Science Laboratory,” AIAA Journal, vol. 54, no. 3, 2017.

[2] C. Y. Tang, “An Introduction to DPLR,” NASA Ames Research Center Thermal and Fluids Analysis Workshop, 2016.

[3] F. M. Cheatwood, D. Bose, C. D. Karlgaard, C. A. Kuhl, J. A. Santos, and M. J. Wright, “Mars Science Laboratory (MSL) Entry, Descent, and Landing Instrumentation (MEDLI): Complete Flight Data Set,” NASA Ames Research Center, 2014

[4] M. J. Wright, T. White, N. Mangini, “Data Parallel Line Relaxation (DPLR) Code User Manual,” NASA Ames Research Center, 2009.

[5] K. T. Edquist, A. A. Dyakonov, M. J. Wright, C. Y. Tang, “Aerothermodynamic Design of the Mars Science Laboratory Heatshield,” AIAA Journal, vol. 51, no. 4, 2014.

[6] M. Mahzari and T. White, “Mars Science Laboratory Heatshield Flight Data and Analysis,”,NASA Ames Research Center Hypersonic Vehicle Flight Prediction Workshop, 2017

[7] P.R. Spalart and S. R. Allmaras, “A One-Equation Turbulence Model for Aerodynamic Flows,” AIAA Paper 92-0439, 1992.

[8] F. R. Menter, “Two-Equation Eddy-Viscosity Turbulence Models for Engineering Applications,” AIAA Journal, Vol. 32, No. 8, pp 1598-1605, 1994.

[9] X. Han, T. J. Wray, and R. K. Agarwal, "Application of a New DES Model Based on Wray-Agarwal Turbulence Model for Simulation of Wall-Bounded Flows with Separation," AIAA Paper 2017-3966, June 2017.

[10] G. S. Settles, T. J. Fitzpatrick, and S. M. Bogdonoff, “Detailed Study of Attached and Separated Compression Corner Flowfields in High Reynolds Number Supersonic Flow,”AIAA Journal, vol. 17, no. 6, 1979.

[11] M. Holden, M. MacLean, T. Wadhams, and E. Mundy, “Experimental Studies of Shock Wave/Turbulent Boundary Layer Interaction in High Reynolds Number Supersonic and Hypersonic Flows to Evaluate the Performance of CFD Codes,” AIAA Paper 2010-4468, 40th Fluid Dynamics Conference and Exhibit, Chicago, Illinois, June 28- July 1, 2010.

[12] A. J. Smits and K. C. Muck, “Experimental Study of Three-Dimensional Shock Wave/Turbulent Boundary Layer Interactions,” J. of Fluid Mechanics, Vol. 182, September 1987.